



**AFRL-RQ-WP-TR-2015-0041**

**CENTER FOR ADVANCED POWER AND ENERGY  
RESEARCH (CAPEC)**

**P.G. Huang**

**Wright State University**

**JANUARY 2015  
Final Report**

**Approved for public release; distribution unlimited.**

*See additional restrictions described on inside pages*

**STINFO COPY**

**AIR FORCE RESEARCH LABORATORY  
AEROSPACE SYSTEMS DIRECTORATE  
WRIGHT-PATTERSON AIR FORCE BASE, OH 45433-7541  
AIR FORCE MATERIEL COMMAND  
UNITED STATES AIR FORCE**

## NOTICE AND SIGNATURE PAGE

Using Government drawings, specifications, or other data included in this document for any purpose other than Government procurement does not in any way obligate the U.S. Government. The fact that the Government formulated or supplied the drawings, specifications, or other data does not license the holder or any other person or corporation; or convey any rights or permission to manufacture, use, or sell any patented invention that may relate to them.

This report was cleared for public release by the USAF 88th Air Base Wing (88 ABW) Public Affairs Office (PAO) and is available to the general public, including foreign nationals.

Copies may be obtained from the Defense Technical Information Center (DTIC)  
(<http://www.dtic.mil>).

AFRL-RQ-WP-TR-2015-0041 HAS BEEN REVIEWED AND IS APPROVED FOR  
PUBLICATION IN ACCORDANCE WITH ASSIGNED DISTRIBUTION STATEMENT.

\*//Signature//

MICHAEL A. ROTTMAYER  
Project Manager  
Electrical Systems Branch  
Power and Control Division

//Signature//

GREGORY L. FRONISTA, Chief  
Electrical Systems Branch  
Power and Control Division  
Aerospace Systems Directorate

//Signature//

JOHN G. NAIRUS, Chief Engineer  
Power and Control Division  
Aerospace Systems Directorate

This report is published in the interest of scientific and technical information exchange, and its publication does not constitute the Government's approval or disapproval of its ideas or findings.

\*Disseminated copies will show “//Signature//” stamped or typed above the signature blocks.

REPORT DOCUMENTATION PAGE				Form Approved OMB No. 0704-0188	
<p>The public reporting burden for this collection of information is estimated to average 1 hour per response, including the time for reviewing instructions, searching existing data sources, gathering and maintaining the data needed, and completing and reviewing the collection of information. Send comments regarding this burden estimate or any other aspect of this collection of information, including suggestions for reducing this burden, to Department of Defense, Washington Headquarters Services, Directorate for Information Operations and Reports (0704-0188), 1215 Jefferson Davis Highway, Suite 1204, Arlington, VA 22202-4302. Respondents should be aware that notwithstanding any other provision of law, no person shall be subject to any penalty for failing to comply with a collection of information if it does not display a currently valid OMB control number. <b>PLEASE DO NOT RETURN YOUR FORM TO THE ABOVE ADDRESS.</b></p>					
1. REPORT DATE (DD-MM-YY) January 2015		2. REPORT TYPE Final		3. DATES COVERED (From - To) 12 September 2007 – 01 January 2015	
4. TITLE AND SUBTITLE CENTER FOR ADVANCED POWER AND ENERGY RESEARCH (CAPEC)				5a. CONTRACT NUMBER FA8650-07-2-2808	
				5b. GRANT NUMBER	
				5c. PROGRAM ELEMENT NUMBER 62203F	
6. AUTHOR(S) P.G. Huang				5d. PROJECT NUMBER 3145	
				5e. TASK NUMBER	
				5f. WORK UNIT NUMBER Q0M1	
7. PERFORMING ORGANIZATION NAME(S) AND ADDRESS(ES) Wright State University Center for Micro Air Vehicles Studies 3640 Colonel Glenn Highway Dayton, OH 45435				8. PERFORMING ORGANIZATION REPORT NUMBER	
9. SPONSORING/MONITORING AGENCY NAME(S) AND ADDRESS(ES) Air Force Research Laboratory Aerospace Systems Directorate Wright-Patterson Air Force Base, OH 45433-7541 Air Force Materiel Command United States Air Force				10. SPONSORING/MONITORING AGENCY ACRONYM(S) AFRL/RQQE	
				11. SPONSORING/MONITORING AGENCY REPORT NUMBER(S) AFRL-RQ-WP-TR-2015-0041	
12. DISTRIBUTION/AVAILABILITY STATEMENT Approved for public release; distribution unlimited.					
13. SUPPLEMENTARY NOTES PA Case Number: 88ABW-2015-2592; Clearance Date: 22 May 2015.					
14. ABSTRACT <p>This report summarizes the activities conducted at the Center for Advanced Power and Energy Research (CAPEC) from 2010 to 2014. The Center was formed to serve the needs of the Air Force Research Laboratory (AFRL) in research of development of power and energy. CAPEC was a collaborative activity between AFRL and Wright State University structured through a cooperative research agreement. Our organizational focuses include:</p> <ol style="list-style-type: none"> <li>1. Modeling of plasma physics</li> <li>2. Modeling fuel cells</li> <li>3. Testing new innovation and ideas for advanced fuel cells</li> <li>4. Development of energy related issue for micro air vehicles (MAVs).</li> </ol>					
15. SUBJECT TERMS plasma physics, fuel cells, micro air vehicles, power, propulsion					
16. SECURITY CLASSIFICATION OF:			17. LIMITATION OF ABSTRACT: SAR	18. NUMBER OF PAGES 114	19a. NAME OF RESPONSIBLE PERSON (Monitor) Michael A. Rottmayer 19b. TELEPHONE NUMBER (Include Area Code) N/A
a. REPORT Unclassified	b. ABSTRACT Unclassified	c. THIS PAGE Unclassified			

## Table of Contents

Section	Page
List of Figures .....	iii
List of Tables .....	v
1 Summary .....	1
2 Plasma Modeling.....	2
2.1 Introduction .....	2
2.2 Aerodynamics-Electromagnetics Interaction Equations .....	4
2.3 Physics-Base Discharge Modeling.....	7
2.4 Ionization Modeling .....	10
2.5 Electromagnetic Equations.....	13
2.6 Numerical Procedure.....	14
2.7 Boundary Conditions of Direct Current Discharge.....	19
2.8 Characteristics of DCD .....	20
2.9 Boundary Conditions of Dielectric Barrier Discharge.....	28
2.10 Characteristics of DBD.....	31
2.11 Periodic Electrostatic Force of DBD .....	37
2.12 Concluding Remarks .....	43
3 Modeling Fuel Cells .....	45
3.1 Introduction .....	45
3.2 Numerical Model.....	45
3.2.1 Anode.....	45
3.2.2 Overpotential due to Mass transport .....	47
3.2.3 Anode governing equations and boundary conditions.....	49
3.3 Cathode.....	51
3.3.1 Overpotential due to electrochemical reactions and ohmic resistance .....	51
3.3.2 Overpotential due to mass transport .....	51
3.3.3 Cathode governing equations and boundary conditions .....	52
3.4 Analysis of Microstructure Parameters Correlations and Percolation Threshold .....	53
3.4.1 Relationship between porosity and tortuosity.....	53
3.4.2 Relationship between porosity and particle size .....	54
3.5 Percolation Threshold .....	55
3.5.1 Model Validation .....	55
3.6 Model Sensitivity Study .....	61
3.6.1 Tortuosity vs. Porosity .....	62
3.6.2 Particle size ratio vs. porosity .....	64
3.6.3 Discussion .....	65
3.6.4 Conclusion .....	66
4 Fabrication and Testing of Advanced Solid Oxide Fuel Cells.....	67
4.1 Impact of In-line Mixer for Printing Anode Interlayer: .....	67
4.2 Graded Braze Power Electronics.....	68
5 Measurement of Static and Dynamic Performance Characteristics of Small Electric Propulsion Systems.....	71
5.1 Introduction .....	71
5.2 Background .....	74
5.3 Experimental setup.....	75

5.4	Uncertainty analysis .....	78
5.5	Experimental procedures.....	81
5.5.1	Static test procedure.....	81
5.5.2	Dynamic test procedure .....	82
5.6	Results and discussion.....	82
5.6.1	Validation of the static test .....	82
5.6.2	Static test results .....	85
5.6.3	Validation of the dynamic test .....	89
5.6.4	Dynamic test results .....	94
5.7	Conclusions .....	101
6	References .....	<b>103</b>

## List of Figures

Figure	Page
Figure 1 Iterative Convergent Acceleration for Solving Poisson Equation of Plasmadynamics	18
Figure 2 Grid Independent Studies .....	19
Figure 3 Electron and Positively Charged Ion Number Density Contours of Parallel Electrodes .....	21
Figure 4 Surface Normal Electric Field Intensity .....	22
Figure 5 Electron Temperature Profile with a DCD Discharge .....	23
Figure 6 Electron and Ion Number Density .....	24
Figure 7 Measurement of Electron Number Density .....	25
Figure 8 Normal Electric Field Intensity .....	26
Figure 9 Joule Heating Contour .....	27
Figure 10 DCD in Transverse Magnetic Field, $B_z=0$ , $B_z=-0.1$ , and $B_z=+0.1$ .....	27
Figure 11 Electrical Current Vectors in the Presence of an Externally Applied Magnetic Field	28
Figure 12 Voltage-current Curve and Discharge Photos Exposed Electrode Anode (U) and Cathode (L) .....	31
Figure 13 Compare Voltage-current Curves (5kHz) with Experimental Observation .....	32
Figure 14 Effect of Discharge duration with Different EMF .....	33
Figure 15 Discharge Domains of DBD by Different Applied EMFs .....	34
Figure 16 Effect of Gap Distances to DBD Discharge .....	35
Figure 17 Effect of Permittivity on DBD Domain .....	36
Figure 18 Comparison of Electrical Conductivity Current with Experimental Measurement, $\phi=4$ kV, $w=10$ kHz .....	36
Figure 19. Comparison of Dimensionless Electric Potential .....	38
Figure 20. Comparison of (a) Positive Ion Density, (b) Electron Density, and (c) Force Field	39
Figure 21. Electric Current Voltage Patterns of the Two-charged-species ( $n_e$ , $n_+$ ) and Three-charged-species ( $n_e$ , $n_-$ , $n_+$ ) Ionization Model, EMF=8.0 kV, $f=5.0$ kHz .....	40
Figure 22. Comparison of Two- and Three-species Ionization Models of DBD at the Peak Positive Cycle .....	41
Figure 23 Comparison of Two- and Three-species Ionization Models of DBD at the Peak Negative Cycle .....	42
Figure 24 Time-averaged Electromagnetic Force of DBD over a Completely AC Cycle, EMF=8.0 kV, $f=5.0$ kHz .....	43
Figure 25 Anode Computational Domain .....	50
Figure 26 Dependence of Tortuosity on the Packing Porosity .....	53
Figure 27 Dependence of $n$ on $\phi L$ for Different Particle Size Ratios .....	54
Figure 28 Packing Density vs. Composition for Different Particle Size Ratios .....	55
Figure 29 Comparison between Numerical Results and Experimental Data for Case No. 1 .	58
Figure 30 Comparison between numerical results and experimental data for case No. 2 .....	58
Figure 31 SEM of Ni/ 8 mol% $Y_2O_3$ - $ZrO_2$ (Ni/TZ8Y) Cermet Anodes Sintered at (a) 1300°C, (b) 1350°C, (c) 1400°C, (d) 1500°C .....	60
Figure 32 Comparison between Numerical Results and Experimental Data for Case No. 3 .	61
Figure 33 Comparison of Predicted Anode Overpotential at Different $n$ -values .....	64
Figure 34 Effect of particle size ratio on active surface area .....	64

Figure 35 Comparison of Predicted Anode Overpotential at Different Particle Size Ratio Values .....	65
Figure 36 Cell (a) –no anode interlayer, (c) and (d)-cells with anode interlayer.....	68
Figure 37 Cross Section of a Typical Cell with Anode Interlayer.....	69
Figure 38 Scanning Electron Image of Cells (a), (c), and (d).....	69
Figure 39 As Sintered @320C Ag Tape Die Attach Layer .....	70
Figure 40 Schematic Diagram of the Experimental Setup.....	75
Figure 41 Assembly of Motor, Torque Cell and Load Cell: (a) Solid Model Representation; (b) Photograph .....	76
Figure 42 Typical Static Test Results .....	83
Figure 43 Comparison of Three Identical Propellers under Static Testing .....	84
Figure 44 Comparison of the Present Static Results to Deters and Selig (2008) .....	85
Figure 45 The Effect of Varying Pitch While Holding Diameter Constant (Static Testing)..	87
Figure 46 The Effect of Varying Diameter While Holding Pitch Constant (Static Testing)..	88
Figure 47 Typical Dynamic Test Results (Graupner $4.7 \times 4.7$ inch Propeller) .....	90
Figure 48 Comparison of Present Dynamic Results to Selig (2012) (APC $8.0 \times 3.8$ SF).....	91
Figure 49 Comparison of Present Dynamic Results to Ol et al. (2008) (APC $6.0 \times 4.0$ ).....	93
Figure 50 The Effect of Varying Propeller Pitch while holding Diameter Constant (Dynamic Testing) .....	95
Figure 51 The Effect of Varying Propeller Diameter while holding Pitch Constant (Dynamic Testing) .....	96
Figure 52 Coefficient of Thrust versus Advance Ratio for Square Propellers ( $D/P = 1.0$ ) with Propeller Diameter Ranging from $4.0 \leq D \leq 18$ inches. ....	97
Figure 53 Coefficient of Thrust vs. Advance Ratio for the APC Sport 400 Electric Propellers ( $\Delta C_T \leq 20\%$ ) .....	98
Figure 54 Coefficient of Propeller Power versus Advance Ratio for the APC Sport 400 Electric Propellers ( $\Delta C_P \leq 20\%$ ) .....	100
Figure 55 Propeller Efficiency vs. Advance Ratio for the APC Sport 400 Electric Propellers ( $\Delta \eta_P \leq 20\%$ ).....	101

## List of Tables

Table	Page
Table 1 $\epsilon_i$ and $\xi_i/k_B$ values .....	56
Table 2 Value of input parameters for model validation case No. 1 .....	56
Table 3 Upper and lower bounds for particle size ratio and electronic volume fraction for 79% Ni/ 21% YSZ .....	57
Table 4 Value of input parameters for model validation case No. 2 .....	62
Table 5 Value of input parameters for model validation case No. 3 .....	63
Table 6 Results of sensitivity study .....	66
Table 7 Summary of Propellers Studied. ....	78
Table 8 Uncertainties of Primary Measurement Sensors and Calibration Sources. ....	81



# **1 SUMMARY**

This report summarizes the activities conducted at the Center for Advanced Power and Energy Research (CAPEC) from 2010 to 2014. The Center was formed to serve the needs of the Air Force Research Laboratory (AFRL) in research of development of power and energy. CAPEC was a collaborative activity between AFRL and Wright State University structured through a cooperative research agreement. The organizational focuses include:

1. Modeling of plasma physics
2. Modeling fuel cells
3. Testing new innovation and ideas for advanced fuel cells
4. Development of energy related issue for micro air vehicles (MAVs).

In Section 2, the final summary of present work on plasma modeling is discussed. The fuel cell modeling approach is given in Section 3. The development in fabrication and testing of advanced solid oxide fuel cells is provided in Section 4. The characterization of MAV propulsion system will be given in Section 5.

## 2 Plasma Modeling

### 2.1 Introduction

Sustained research interest and achievements in flow control by aerodynamics-electromagnetics interactions have grown in the past few years. Numerous innovative techniques have been developed in a wide range of applications from the remote energy deposition, electrical-thermal energy conversion, to surface plasma generation for flow control. However, the surface plasma actuators are the most frequently adopted technique for its simplicity, nonintrusive implementation and control effectiveness [1-5]. The interaction of aerodynamics-electromagnetics is derived from the three basic electromagnetic properties [6,7]: The electrostatic force by the free-space charge separation in the plasma sheath which is the cornerstone of dielectric barrier discharge (DBD) operation. A series of applications devised by Corke et al. [1-2], as well as, Moreau and his colleagues [3] have been successfully demonstrated for flow control at subsonic and transonic flow regimes. The Joule heating occurs for all electrical discharge but it's the dominant effect for direct current discharge (DCD). A glow discharge at a low ambient density becomes Corona discharge at the elevated ambient pressure condition. The thermal plasma actuator is best suited for high altitude flight and closely associated with hypersonic flows [4,5]. The third mechanism for plasma actuator is the Lorentz acceleration which is a cross product of an externally applied magnetic field and the discharge current.

In surface plasma generation by the electron collision process, the Townsend's mechanism controls the secondary emission, multiple primary avalanches, and ultimately maintains the discharge [7,8]. For this reason, the classic Townsend's similarity law for electron impact ionization is still a viable formulation of the complex chemical-physical process to simulate the electrical field dominated phenomena. The charged particle number density is generally limited to an order of magnitude of  $10^{12}$  per cubic centimeter. The generated plasma consists of electrons in a highly excited state but the heavy ions retain the thermodynamic condition of their surrounding environment. Therefore, the weakly ionized gas is usually far from thermodynamic equilibrium. Meanwhile the drift motion of charged particles and diffusion, including the ambipolar diffusion, profoundly modifies the transport properties of the ionized medium.

In contrast to DCD, the DBD is maintained by an alternating electric current. The DBD operates on a self-limiting process through the reduced electric field potential by the surface charge accumulation, thus prevents the corona-to-spark transition [7,8]. Specifically, the earlier outstanding effort by Elisson and Kogelschatz [9] has identified that the discharge consists of two distinct positive Corona streamers and diffusion modes. Enloe et al. [10,11] have reaffirmed that when the exposed electrode is positively biased in the AC cycle, the discharge is characterized by a streamer like structure. These microdischarges have a short life span of about a few nanoseconds and with the random temporal and spatial structures. In the negatively biased phase of the exposed electrode, it acts as the cathode and the discharge appears as a more diffusive structure [9-11]. The discharge pattern over the dielectric surface depends on the polarity and intensity of the applied electric field, as well as, the electric permittivity of the dielectrics [7]. In essence, the propagation of charged particles is in a locked-step to the frequency of the AC field. Meanwhile the induced electrostatic force by the free-space charge separation during the AC cycles becomes a periodic dynamic event. Nevertheless, the discharge phases still can be identified as avalanche, streamer formation, a subsequent glow discharge and finally quenching of the microdischarge on the electrodes [7,8]. A complex physical

phenomenon of DBD emerges; a wide range of discharge patterns are observed depending on the gas mixture composition, pressure, electrodes arrangement, and other parameters. However, the global structure always consists of the continuous diffusive and random distributed pulsing microdischarges in a short duration.

An enormous amount of energy is needed to generate localized volumetric plasma that must have a sufficient charged particle number density for strong magneto-aerodynamic interactions [1-5]. For examples, the ionization potential is 34 eV for electron beam [12], 65.7 eV for DCD, and 81 eV per ion-electron pair for discharge at the radio frequency [7,8]. The ionization potential always underestimates the energy requirement in applications, because the nonequilibrium energy cascades to vibration excitation, recombination, and attachment processes. In the electron impact processes for ionization, the positive and negative charged ions still retain their ambient condition. For this reason, the partially ionized is often identified as the low-temperature plasma with a charge number density generally limited to the order of magnitude of  $10^{12}/\text{cm}^3$ . As a weakly partial ionized plasma, the electromagnetic force usually exerts a small perturbation to the mainstream flow and the thermodynamic behavior is significantly different from the plasma generated by thermal excitation [7,11]. Therefore the plasma actuator for flow control is the most effective at the flow bifurcations such as the onset of dynamic stall, laminar-turbulent transition, vortical separation [1,2]. However the electromagnetic effect can also be amplified by an externally applied magnetic field or by inviscid-viscous interaction at the leading edge of hypersonic control surfaces [4,5].

The nonequilibrium chemical kinetics associated with the DBD in atmosphere is well known because it had been applied as an ozone generator for years. Elisson et al. [9] have identified plasma chemistry in microdischarge by 30 species through 143 elementary reactions. In a more recent work by Bogdanov et al. [13], the chemical-physics kinetics of atmospheric plasma have been investigated by 576 chemical reactions involving vibrational excitations of nitrogen and oxygen, ozone, positive and negative ions, besides oxide-nitrides. The complexity of the internal degrees of excitations includes molecular nitrogen and oxygen at few quanta above ground states; the atomic nitrogen, ( $4S, 2D, 2P$ ), oxygen ( $^3P, ^1S, ^1D$ ), the charged nitrogen molecules ( $A^3\Sigma_u^+, B^3\Pi_g, A^1\Pi_g, C^3\Pi_u$ ) and oxygen ( $X^3\Sigma_u^+, A^1\Delta, B^1\Pi$ ), ozone molecules  $O_3$ , as well as, negatively charged ions ( $N_2O^-, NO^-, O^-, O_2^-, O_3^-, \dots$ ) and positively charged ions ( $N^+, O^+, NO^+, NO_2^+, \dots$ ) respectively. Bogdanov et al. also have correctly pointed out that the concentrations of the negatively charged ions is relatively lower than the positively charged counterpart, but the effect of the negatively charged ions can still exert a critical directional demarcation for the electrostatic force during an AC cycle. The finding by Kim et al [14] has also shown the  $O_2^-$  plays a dominant role in DBD plasma actuator. Again, DBD is a nonequilibrium transient discharge. The mean energy state of the electrons and heavy particles is considerably different. For this reason the energy of charged particles can be effectively transferred to the internal states of molecule or atom.

In DBD applications, the interaction of charged particles and the dielectrics is important. According to Golubovskii et al. [15], the photoemission is negligibly small for nitrogen because the energy of photons in the visible range is too small to cause the emission of electrons. Raizer [7] also has pointed out that the photoemission cannot compete with electron impact ionization because the collision cross sections of molecular and atomic oxygen and nitrogen close to the emission threshold are rather high ( $10^{-16} \text{ cm}^2$ ). In gist, the gas in DBD occupies only few quanta

above the ground state that is capable of photoemission. The process however can supply the seeding electrons that need to start the avalanche in streamer propagation [7,16].

The other important processes are desorption of electrons and surface recombination. The electrons can be desorbed mostly by energy cascading to vibrational excitation or by depletion of the metastable molecule  $N_2(A^3\Sigma_u^+)$ . However, the secondary electrons emission of electrons from the surface during an AC cycle is the dominant mechanism and leads to the charge separation in the cathode layer. Meanwhile, the surface charge accumulation also alters the electric potential within the discharge domain. In view of the relatively short duration of microdischarge versus the microsecond time scale of the AC cycle; the instantaneous surface recombination is a plausible and acceptable approximation. In this connection, one needs to be mindful of the fact that the positive charge builds up on the dielectrics far downstream of the DBD has also been observed by Opaits et al. [17]. They also noted that the surface potential coincided with the biased polarity and depletes slowly in duration of tens of minutes to degrade the performance of DBD. Finally and most importantly, the ionization of DBD is still a basic Townsend process [7,8]. This observation becomes the foundation to all known formulation for ionization by electron collisions.

The periodic electrostatic force in the charge separation region is proportional to the product of the net balance of electrically charged number density and electric field intensity within the plasma. The former is the difference between the number densities of positively and negatively charged ions with electrons,  $\rho_e = e(n_i^+ - n_e - n_i^-)$ . The compatible electric field intensity is also modified by the distributions of the charged particle density or the charged species concentration [7]. On the other hand, the distinct differences in time scales in the fast ionization ( $10^{-11}$ s), the slower diffusion phenomena ( $10^{-4}$ s) and the AC cycle ( $10^{-3}$ s) are the key elements for DBD operation [13-18]. It is recognized that the range of time scales varies greatly through the values from tens of nanoseconds to a few millisecond [16]. The required temporal resolution for experimental measurements and computational simulations impose a significant challenge [3,11,15-16]. In computational simulation, the spatial resolution requirement for multiple microdischarges is also beyond the current computational capability. Therefore an alternative approach to evaluate the low-temperature weakly ionized gas becomes necessary.

The objectives of the present investigation are hopefully to clarify some of the conflicting explanations by putting the models of DCD and BDB for plasma actuation on a theoretical frame based on the drift-diffusion and chemical-physics approximations. Although there are deficiencies in ionization by electron impact process, transport property by the drift-diffusion formulation, and bypassing the detailed multiple microdischarges simulation, but the fundamental physics is rigorously described by the electromagnetic theory. It is further hoped that the present formulation can be used as a stepping stone for future progress.

## 2.2 Aerodynamics-Electromagnetics Interaction Equations

The rigorous and complex governing equations for flow control using plasma actuation consist of the compressible Navier-Stokes equation, Maxwell equation for electromagnetics, law of mass action including quantum chemical-physics for nonequilibrium chemical reaction, and the gas kinetics for transport properties. However, from all existed experimental evidences and an order-of-the magnitude analyses [1-6,18-21], the electromagnetic force and energy appear mostly as a perturbation to the inertia of the main flowfield. In most plasma based flow control environments,

the Magnetic Reynolds number which is the product of the electrical conductivity  $\sigma$ , magnetic permeability  $\mu_m$ , characteristic velocity and length scales of the study phenomenon

$R_m = ul / (\sigma\mu_m)^{-1}$ , usually has a value much less than unity. Under this condition, the induced magnetic flux density,  $\frac{\partial B}{\partial t}$  is negligible in comparison with the externally applied field [4-6,19].

As the consequence, the Faraday's induction law can be decoupled from the rest of the Maxwell's equations. This simplification focuses the study of magneto-aerodynamic interaction with fluid dynamics rather than electromagnetic wave motion. In this formulation the electrostatic force, Lorentz acceleration, and Joule heating are appears as the perturbing source terms in the generalized Navier-Stokes equations. Therefore, the essential physics of aerodynamics-electromagnetics interaction for plasma flow control can be effectively approximated by a simplified governing equation system which can be summarized as:

$$\frac{\partial \rho_i}{\partial t} + \nabla \cdot [\rho_i(\vec{u} + \vec{u}_i)] = \frac{dw_i}{dt}, \quad (2-1)$$

$$\frac{\partial \rho \vec{u}}{\partial t} + \nabla \cdot (\rho \vec{u} \vec{u} + p \vec{I} - \vec{\tau}) = \rho_e \vec{E} + (\vec{J} \times \vec{B}), \quad (2-2)$$

$$\frac{\partial \rho e}{\partial t} + \nabla \cdot [\rho e \vec{u} - \kappa \nabla T + \sum \rho_i u_i h_i + q_{rad} + \vec{u} \cdot p \vec{I} + \vec{u} \cdot \vec{\tau}] + Q_{vt} - Q_{et} = \vec{E} \cdot \vec{J}. \quad (2-3)$$

The vibrational energy conservation equations for polyatomic molecular species are;

$$\frac{\partial \rho_i e_{iv}}{\partial t} + \nabla \cdot [\rho_i(\vec{u} + \vec{u}_i) e_{iv} + q_{iv}] = e_{iv} \frac{dw_i}{dt} + Q_{v,\Sigma}. \quad (2-4)$$

The electronic energy conservation equation has been traditionally given as;

$$\begin{aligned} \frac{\partial \rho_i e_e}{\partial t} + \nabla \cdot [\rho_i(\vec{u} + \vec{u}_i) e_e + \vec{u} \cdot p_e \vec{I} + q_e] &= e_e \frac{dw_i}{dt} + \vec{E} \cdot \vec{J} \\ &+ [\rho_e \vec{E} + (\vec{J} \times \vec{B})] \cdot (\vec{u} + \vec{u}_i) + Q_{e,\Sigma}. \end{aligned} \quad (2-5)$$

where  $\vec{J}$  is the current density,  $\vec{J} = e[-d_+ \nabla n_+ + d_- \nabla n_- + d_- \nabla n_- + (n_+ \mu_+ - n_e \mu_e - n_- \mu_-) \vec{E}]$  of the partially ionized gas, and can be approximated by the transport property consisting of the drift velocity and diffusion. The electron and ion mobilities ( $\mu_e, \mu_+, \mu_-$ ) are traditionally evaluated as the functions of the reduced electric field intensity  $E/P$ , and the diffusion coefficients ( $d_e, d_+, d_-$ ) of the charged molecules can be calculated by the Einstein formula [7,8]. The diffusion and drift velocity for both positively and negatively charged ions, as well as, electrons are included to describe the individual random and forced motions of the charged particles. The vector field of  $\vec{E}$  and  $\vec{B}$  are the sum of the externally applied and induced electrical and magnetic field intensities.

The net energy transfer between translational, vibration, electronic excitations, and the sums in each degree of freedom that appears in Equations (2-3), (2-4), and (2-5) are designated as  $Q_{v_i}$ ,  $Q_{e_i}$ ,  $Q_{v,\Sigma}$ , and  $Q_{e,\Sigma}$  respectively. The energy cascading processes for the partially ionized gas occur beneath the atomic and molecule scales which cannot be described the gas kinetic theory, thus must be modeled through the quantum chemical and chemical-physical kinetics [18-20].

It is important to note that in the governing Equations (2-2), (2-3), and (2-5), the coupling between fluid motion and electromagnetic force/energy appears as the electrostatic force  $\rho_e \vec{E}$ , Lorentz acceleration  $\vec{J} \times \vec{B}$ , and Joule heating  $\vec{E} \cdot \vec{J}$  [6,7]. In the absence of an externally applied magnetic field, the charged particles are accelerated by the electrostatic force due to charge separation in the plasma sheath. The well-known induced gas motion by DBD is the consequence of momentum transfer by collisions between charged ions and the neutral molecules [1-3]. On the other hand, the DCD imparts thermal energy to the external stream through Joule heating mostly in the cathode layer in addition to the electrode heating. It is the basic mechanism of plasma actuator by thermal effect [3-5].

The vivid illustration by applying Lorentz acceleration to alter the flowfield structure is displayed in the classic experimental by Ziemer [22]. He has convincingly demonstrated that an externally applied magnetic field can change the bow shock standoff distance by the magnetic pressure,  $\vec{B} \cdot \vec{B} / 2\mu$  [19]. The electromagnetic-aerodynamic interaction with an externally applied magnetic field in partially ionized gas has been applied to hypersonic control surface and inlet [4,5], a sharp-nose conical configuration by Cristofolini et al. [23], and heat-flux mitigation at the stagnation region of blunt bodies by Matsuda et al. [24] and Gulhan et al. [25]. The dependence of the interdisciplinary formulations on the Maxwell equations will be deferred to the section of the discharge modeling.

The law of mass action establishes the foundation for modeling chemical reaction, and the rate of species production and depletion in the species conservation law, Equation (2-1) is described by the Arrhenius formula through the forward and backward chemical reactions. For a total number of the chemical species of  $n$ , then a  $(n-1)$  number of concentration equations are required to be solved simultaneously. It is obvious; the required effort is tremendous and tedious.

$$\frac{dw_i}{dt} = M_i \sum_{j=1}^J (\nu''_{i,j} - \nu'_{i,j}) \left\{ k_{f,j} \prod_{k=1}^{N_{kf}} \left( \frac{\rho_k}{M_k} \right)^{\nu'_{k,j}} - k_{b,j} \prod_{k=1}^{N_{kb}} \left( \frac{\rho_k}{M_k} \right)^{\nu''_{k,j}} \right\} \quad (2-6)$$

For most investigations, the forward and backward chemical reaction rates are adopted from a wide range of chemical kinetic models and experimental data [13,15,19-21].

The definition of the internal energy is now given as;

$$\rho e = \sum_{i \neq e} \rho_i (c_{v,i} T + \frac{\vec{u} \cdot \vec{u}}{2}) + \sum_{i \neq e} \rho_e e_{v,i} + \sum_{i \neq e} \rho_i h_i^o + \rho_e (c_{v,e} T_e + \frac{\vec{u}_e \cdot \vec{u}_e}{2}) \quad (2-7)$$

where  $h_i^o$  is the standard heat of formation for all reacting species.

To be consistent with the kinetic model of internal structure of gas; transport properties of the gas mixture for thermal diffusion, molecular viscosity, and thermo conductivity need to be calculated from Boltzmann equation by Chapman-Enskog expansion [26]. It is a landmark

achievement of the kinetic theory of diluted gas mixture by its ability in describing the transport property of any combination of gaseous mixture by the inter-molecular potential functions. The required collision integrals and cross sections have been obtained by either the Lenard-Jones potential for non-polar molecules or a polarizability model for ion-neutral non-resonant collisions [27]. The results from the kinetic theory for the molecular viscosity and thermal conductivity of individual species are used to generate a global property for a gas mixture.

The interdisciplinary computational fluid dynamics (CFD) equations, Equation (2-1) through (2-5), have been widely applied for nonequilibrium chemical reacting flows and are independent from the specific plasma modeling. Therefore, the numerical algorithms and the required initial values and pertaining boundary conditions will not be elaborated in here. The details can be easily found in open literature and references [4,5,13,15,18-21].

## 2.3 Physics-Base Discharge Modeling

The modeling of weakly partial ionized gas actually consists of two parts; the transport property and the ionization process for the partially ionized gas. The physics for DCD is well known through the luminary contributions by Townsend [7,8]; the ionization is evolving from electrons impact, secondary emission, and avalanche. The physical process of the glow discharge has long been referred to as the Townsend mechanism. For the charged carried gas mixture, the transport properties must include the force diffusion by the applied electrical field on an electrically conducting medium and the ordinary and bipolar diffusions. For the gas discharge physics, the modeling and formulation based the drift-diffusion approximation for the transport property was established in the late 1980s [28,29]. The model for DCD flow control is first applied by Surzhikov and Shang and extends the discharge model to include an externally applied transverse magnetic field [30-32]. A series results of computational simulations using this model have been verified and validated by experimental observations conducted in a Mach five plasma channel [4,5,33].

For supersonic and hypersonic flow controls using DCD, both electrodes are exposed and flushed mounted over the surface so the combined electrode and joule heating will raise the temperature of the gas over the electrodes locally. In turn, the elevated local temperature increases the displacement thickness of the shear layer to induce compressible waves and eventually coalesces into an oblique shock [4,5,30,31,34]. In most DBD applications, two electrodes are either overlapped or placed at a very short distance of a few mm apart, and with a minuscule recessed height [1-3,10,11]. One of the electrodes is exposed and the other is encapsulated by a dielectric coating. The most significant effect of an encapsulated DBD electrode to the electromagnetic field is by modifying the electric field intensity through surface charge accumulation. Under a discharging condition, the dielectric electrode becomes a capacitor to diminish the electric field intensity across the electrodes. The quenching and replenishing rate of the surface discharge is dependent on the applied alternating voltage across the electrodes and the surrounding electrically conducting medium. To a degree, the rate is also dependent on the material property of the dielectric. The biased electric field intensity and the charge separation over the electrodes generate a periodic electrostatic force to move the charged particles which in turn transfer momentum by colliding with the neutral particles. In fact, the momentum transfer between the ions and the neutral particles lead the so-called electrical wind of the DBD. It is therefore logic to model the partially ionized air plasma by the multiple-fluid particle approximations.

In DBD operation, the Townsend's mechanism still controls the secondary emission initiated by electron collisions, multiple primary avalanches, and ultimately maintains the discharge. Impressive pioneering efforts by Massines et al. [35] and Lee et al. [36] have gained helpful insights. All the aforementioned approaches are assumed that in a high-pressure discharge field the electrons and ions are in equilibrium with the electric field. In particular, Lee et al solve the Boltzmann equation for the electron energy distribution function. All previous investigators understood the key elements of the discharge; the temporal-spatial variation of the physics must be analyzed simultaneously. Both efforts investigated the basic phenomenon during a single AC cycle after the initial transient has subsided.

The individual velocities of charged particle motions of weakly ionized plasma that constitutes of neutral molecules ( $10^{19} \text{ cm}^{-3}$ ), positively ( $10^{12} \text{ cm}^{-3}$ ) and negatively charged ions ( $10^9 \text{ cm}^{-3}$ ), as well as electrons have been derived by Surzhikov et al [31,32] from the momentum equation of charged particles motion. The electron-neutral collision frequency is proportional to the charged particle number density and the electron temperature. The time scale is orders of magnitude shorter than the organized motion of the neutral particles; thus the time dependency of the molecular shear stress and inertia of neutral particles in the momentum equation of charged particles motion are negligible. By defining the partial pressure of each charged species and omitting the relatively slower velocity of the organized motion of neutral particles, the individual charged species velocities can be summarized as the following;

$$\begin{aligned} n_e \vec{u}_e &= -d_e \nabla n_e - \mu_e n_e \vec{E} - \mu_e n_e (\vec{u}_e \times \vec{B}) \\ n_+ \vec{u}_+ &= -d_+ \nabla n_+ + \mu_+ n_+ \vec{E} - \mu_+ n_+ (\vec{u}_+ \times \vec{B}) \\ n_- \vec{u}_- &= -d_- \nabla n_- - \mu_- n_- \vec{E} - \mu_- n_- (\vec{u}_- \times \vec{B}) \end{aligned} \quad (2-8)$$

It is important to recognize, the above equations actually define the diffusion velocities of an inhomogeneous, electrically conducting mixture. The first terms in Equation (2-8) describe the ordinary diffusion due to local concentration of electrons, positively and negatively charged ions. The second terms are the force diffusion in form of drift motion for an electrically charged species by an externally applied electric field. The last terms are also the force diffusion by the Lorentz acceleration.

The species conservation equation becomes a simplified approximation to the continuity equation, Equation (2-1) for plasma flow control. The diffusion-drift model of weakly ionized air plasma is equally applicable to DCD and DBD. This formulation has been adopted by most recent numerical simulations by Surzhikov et al [30-32], Gibalov et al. [37], Boeuf et al. [38-39], Unfer et al. [40], Solv'ev et al. [41], Likhanskii et al. [42], Shang et al [43-45], and Huang et al. [46]. One of the weaknesses of this approximation is that the detailed distinction between metastable molecules is no longer recoverable by this approximation [9-11]. The weakly ionized gas is treated as a medium consists of three charged and one neutral species. The species conservation equations for the three distinct charged particles are:

$$\frac{\partial n_e}{\partial t} + \nabla \cdot \vec{\Gamma}_e = \frac{dw_e}{dt} \quad (2-9)$$



$$\frac{\partial n_+}{\partial t} + \nabla \cdot \vec{\Gamma}_+ = \frac{dw_+}{dt} \quad (2-10)$$

$$\frac{\partial n_-}{\partial t} + \nabla \cdot \vec{\Gamma}_- = \frac{dw_-}{dt} \quad (2-11)$$

Where the terms in the right-hand-side of the equations;  $\frac{dw_e}{dt}$ ,  $\frac{dw_+}{dt}$ , and  $\frac{dw_-}{dt}$  designate the production and depletion rates of the considered ionized species. These rates have either been determined by some chemical kinetic models [9,13,15,41,47] or simplified approximations based on the known ionization process [30-32,38-46]. The symbols  $\vec{\Gamma}_e$ ,  $\vec{\Gamma}_+$ , and  $\vec{\Gamma}_-$  denote the electron, positively and negatively charged ions flux densities and have the following definitions;

$$\begin{aligned} \vec{\Gamma}_e &= -d_e \nabla n_e - n_e \mu_e (\vec{E} + \vec{u}_e \times \vec{B}) \\ \vec{\Gamma}_+ &= -d_+ \nabla n_+ + n_+ \mu_+ (\vec{E} + \vec{u}_+ \times \vec{B}) \\ \vec{\Gamma}_- &= -d_- \nabla n_- - n_- \mu_- (\vec{E} + \vec{u}_- \times \vec{B}). \end{aligned} \quad (2-12)$$

The important connection between the coefficients of diffusion,  $d_i$  and the mobility,  $\mu_i$  of drift velocity is given by the Einstein relation [7,32], the relative magnitude is a function of the electron characteristic energy to the elementary electric charge.

$$\begin{aligned} \mu_e &= \frac{e}{m_e v_{en}} \approx \mu_e(|\vec{E}|/P); d_e = \frac{kT_e}{e} \mu_e \\ \mu_{\pm} &= \frac{e}{m_{\pm} v_{\pm n}} \approx \mu_{\pm}(|\vec{E}|/P); d_{\pm} = \frac{kT_{\pm}}{e} \mu_{\pm} \end{aligned} \quad (2-13)$$

Like the energy spectrum, it is a function of the reduced electrical field  $|\vec{E}|/P$ . When a considerable free space charge is formed by charged separation, the polarized electric field restrains the motion of electrons from that of ions to appear as the ambipolar diffusion. This coefficient of diffusion has frequently approximated by a function of the ratio of the electron energy and ambient states [30-32].

A general formulation for the drift-diffusion model including an externally applied magnetic field is very complex because the gyration of charged particle associated with the magnetic field polarity [6]. For the purpose of an analytic formulation, it is convenient to resolve the velocity of charged particles into component parallel and perpendicular to the direction of an externally applied magnetic field. In practical application, the transversal magnetic field for flow control is known to be the most effective [6-8]. Therefore, a two-dimensional formulation in (x,y) plane for charged particle flux densities including all the electromagnetic effect is viable by restricting the magnetic flux density to the z coordinate  $\vec{B}_z$ . The resultant equations are similar to that in the absence of an externally applied magnetic field by introducing effective electric field strengths as,

$$E_{e,x} = \frac{b_e E_y - E_x}{1 + b_e^2}, E_{e,y} = -\frac{b_e E_x + E_y}{1 + b_e^2}, \text{ and the components of the electron flux density becomes;}$$

$$\Gamma_{e,x} = -\mu_e n_e E_{e,x} - \frac{1}{1+b_e^2} d_e \frac{\partial n_e}{\partial x} + \frac{b_e}{1+b_e^2} d_e \frac{\partial n_e}{\partial y} \quad (2-14a)$$

$$\Gamma_{e,y} = -\mu_e n_e E_{e,y} - \frac{1}{1+b_e^2} d_e \frac{\partial n_e}{\partial y} - \frac{b_e}{1+b_e^2} d_e \frac{\partial n_e}{\partial x} \quad (2-14b)$$

Similarly for the positively charged ions, by letting  $E_{+,x} = \frac{E_x + b_+ E_y}{1+b_+^2}$ ,  $E_{+,y} = \frac{E_y - b_+ E_x}{1+b_+^2}$ , we have

$$\Gamma_{+,x} = \mu_+ n_+ E_{+,x} - \frac{1}{1+b_+^2} d_+ \frac{\partial n_+}{\partial x} - \frac{b_+}{1+b_+^2} d_+ \frac{\partial n_+}{\partial y} \quad (2-15a)$$

$$\Gamma_{+,y} = \mu_+ n_+ E_{+,y} - \frac{1}{1+b_+^2} d_+ \frac{\partial n_+}{\partial y} + \frac{b_+}{1+b_+^2} d_+ \frac{\partial n_+}{\partial x} \quad (2-15b)$$

Finally, set the effective electric field strength as  $E_{-,x} = \frac{E_x - b_- E_y}{1+b_-^2}$ ,  $E_{-,y} = \frac{E_y + b_- E_x}{1+b_-^2}$ . The components of the negatively charged ions are;

$$\Gamma_{-,x} = -\mu_- n_- E_{-,x} - \frac{1}{1+b_-^2} d_- \frac{\partial n_-}{\partial x} + \frac{b_-}{1+b_-^2} d_- \frac{\partial n_-}{\partial y} \quad (2-16a)$$

$$\Gamma_{-,y} = -\mu_- n_- E_{-,y} - \frac{1}{1+b_-^2} d_- \frac{\partial n_-}{\partial y} - \frac{b_-}{1+b_-^2} d_- \frac{\partial n_-}{\partial x} \quad (2-16b)$$

In the above equations,  $b_e$ ,  $b_+$ , and  $b_-$  are the Hall parameters for electrons, positively and negatively charged ions, which are directly related to the Larmor frequencies of electrons and the ions,  $b_e = \frac{\mu_e B_z}{c} = \frac{\omega_e}{\nu_e}$ ,  $b_- = \frac{\mu_- B_z}{c} = \frac{\omega_-}{\nu_-}$ , and  $b_+ = \frac{\mu_+ B_z}{c} = \frac{\omega_+}{\nu_+}$ . In here,  $\nu_e$ ,  $\nu_-$ , and  $\nu_+$  are the averaged electron and ion collision frequencies [6,7].

The above formulations have been validated by successfully simulating hypersonic flow controls in the presence of an externally applied transverse magnetic field at a sharp leading edge and in a virtual variable area inlet cowl [4,5,30,33]. The numerical results are verified by experimental data generated by a Mach five plasma channel. On the sharp-leading edge, the experimental data and numerical results of the surface pressure reveal a substantially amplified viscous-inviscid phenomenon by the transverse magnetic field through the magneto-aerodynamics interaction. Similarly, the computational simulations also compare well with the Pitot pressure surveys in the cross-section planes and surface pressure distributions within a square cross-section inlet [4,5].

## 2.4 Ionization Modeling

The ionization process by electron impact is distinct from the thermal excitation, but the nonequilibrium ionized species concentrations must satisfy the law of mass action. For this reason, the ionization processes are treated as chemical reactions of molecules, atoms, and electrons or ions. Chemical kinetics models for the low-temperature plasma generation span a

very wide range of complexity, from the detailed description by Elisson et al. [9], Bogdanoff et al [13] to simplified approximations by Solov'ev et al. [41] and Singn and Roy [47]. Singn et al. reduce the chemical kinetic model by omitting the metastable species and the nitrous oxide. Solov'ev et al. simplify their selection of the elementary chemical reactions based on the comparable reaction rates of species to the characteristic time scale on the order of 30 nanoseconds for DBD in atmospheric air. The approach is rational and the fidelity of numerical simulation to nonequilibrium chemical reaction is solely depended on the empirical determined rate constants. Unfortunately, it's the weakest link of ionization models for both the high-temperature thermal excitation and electron collision mechanisms [9,13,20,21,41]. The complete differential equations system of species conservation is very stiff to become a formidable computational challenge.

An alternative approach in determining the net rates of generation and depletion of individual ionized species can be achieved by the chemical-physics ionization modeling. In fact the ionization by electron collisions occurs at the outer limited of the Maxwell-Boltzmann distribution where the gas energy is lower than the ionization potential [7]. The dominated species of DBD are the metastable molecules  $N_2(A^3\Sigma_u^+)$  and  $O_2(b^1\Sigma_d^+)$ . The main ionized processes of a nonequilibrium volumetric discharge consist of four type of reactions; electron/molecular, atomic/molecular, decomposition and synthesis [7,9]. At any instance during discharge, the ionized species concentration is the net balance between ionization, detachment, attachment, and recombination processes. The ionization model is therefore focused on these mechanisms.

The classic formulation for electronic impact ionization is the similar law by Townsend and is an empirical formula. In the formulation, the ionization coefficient  $\alpha$  which measures the number of ionization by electron per unit distance is a function of the reduced electrical field  $|\vec{E}|/P$  [7,8].

This quotient is also a measure of the energy gain by a charged particle between collisions from the principle of similarity. In fact, the coefficient  $\alpha = A \exp(-Bp / |\vec{E}|)$  of Townsend's similarity law holds extremely well in comparison with a large group of experimental data both in the ionization frequency and degree of ionization. For discharge in air;  $A=15$  and  $B=365$  in the  $E/P$  range from 100 to 800 (V/Torr cm). At a relatively higher value of  $E/P$ , an accuracy improvement may be needed but is not essential. The coefficients of ionization for air can be summarized as;

$$\left(\frac{\alpha}{p}\right) = 15 \exp\left[-\frac{365}{(|\vec{E}|/P)}\right], 1/cm \cdot torr \quad (2-17)$$

The dissociative recombination is the fastest mechanism of the bulk recombination of the weakly ionized gas, and is a simple binary chemical reaction. The decay rate with time of plasma is often given as  $(\frac{dn_e}{dt})_i = -\beta n_+ n_e$ , and typically coefficient  $\beta$  is assigned a value of  $2 \times 10^{-7} \text{ cm}^3/\text{s}$  and the characteristic decay time scale is less than  $10^{-3}$  second.

Another main mechanism of charge neutralization is the ion-ion recombination process. At the low pressure environment, the recombination takes place through binary collision and the reaction is similar to charge transfer [9,13,15]. At the moderate pressure, the process proceeds

through triple collisions, again the rate of ion-ion recombination can be given as  $(\frac{dn_i}{dt})_r = -\beta_i n_+ n_-$ .

For an example, the recombination rate constants between  $O_2^-$  and  $O_4^+$ , as well as,  $NO^+$  and  $NO_2^-$  are on the order of magnitude of  $10^{-25}$  and  $10^{-26}$   $\text{cm}^6/\text{s}$  [7,13]. The maximum value of the ion-ion recombination at the one atmosphere has a value of  $10^{-6}$   $\text{cm}^3/\text{s}$  [7].

The electron attachment and detachment are the formation and depletion of the negative charged ions in the partially ionized air [9]. For the strongly bound molecules, a sufficiently high energy is required for the dissociative attachment of an electron. The electron attachment is the main mechanism for removing the electron from the negatively charge ions. The lost electron number density can be given as;  $(\frac{dn_e}{dt})_a = -\nu_a n_e$ . The attachment frequency of electron in dry air at one atmosphere condition is around  $10^8/\text{s}$  [7].

The coefficients of the detachment of electron,  $\kappa_d$  in partially ionized gas at the room temperature have the value of  $10^{-10}$   $\text{cm}^3/\text{s}$ . The value for the metastable molecules  $N_2(A^3\Sigma_u^+)$  and  $O_2(b^1\Sigma_d^+)$  in air are unknown [9,13]. But by an indirect estimate, the discharges are characterized by a value of  $10^{-14}$   $\text{cm}^3/\text{s}$ . It's also interesting to note that the weakly ionized plasma is sustainable in negatively charged gas at a lower value of  $E/p$  than that by a short pulse discharge.

From the above brief discussion, the plasma generation and depletion processes are modeled as the following [30-32];

$$\begin{aligned} \frac{\partial n_e}{\partial t} - \nabla \cdot (n_e \mu_e \vec{E} + d_e \nabla n_e) &= \alpha(|\vec{E}|) |\vec{\Gamma}_e| - \beta n_+ n_e - \nu_a n_e + \kappa_d n_n n_- \\ \frac{\partial n_+}{\partial t} + \nabla \cdot (n_+ \mu_+ \vec{E} - d_+ \nabla n_+) &= \alpha(|\vec{E}|) |\vec{\Gamma}_e| - \beta n_+ n_e - \beta_i n_+ n_- \\ \frac{\partial n_-}{\partial t} - \nabla \cdot (n_- \mu_- \vec{E} + d_- \nabla n_-) &= \nu_a n_e - \kappa_d n_n n_- - \beta_i n_+ n_- \end{aligned} \quad (2-18)$$

In fact, the sum of the above equations satisfies fully the charge conservation law which is derived from the Maxwell equations [50]. Again in the above approximation; the number density of neutral particles of air,  $n_n$  is treated as a constant to have a value of  $2.69 \times 10^{19}/\text{cm}^3$ . The attachment frequency  $\nu_a$  is formally defined as  $\nu_a = (\alpha_a / p) u_{e,drift} \cdot p$ . In here, a commonly adopted value is  $(\alpha_a / p) = 0.005 / \text{cm} \cdot \text{torr}$ , and  $u_{e,drift}$  is the drift velocity of electron. From the drift-diffusion theory, the velocity can be consistently evaluated as  $u_{e,drift} = \mu_e |\vec{E}|$ .

The coefficient of ion-ion recombination  $\beta_i$  is estimated from the chemical kinetics of ionized and molecular nitrogen and oxygen to have a value of  $\beta_i = 1.6 \times 10^{-7}$ ,  $\text{cm}^3 / \text{s}$ . The detachment coefficient is estimated to have a range of  $10^{-14} < \kappa_d < 8.6 \times 10^{-10}$ ,  $\text{cm}^3 / \text{s}$ . This coefficient is important for the negatively charged ion number density computation; because it's the principal mechanism that governing the depletion of this species. Fortunately, its value can be verified by the discharged electrical current from experimental data.

The above model of electron collision ionization is actually replaced the energy conservation equations of the vibrational and electronic internal excitations, Equations (2-4) and (2-5), as well as, the law of mass action Equation (2-6) for chemical kinetics modeling. The electron attachment mechanism has been modeled to be proportional to the Townsend's ionization process for a non-physical but computational stability concern. In this approach, a portion of the negative-ion ionization is split from the electron generation [40].

In theory, the above ionizing models can be further improved by expanded the experimental data base or by *ab-initio* approach to the quantum chemical-physics. In this regard, the state-of-the-art status in low-temperature ionization modeling is similar to that of chemical-physics models by the approximated chemical reaction rates [13,41,47], but it has a decided advantage by substantially reducing computational resource required for simulations.

## 2.5 Electromagnetic Equations

The Maxwell's equations govern all electromagnetic phenomena and consist of the Faraday's induction law, the generalized Ampere's circuit law, and two Gauss' divergence equations for magnetic flux density as well as electric displacement [50]. For the DCD and DBD modeling, the governing equations including the boundary conditions are based on these fundamental laws of electromagnetics. The differential equations system is;

$$\begin{aligned}\frac{\partial B}{\partial t} + \nabla \times E &= 0 \\ \frac{\partial D}{\partial t} - \nabla \times H &= -J \\ \nabla \cdot B &= 0 \\ \nabla \cdot D &= \rho\end{aligned}\tag{2-19}$$

The associated boundary conditions of the differential system bounded by media interface can be summarized as;

$$\begin{aligned}\vec{n} \times (E_1 - E_2) &= 0 \\ \vec{n} \cdot (D_1 - D_2) &= \rho_s \\ \vec{n} \times (H_1 - H_2) &= J_s \\ \vec{n} \cdot (B_1 - B_2) &= 0\end{aligned}\tag{2-20}$$

The above boundary conditions require the parallel component of electric field strength  $E$  on a media interface to be unaltered, but the difference in the electric displacement component  $D$  across the interface must be balanced by the surface charge  $\rho_s$ . At the same time, the magnetic field strength  $H$  parallel to the medium interface needs to be balanced by the electric surface current  $J_s$ , and the normal component of the magnetic flux density  $B$  to the media interface is unchanged.

In most plasma based flow control environments, the Magnetic Reynolds number usually has a value much less than unity [4,6,19]. In the absence of an externally applied magnetic field its induced magnetic flux density is negligible and the electric field dominates the aerodynamic interactions of DCD and DBD. This simplification reduces the electromagnetic-aerodynamic interaction equations into the weak form. In this formulation the electrostatic force, Lorentz

acceleration, and Joule heating are appears as the source terms in the interdisciplinary equations, Equation (2-2) and (2-3).

In deriving the species concentration equation, the Maxwell equation is not explicitly include but the sum of Equations (2-2), (2-3), and (2-4) fully satisfies the charge conservation equation. This equation is obtained by taking the divergence of the generalized Ampere's circuit law and invoking the Gauss's law for the divergent free of the magnetic flux density [50];

$$\frac{\partial \rho_e}{\partial t} + \nabla \cdot \vec{J} = 0 \quad (2-21)$$

In the above equation, the electric charge density and the electric current density are defined as [30-32];

$$\begin{aligned} \rho_e &= e(n_+ - n_- - n_e) \\ \vec{J} &= e(\vec{\Gamma}_+ - \vec{\Gamma}_- - \vec{\Gamma}_e) \end{aligned} \quad (2-22)$$

The DCD and DBD plasma model is formally closed by the Poisson equation of plasmadynamics which satisfies the Gauss's law for the electric displacement,  $\nabla \cdot (\epsilon \vec{E}) = \rho$  and assumes the electric field intensity can be derived from the electrical potential. Specifically the electrical field intensity equals to the negative gradient of the electric potential,  $\vec{E} = -\nabla \phi$ . The resultant well-known Poisson equation appears as:

$$\nabla^2 \phi = \frac{e}{\epsilon} (n_e + n_- - n_+) \quad (2-23)$$

The appropriate boundary conditions for DCD and DBD simulations associate with the unique characteristic of different discharges will be discussed in the following sections.

It is recognized that the DBD modeling may not necessarily be adequate to describe the plasma sheath with free-space discharge separation, especially in conjunction with the Poisson equation of plasmadynamics. The shortcoming is the consequence that the compatible electric field is evaluated from the basic assumption, in that the electric field intensity is directly derivable from the electric potential. Numerous attempts have been made to improve this deficiency of plasmadynamics equation [26,27,48] including a Monte-Carlo simulation by Boeuf et al [49]. Although these improvements have captured some new details of the gas discharge phenomenon, but the basic approximation is still capable to predict all essential features with sufficient accuracy for the motion of partially ionized particles.

## 2.6 Numerical Procedure

The governing equations for DCD and DBD modeling are identical and the distinctive physics are generated by the different initial values and boundary conditions. The physics-based model consists of a mixed inhomogeneous hyperbolic and elliptic partial differential equations, Equations (2-18) and (2-23). The equations are source terms dominant and the eigenvalues of this differential equations system span a large range to make it very stiff for computation. A number of innovative measures must be introduced to ensure stability and accuracy of the numerical simulation. In the earlier efforts, the entire equations system was solved by a straightforward implicit scheme which possesses a narrow convergent band. Therefore a set of

stringent initial values must be specified to meet a converged tolerance within a reasonable time [31,32].

The most recent approach implements the total variation diminishing (TVD) discretization by an implicit time accurate marching scheme coupled with multigrid method, and the implicit boundary conditions on electrodes. The numerical procedure attempts to establish a computational stable and efficiency method for simulating surface DBD plasma actuator. First, the two-dimensional charged species conservation law, Eq. (2-18), is discretized over the control volume as shown in the following for the variable  $n_+$  ;

$$\begin{aligned} \frac{\partial n_+}{\partial t} = & - \left[ \frac{(n_+ E_x)_{(i+1/2,j)} - (n_+ E_x)_{(i-1/2,j)}}{\Delta x_{(i,j)}} + \frac{(n_+ E_y)_{(i,j+1/2)} - (n_+ E_y)_{(i,j-1/2)}}{\Delta y_{(i,j)}} \right] \\ & + \frac{1}{\Delta x_{(i,j)}} \left[ \left( d_+ \frac{\partial n_+}{\partial x} \right)_{(i+1/2,j)} - \left( d_+ \frac{\partial n_+}{\partial x} \right)_{(i-1/2,j)} \right] \\ & + \frac{1}{\Delta y_{(i,j)}} \left[ \left( d_+ \frac{\partial n_+}{\partial y} \right)_{(i,j+1/2)} - \left( d_+ \frac{\partial n_+}{\partial y} \right)_{(i,j-1/2)} \right] + s_+ - sn_+ \end{aligned} \quad (2-24)$$

In the above formulation, The diffusive terms were treated with the central differencing and the source terms are separated in two parts; for the term  $s_i$  does not explicitly contain the pertaining dependent variable  $n_i$  and the nonlinear term  $s$  is a product of collision process with other charged species. The typical convective flux on the control surface  $(n_+ E_x)_{(i+1/2,j)}$  can be expressed as:

$$\begin{aligned} (n_+ E_x)_{(i+1/2,j)} = & (E_x)_{(i+1/2,j)} [(n_+)_{(i,j)} + (n_+)_{(i+1,j)}] / 2 + |(E_x)_{(i+1/2,j)}| [(\Delta \tilde{n}_+)_{(i,j)} + (\Delta \tilde{n}_+)_{(i+1,j)}] / 4 \\ & - \left| (E_x)_{(i+1/2,j)} \right| + \left| (E_x)_{(i+1/2,j)} \right| / 2 \left[ (\Delta \tilde{n}_+)_{(i+1,j)} - (\Delta \tilde{n}_+)_{(i,j)} \right] / \left[ (n_+)_{(i+1,j)} - (n_+)_{(i,j)} \right] \\ & \left[ (n_+)_{(i+1,j)} - (n_+)_{(i,j)} \right] / 2 \end{aligned} \quad (2-25)$$

The TVD limiter by Yee's MINMOD scheme [51] is adopted as;

$$\Delta \tilde{n}_{(i,j)} = \tilde{s}_{(i,j)} \max[0, \min(|\Delta n_{(i+1,j)}|, \tilde{s}_{(i,j)} \Delta n_{(i-1,j)})] \quad (2-26)$$

where  $\Delta n_{(i+1,j)} = n_{(i+1,j)} - n_{(i,j)}$  and  $\tilde{s}_{(i,j)} = \text{sign}(\Delta n_{(i+1,j)})$ .

The discretized charged species conservation equations are expressible by a simple algebraic equation of the following form;

$$\begin{aligned} \frac{\partial n_{+, (i,j)}}{\partial t} = & a_{E, (i,j)} n_{+, (i+1,j)} + a_{W, (i,j)} n_{+, (i-1,j)} + a_{N, (i,j+1)} n_{+, (i,j+1)} + a_{S, (i,j)} n_{+, (i,j-1)} \\ & - (a_{P, (i,j)} + s_{(i,j)}) n_{+, (i,j)} + s_{+, (i,j)} \end{aligned} \quad (2-27)$$

One more step we took in this approach is to use the Delta formulation via the iteratively diminishing residual approach. By setting  $\delta n_+ = n_+^{**} - n_+^*$ , where  $**$  is the current iteration level and  $*$  is the previous iteration level, the discretized equations system can be summarized as;

$$\begin{aligned} \frac{\partial \delta n_{+, (i, j)}}{\partial t} = & a_{E, (i, j)} \delta n_{+, (i+1, j)} + a_{W, (i, j)} \delta n_{+, (i-1, j)} + a_{N, (i, j+1)} \delta n_{+, (i, j+1)} + a_{S, (i, j)} \delta n_{+, (i, j-1)} \\ & - (a_{P, (i, j)} + s_{(i, j)}) \delta n_{+, (i, j)} + RHS_{+, (i, j)}^* \end{aligned} \quad (2-28)$$

In Equation (2-28), the  $RHS_{+, (i, j)}^*$  is an abbreviation of the right-hand-side of Eq. (2-24), or Eq. (2-27), according to the diminishing residual delta formulation to be evaluated at the previous iterative level \*.

The third-order TVD type of Runge-Kutta algorithm for time advancement is applied by the consecutive implicit operators. The following formulations contain the RHS of Equation (2-27) at different fractional time steps and the previous time level to appear as;

$$\begin{aligned} \left[ \frac{1}{\Delta t} + a_{P, (i, j)} + S_{(i, j)}^n \right] \delta n_{+, (i, j)}^{(1)} = & a_{E, (i, j)} \delta n_{+, (i+1, j)}^{(1)} + a_{W, (i, j)} \delta n_{+, (i-1, j)}^{(1)} + \\ & a_{N, (i, j)} \delta n_{+, (i, j+1)}^{(1)} + a_{S, (i, j)} \delta n_{+, (i, j-1)}^{(1)} + RHS_{+, (i, j)}^n \\ n_{(i, j)}^1 = & n_{(i, j)}^n + \delta n_{(i, j)}^{(1)} \\ \left[ \frac{1}{\Delta t} + \frac{a_{P, (i, j)}}{4} + S_{(i, j)}^{(1)} \right] \delta n_{(i, j)}^{(2)} = & -\frac{3}{4\Delta t} \delta n_{(i, j)}^{(1)} + \\ \frac{1}{4} (a_{E, (i, j)} \delta n_{+, (i+1, j)}^{(2)} + a_{W, (i, j)} \delta n_{+, (i-1, j)}^{(2)} + a_{N, (i, j)} \delta n_{+, (i, j+1)}^{(2)} + a_{S, (i, j)} \delta n_{+, (i, j-1)}^{(2)}) + & \frac{1}{4} RHS_{+, (i, j)}^{(1)} \\ n_{(i, j)}^2 = & n_{(i, j)}^1 + \delta n_{(i, j)}^{(2)} \\ \left[ \frac{1}{\Delta t} + \frac{2}{3} a_{P, (i, j)} + S_{(i, j)}^{(2)} \right] \delta n_{(i, j)}^{n+1} = & -\frac{1}{3\Delta t} \delta n_{(i, j)}^{(2)} + \\ \frac{2}{3} (a_{E, (i, j)} \delta n_{+, (i+1, j)}^{n+1} + a_{W, (i, j)} \delta n_{+, (i-1, j)}^{n+1} + a_{N, (i, j)} \delta n_{+, (i, j+1)}^{n+1} + a_{S, (i, j)} \delta n_{+, (i, j-1)}^{n+1}) + & \frac{2}{3} RHS_{+, (i, j)}^{(2)} \\ n_{(i, j)}^{n+1} = & n_{(i, j)}^2 + \delta n_{(i, j)}^{n+1} \end{aligned} \quad (2-28)$$

Similarly, the Poisson equation of plasmadynamics, Eq. (2-23), can be discretized using the central differencing scheme. In the Delta formulation the equation yields;

$$a_{P, (i, j)} \delta \phi_{(i, j)} = a_{E, (i, j)} \delta \phi_{(i+1, j)} + a_{W, (i, j)} \delta \phi_{(i-1, j)} + a_{N, (i, j)} \delta \phi_{(i, j+1)} + a_{S, (i, j)} \delta \phi_{(i, j-1)} + RES_{\phi, (i, j)}^* \quad (2-29)$$

where RES is the residual value of Eq. (2-23), namely the RHS subtracting LHS. Both Equations (2-28) and (2-30) require a very efficient implicit solver. The SIP (Strong Implicit Procedure) or the ILU (Implicit Lower and Upper) decomposition scheme by Stone, or a modified version of it, MSIP, is adopted [52, 53]. The algorithm is very efficient for solving a sparse matrix equation system;  $AU = R$ . In here, U may be charge species;  $n_e, n_+, n_-$  or electric potential,  $\phi$ ; A is the five-point stencil matrix whose coefficients are made up from  $a$ 's shown in Eq. (2-29) and (2-30). By addition a complementary matrix C to the A, the resulting matrix, M, can be solved implicitly using the lower and upper matrix decomposition:



$$M = A + C \quad (2-30)$$

The identical implicit, iterative solving procedure is then;

$$MU^{**} = CU^* + R \quad (2-31)$$

Stone further introduced a partial cancellation term in both side of the Eq. (2-32) in order speed up the rate of convergence. The readers are referred to the original paper for the details of the procedure [52,53].

For the surface discharge phenomenon, the steep gradient always occurs near the corner of the exposed electrodes and dielectric surface, thus a high non-uniform mesh is generally recommended to solve the equations. Due to a large number of highly stretching grid points were used to cover the whole computational domain, the multigrid method offers the best solving option [54]. The multigrid method renders the error of the rapidly varying Fourier component to be first eliminated by the fine mesh system. The slowly decay error associated with the spectral radius becomes a smooth function. Through this implementation, an amazing convergent acceleration is observed, but the most important improvement to the numerical simulation is the computational stability by the combination of SIP (or MSIP), the implicit third-order Runge-Kutta scheme and TVD spatial discretization, which contributes greatly to the accurate of the numerical solution.

In Figure 1, the comparative study of the implicit solving schemes is depicted on a highly stretched (641 by 891) grid. The remarkable convergent acceleration from the conventional tridiagonal line relaxation (TDMA) to SIP and finally the combination of SIP and multigrid procedure is clearly illustrated. The acceleration in residual reduction by the SIP algorithm alone exceeds four orders of magnitude. The rate of convergence is further vastly improved by the combined application of the SIP and multigrid techniques, although the computational stability is not easily quantified but its impact is impressive. Through these superior computational attributes, the grid independent solutions are truly realizable.

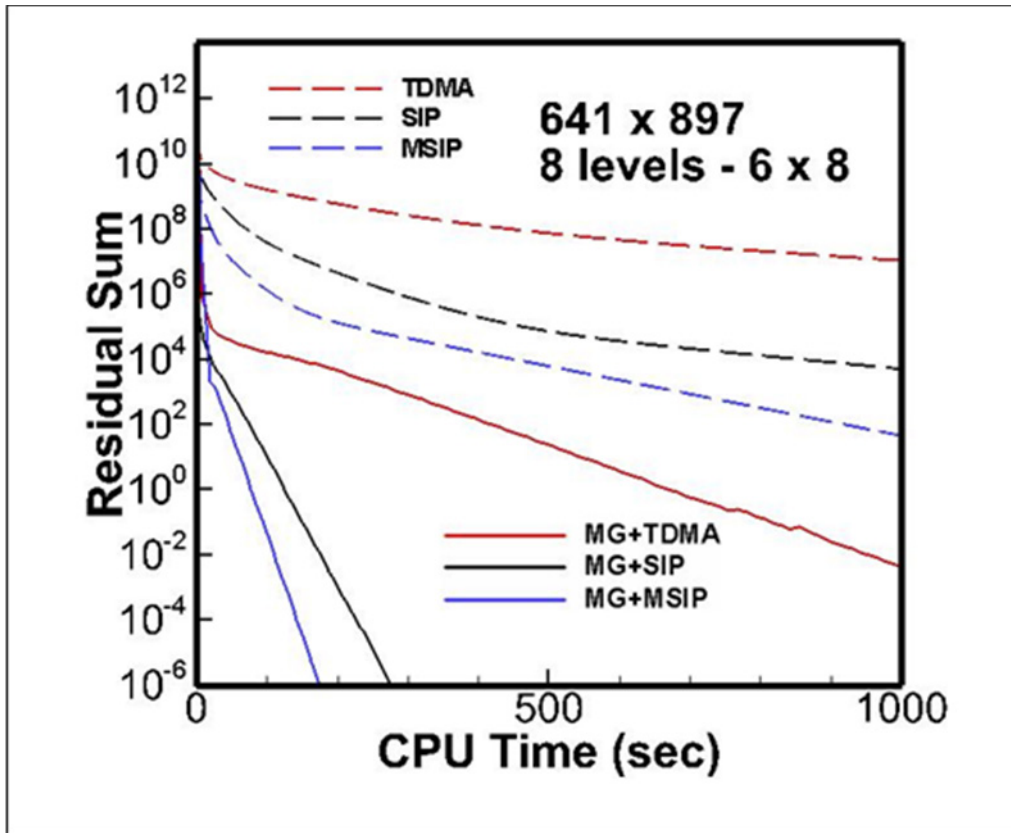


Figure 1 Iterative Convergent Acceleration for Solving Poisson Equation of Plasmadynamics

Figure 2 demonstrates the ability in achieving the grid independent solutions through the combination of SIP and multigrid technique. The electric field potential vectors are projected on the contours of the charge density distribution. A total three different nonuniform grids of (257×417), (641×897), and (1281×2049) are used. In the left side of the graph, the exposed electrode is positively biased, and the counter part of the negative polarity is at right side. All the solutions are interpolated to a fixed position for purpose of comparison. After the second grid density refinement, the difference between solutions is undiscernible.

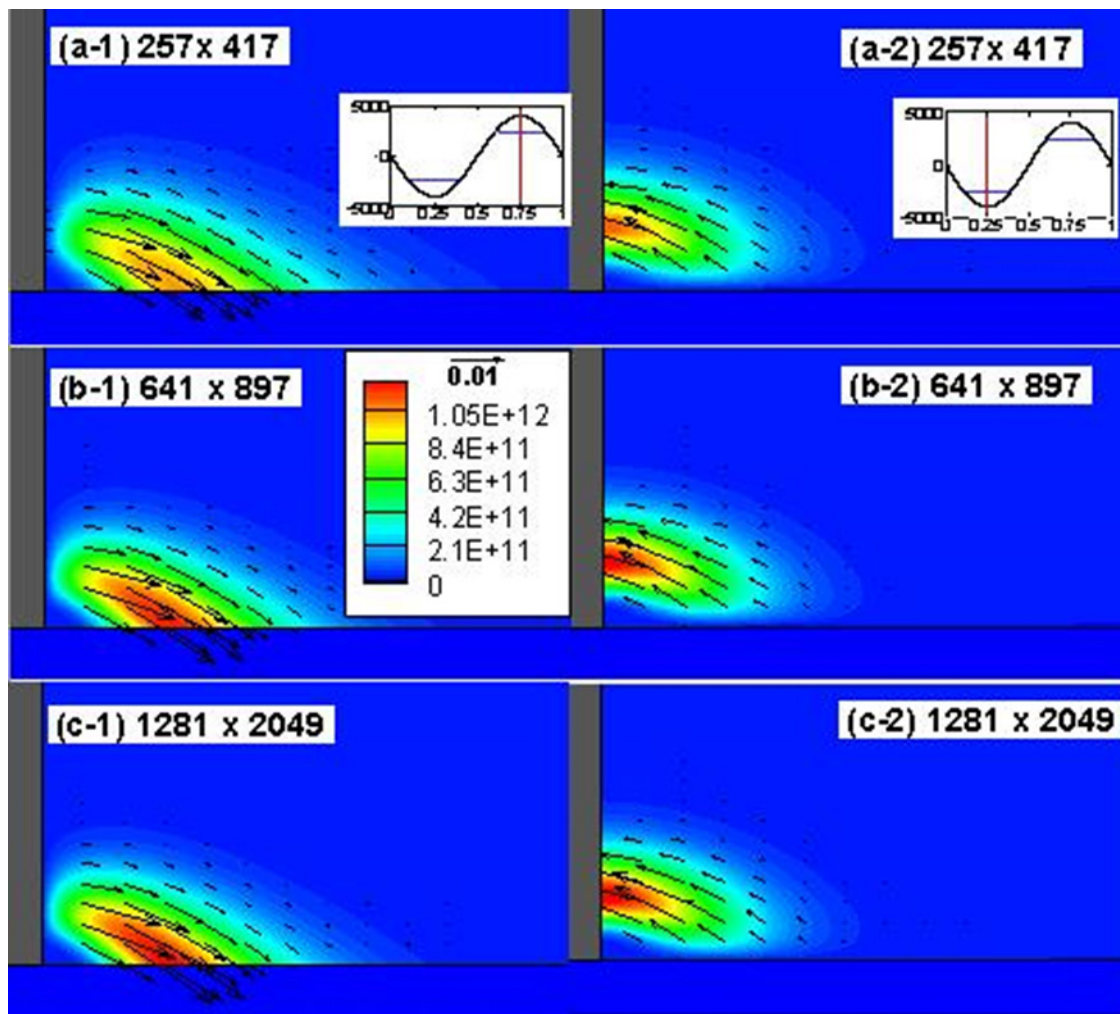


Figure 2 Grid Independent Studies

(a-1) to (a-3) are for positive cycle and (b-1) to (b-3) are for negative cycle. Contours show the charged density distribution and vectors are the force field. The solutions were interpolated to fixed position for purposes of comparison.

## 2.7 Boundary Conditions of Direct Current Discharge

The effect of DCD in applications to flow control is derived from the dissipative Joule heating of the discharge [4-6]. However, the thermal effect also includes the electrode heating from the metallic electrodes and mostly over the cathode. The electrodes generally have two typical configurations; the parallel electrodes separated by a gap distance  $d$ , and the side-by-side arrangement. The boundary condition for DBD is straightforward:

On the cathode, the electric field potential vanishes on metallic surface, all negatively charged ions are repelled, and the number density of the positively charged ions reaches the cathode unaltered. The secondary electron emission is the result of the Penning tunneling through a very strong electrical field intensity in the cathode layer generated by the positive-ion accumulation immediately adjacent to the solid surface. The quantification of the electron emission from the cathode by positively charged ions is described by an emission coefficient  $\gamma$  which has a well-known value range from 0.01 to 0.1, depending on the electrode material [7,28,29]

$$\begin{aligned}
\varphi &= 0 \\
n_- &= 0 \\
\vec{n} \cdot \nabla n_+ &= 0 \\
\vec{n} \cdot \vec{\Gamma}_e &= -\gamma \vec{n} \cdot \vec{\Gamma}_+
\end{aligned} \tag{2-32}$$

On the anode, all the positively charged ions are repelled. The negatively charged ions and electron number densities are unaltered when reached the anode surface. The electric potential on the anode is the balance of the electromotive force, EMF and the loss along the external circuit.

$$\begin{aligned}
\varphi &= EMF - IR \\
\vec{n} \cdot \nabla n_- &= 0 \\
n_+ &= 0 \\
\vec{n} \cdot \nabla n_e &= 0
\end{aligned} \tag{2-33}$$

where the symbol  $I$  is the total electrical current and  $R$  is the resistance of the circuit including the discharging column.

The boundary conditions on the farfield boundaries are uniformly imposed by the vanishing outward normal gradient approximation to describe the vanishing electrical field potential;

$$\begin{aligned}
\vec{n} \cdot \nabla \varphi &= 0 \\
\vec{n} \cdot \nabla n_- &= 0 \\
\vec{n} \cdot \nabla n_+ &= 0 \\
\vec{n} \cdot \nabla n_e &= 0
\end{aligned} \tag{2-34}$$

## 2.8 Characteristics of DCD

The typical DCD computational simulations are conducting at the ambient pressure levels from nearly vacuum up to 50 Torr by an electromotive force (EMF) up to 9 kV. The electric current density is usually limited around 10 mA/cm<sup>2</sup>. The classic DCD discharge structure has been examined by the parallel electrodes arrangement and is implemented by the side-by-side configuration for flow control. In general, the dimension of discharge domain is proportional to the magnitude of the applied EMF and inversely proportional to the ambient pressure, to be precise, the ambient gas density. The important current voltage relationship has been studied by the classic work by Engel and Steenbeck in one-dimension [55] and most recently by Rafatov et al. by an elaborate drift-diffusion model [56]. At the low current density and due to the greater electron mobility; the ion number density usually exceeds the electron counterpart within the entire discharge domain.

Figure 3 depicts the contours of electron and positively charged number density of the DCD within a parallel electrode configuration. The diffusive discharge is generated between a gap distance of 2.0 cm by an EMF of 2.4 kV at an ambient pressure of 5 Torr. On the cathode all the electrons are repelled, but the secondary emission generates a rapid avalanche in the positive column. The positively charged ions are clustered in the cathode layer to reach the maximum number density of  $3.0 \times 10^{10}/\text{cm}^3$ . Although the electron temperature is not including in the simulation, but the highest value from the classic work is known to exist in the cathode layer and has a value around 3 eV [7,55].

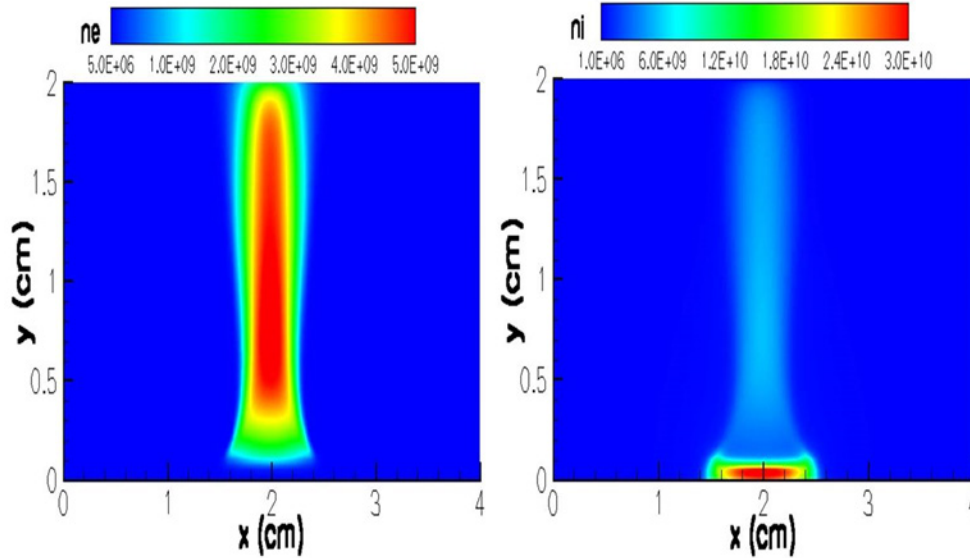


Figure 3 Electron and Positively Charged Ion Number Density Contours of Parallel Electrodes  
 $p=5$  Torr,  $EMF=2.0$  kV,  $gap=2.0$  cm

In Figure 4 by increasing the ambient pressure from 3 to 10 Torr, the electric field intensity is increasing proportionally [55]. The distinct cathode fall is captured by the two-dimensional computational simulations. In fact, the intensities drop by nearly two orders of magnitude from the cathode layer to the positive column. At the pressure of 10 Torr, the maximum normal electric field intensity on the cathode exceeds the value of  $8.0 \times 10^3$  and decreases to a value of  $3.5 \times 10^2$  V/cm in the positive column and rises moderately on the anode. The computational result at  $p=5$  Torr agrees well to the early effort by a different numerical algorithm as a validation [4,5,33]. An interesting observation is also made in that by lower the value of the secondary emission coefficient,  $\gamma$ ; the thickness of the cathode layer increases accordingly. This effect also produces a drop in electric field intensity and the normal current density which means that by lowering the secondary emission coefficient actually reduces the ionizing efficiency in the cathode layer.

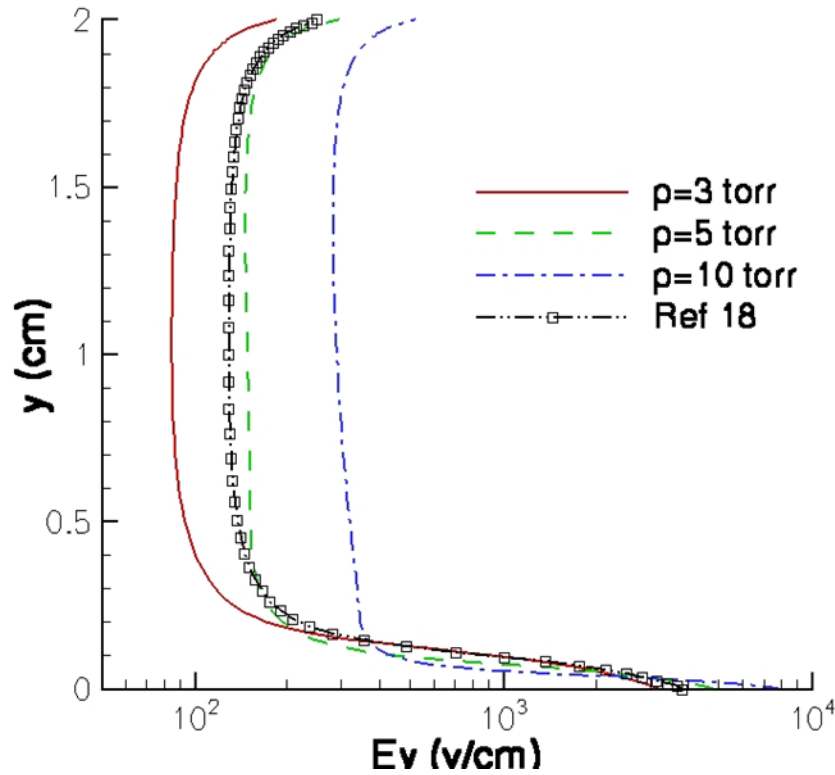


Figure 4 Surface Normal Electric Field Intensity  
 $EMF=2.0kV$ ,  $gap=2.0cm$

In the DCD modeling, the electrode heating is rigorously determined by the Fourier's law for conductive heat transfer, and the dissipative Joule heating can be evaluated by the current density and the electrical field intensity induced by the discharge. The temperature of the neutral particles has been simulated by Petrusiv et al. [57] by assuming a constant electron temperature of 1 eV ( $1.1604 \times 10^4$  K). It is anticipated that the maximum value of the temperature is located deeply in the cathode layer. Realistically, the nonequilibrium electron temperature is not an invariant in the discharge domain and has been described by an empirical equation of reduced field intensity  $|\vec{E}|/P$ ;  $T_e/T = 29.96 \ln(|\vec{E}|/p) + 24.64$ . The typical DCD experiment for hypersonic flow control is generated around an EMF of 2 kV and at a pressure level of 5 Torr which has exceeded the reduced electrical field intensity of the original empirical relationship. For the purpose of illustration, the electron temperature contour of a DCD is depicted in Figure 5. Again, the maximum electron temperature is observed to be embedded within the cathode layer and decay rapidly in the positive column toward the anode and far field. The range of electron temperature variation within a DCD is indeed modest,  $1 < T_e < 2.8$  eV.

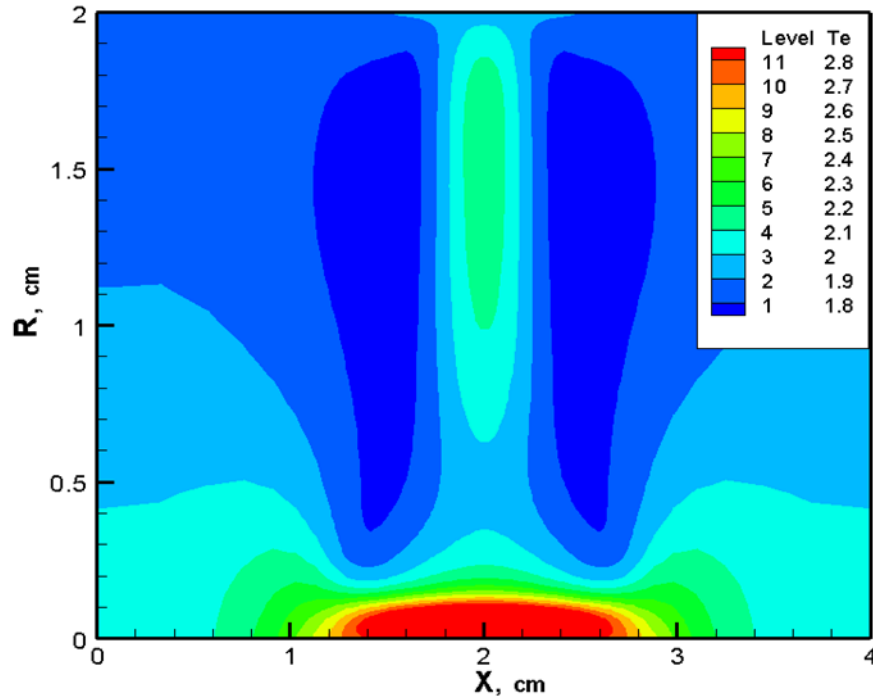


Figure 5 Electron Temperature Profile with a DCD Discharge  
 $EMF=2.0\text{ eV}$ ,  $P=5.0\text{ Torr}$

The DCD structure is presented in Figure 6 by a side-by-side electrodes configuration as the most flow control applications. The DCD is generated at an EMF of 2.4 kV, a pressure level of 5 Torr, and with the gap distance between electrodes of 2.0 cm. The cathode is placed on the left of the anode in the composite presentation. On the left-hand side of the inset, the discharge current vector traces are appended to the electron number density contour. On the right-hand side of the inset, the electric field intensity vector traces are superimposed over the positively charged ion number density. The maximum electron density over the anode is  $3.02 \times 10^{10}$  and the positively charged ion is located over the cathode with a maximum value of  $5.76 \times 10^{10}/\text{cm}^3$ . The basic DCD structure is still identifiable such as the positive column, cathode and anode layers to that of the parallel electrodes arrangement, but the discharge domain becomes pronounced biased by the different gap distance between electrodes. However, the average cathode-layer thickness is still maintained at 0.125 cm, which is comparable to the result of the parallel electrodes configuration.

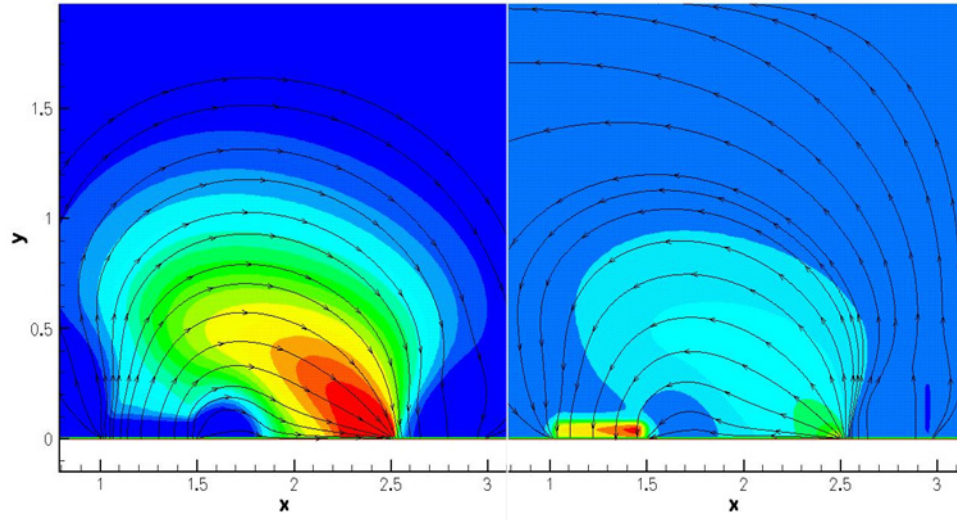


Figure 6 Electron and Ion Number Density  
*Contour and charge current density (left), ion number density and electric field intensity (right);*  
*EMF=439V, I=5.20 mA, p=5 Torr*

It is also interesting to note that the strong electric field vector is perpendicular downward to the cathode and the field intensity is nearly parallel to the dielectric surface between electrodes toward the cathode. All the field intensity traces are highly concentrated at the edges of the electrodes to indicate a high gradient electric field region locally.

The electron number density obtained from Langmuir probe measurements within a DCD field is shown in Figure 7. A 60 mA discharge current is maintained by an electrical potential at 1.2 kV over the side-by-side electrode arrangement [33]. Surveys are conducted on the plate centerline and the cathode is placed to the left of the anode. The electron number density is presented as a function of  $x$  at four different heights above the electrode surface. The electron number density is highest near the plate surface, and decreases away from the plate. Peak number densities of about  $10^{12} \text{ cm}^{-3}$  are obtained over the cathode, and the measured value is comparable with the numerical results under the similar condition. The lowest electron concentrations are still measurable at 0.5 cm above the plate surface downstream of the cathode, but the number density at this height drops off rapidly upstream and downstream from this location



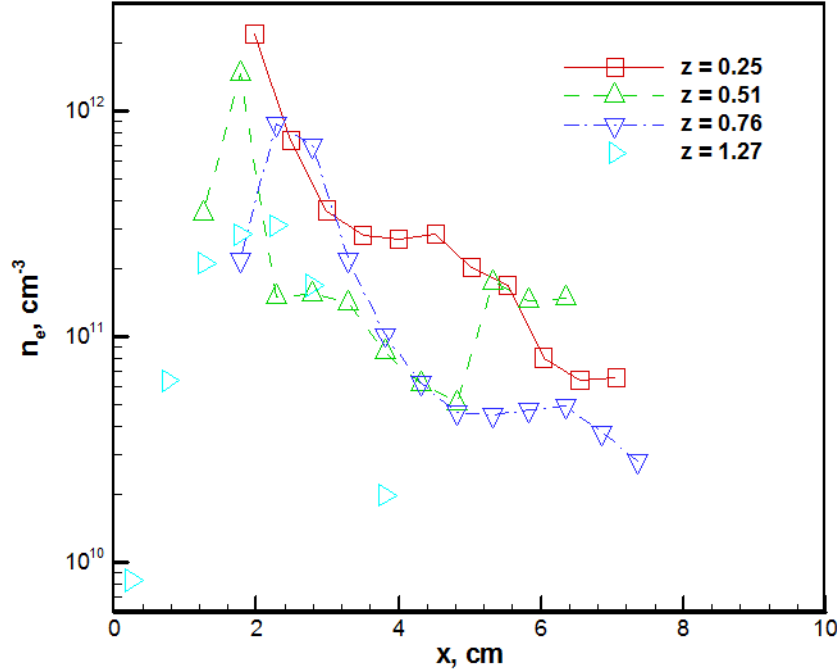


Figure 7 Measurement of Electron Number Density  
(over a side-by-side DCD configuration by a Langmuir Probe,  $\phi=1.2$  kV,  $I=60$  mA,  $p=1.0$  Torr)

The behavior of the electric field intensity at the edges and over the electrodes is highlighted by Figure 8. The two-dimensional simulation is conducted for the side-by-side configuration with the electrodes dimension of 0.5 cm in length and the gap distance of 1.0 cm. The outer edges of the electrodes are placed at the 1.5 cm from the outer boundaries of the computational domain. In order to resolve the high intensity field, a nonuniform  $250 \times 120$  mesh system is used with a minimum horizontal grid spacing of  $5 \times 10^{-3}$  cm and a minimum perpendicular spacing of  $1.671 \times 10^{-3}$  cm clustering to the electrodes. The normal electric field intensities over the cathode at different ambient pressure have the averaged value around 5kV/cm, but rise sharply to four times the value at the edges of electrode. Similar behaviors are also exhibit over anode but with a much less intensity. This phenomenon is well-known in electric circuit design and especially in discharge physics [7,8].

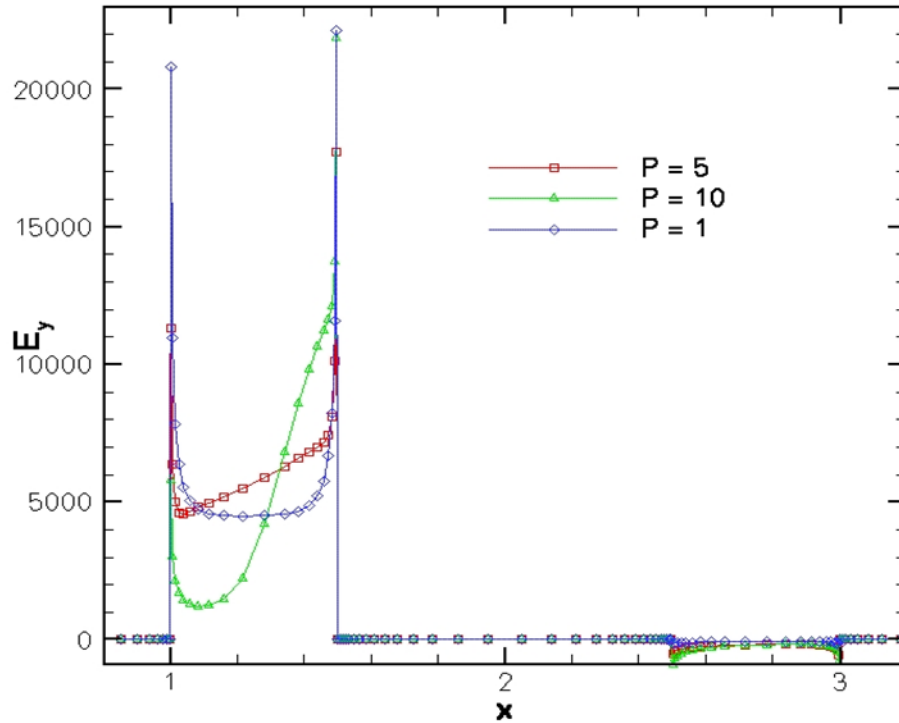


Figure 8 Normal Electric Field Intensity  
 $EMF=2.0\text{ kV}$ ,  $gap=0.5\text{ cm}$ ,  $electrode\ length=1.0\text{ cm}$

The most important flow control mechanism of DCD by Joule heating distribution is depicted in Figure 9. The volumetric heating occurs mainly within the cathode layer at the inner edge of the cathode toward the anode. A hot spot also appeared on the inner edge of the anode but with a much less intensity. From the numerical simulation, the Joule heating release to the discharging domain is  $1.3\text{ J/s}\cdot\text{cm}^2$ . This value is relatively small in comparison with the total amount of power for the surface DC plasma generation of  $21.52\text{ J/s}\cdot\text{cm}^2$ . The Joule heating contributes about 50% to the total heat flux from the DCD in comparison with the electrode heating at the simulated condition, and this ratio has been verified by experimental measurements [4,5,32]. The advantage of the Joule heating is beyond the electrode surface but extends into the flow field. In all, the net effect of Joule heating is created a local thermal expansion to the flowfield and alters the boundary-layer displacement thickness and thus the local slope of a control surface. The outward displaced surface slope always triggers a family of compression waves by the external supersonic stream to generate the flow control mechanism [4,5,19].

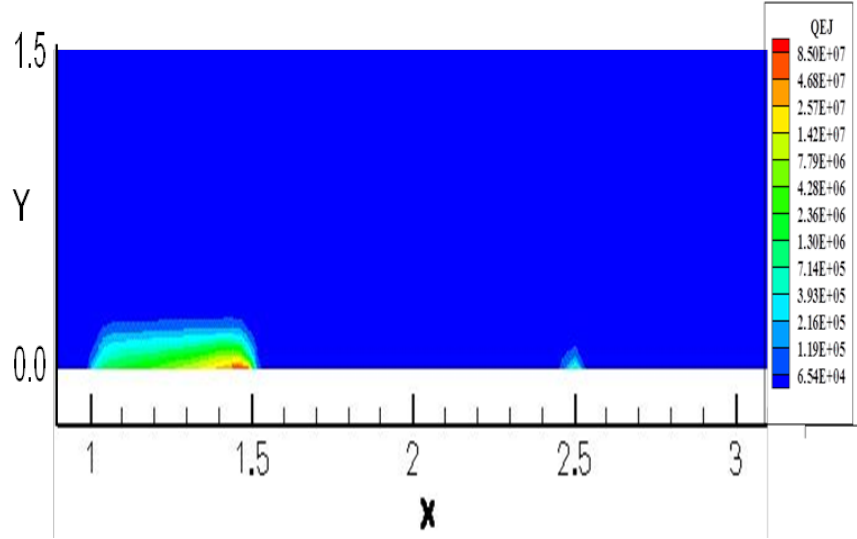


Figure 9 Joule Heating Contour  
(over side-by-side direct current discharge,  $E=439.4$  V,  $I=5.20$  mA,  $p=5.0$  Torr, Gap=1.0cm. Joule heating 1.3 Watts, DCD power supply 21.52 Watts)

The global effect of the externally applied magnetic flux density to DCD and the comparison with experimental observation is given by Figure 10. The computational simulations are comparing with the experimental observation in at Mach number of 5.15 at the identical condition of a pressure of 1.0 Torr, a temperature of 43 K, and by an EMF of 1.2 KV. The transverse magnetic flux density of  $\pm 0.1$  Tesla is applied with opposite polarities across the side-by-side electrodes by a gap distance of 2.45 cm. At the relatively low externally applied magnetic field, the Lorentz force exerts a significant influence to the discharge structure. According to the right-hand rule and in the specific experimental arrangement, the positive polarity in the applied transverse magnetic field expels the plasma away from the electrode surface by the Lorentz force. By reverse the polarity of the magnetic field, the plasma is suppressed toward the electrode. At the relatively low magnetic flux density of 0.1 Tesla, the externally applied magnetic field exerts a profound change to the DCD structure.

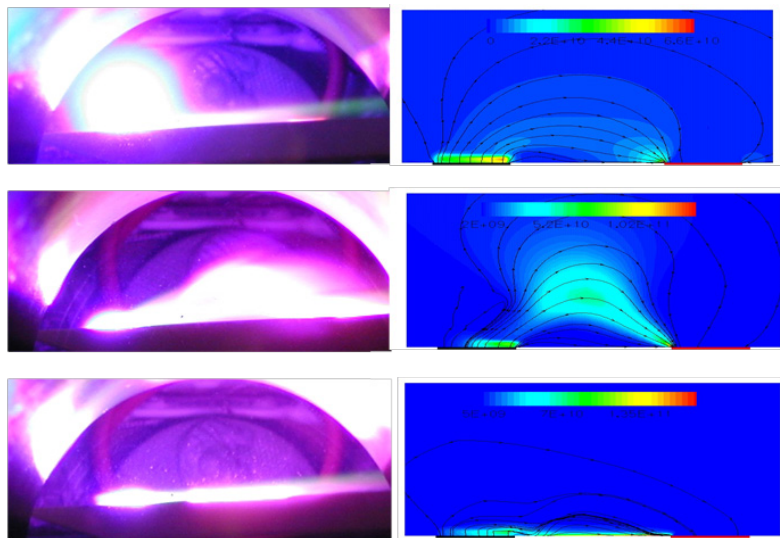


Figure 10 DCD in Transverse Magnetic Field,  $B_z=0$ ,  $B_z=-0.1$ , and  $B_z=+0.1$

The detailed electrical current vectors of DCD in the presence of an externally applied transverse magnetic field are given in Figure 11. The computational simulation mimics the experiment, except by a smaller computational dimension (electrodes of 0.5 cm in length and 1.0 cm apart), a weaker magnetic flux density of 0.05 Tesla, but at a stronger EMF of 2.0 kV. The corresponding Hall parameter of the electron and ion are  $\beta_e = \mu_e B_z = \pm 0.440$  and  $\beta_i = \mu_i B_z = \pm 0.0014$  respectively. The numerical simulations are in agreement with experimental observation in that the polarity of the applied magnetic field may increase plasma generation to sustain a fixed discharge electric current. In the numerical simulation at  $B = -0.05$  Tesla, the Lorentz acceleration pushes the charged particles, thus the discharge current away from the electrodes, and concentrates the current toward the inner edges of the electrode pairs. The opposite effect is displayed at  $B = +0.05$  Tesla: The discharge electrical current is suppressed over the dielectric surface between electrodes. The discharge current is nearly parallel and confines to the surface strait. The effect for a greater flow control effectiveness has also been recorded by experimental observations [4,5,23-25,33].

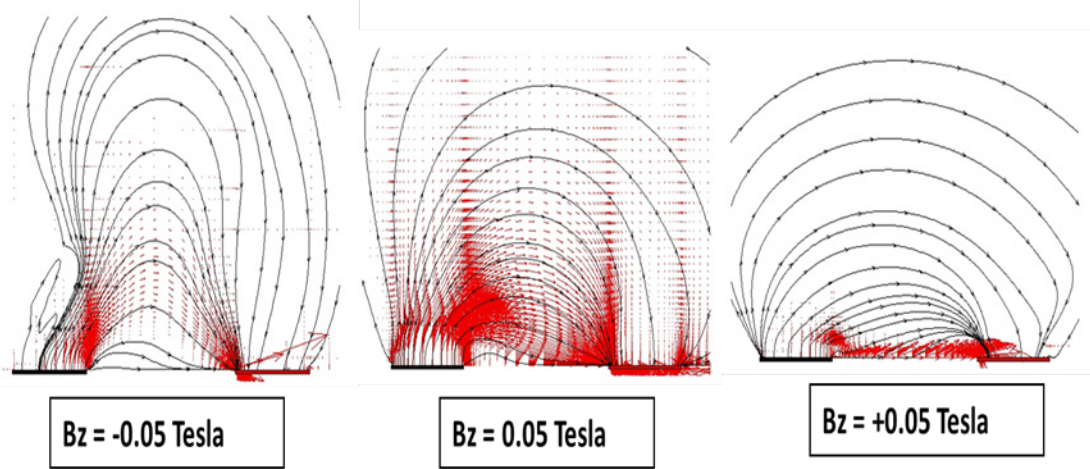


Figure 11 Electrical Current Vectors in the Presence of an Externally Applied Magnetic Field  
1.0 cm separation distance between electrodes, EMF=2.0 kV, P=5 Torr.

## 2.9 Boundary Conditions of Dielectric Barrier Discharge

The dielectric coating is the key component for the proper DBD operation, because it limits the amount of charge transported by a single microdischarge and distributes the microdischarges over the entire electrode [9-11]. Therefore one of the electrodes is always encapsulated by dielectric material and is often grounded [3]. Despite numerous computational simulations, some computational simulations have not imposed the correct media interface boundary condition for describing this key physical phenomenon of DBD [44-46].

According to the theory of electromagnetics, the electric field across the dielectric and plasma interface must satisfy the following conditions [19,50];

$$\vec{n} \times (E_d - E_p) = 0, \quad (2-35)$$

$$\vec{n} \cdot (D_d - D_p) = \rho_{e,s}. \quad (2-36)$$

In the above equations, the subscripts  $p$  and  $d$  designating the variables either reside in plasma medium or on the dielectrics. The local surface charge density is evaluated by integrating the net

charged number density over an infinitesimal normal distance over the control surface, and is defined as  $\rho_{e,s} = e \int (n_+ - n_e - n_-) d\sigma$  which has a dimension of coulombs/cm<sup>2</sup>.

Equation (2-35) simply states that the tangential electrical field strength is continuously across the media interface. It can be shown on the Cartesian frame, the rate of change for electric potential in z,  $\partial\phi/\partial z$ , must be identical across the interface along the x coordinate. Similarly, the rate of change of electrical potential in x,  $\partial\phi/\partial x$ , must be equal along the z coordinate across the media interface. This requirement is automatic satisfied by the two-dimensional formulation.

The discontinuity of the normal component of the electric displacement,  $D$ , across different media must be balanced by the net surface charge on the interface by emission, desorption, and accumulation. In fact, the condition defined by equation (2-36) is independent of all chemical-physics processes on the medium interface. And this equation is further developed by introducing the electric potential for the partially ionized plasma,  $E = -\nabla\phi$  to become;

$$\varepsilon_p \frac{\partial\phi_p}{\partial n} - \varepsilon_d \frac{\partial\phi_d}{\partial n} = \rho_{e,s}. \quad (2-37)$$

In the above equation,  $\varepsilon_p$  and  $\varepsilon_d$  denote the electric permittivity of the plasma and dielectrics respectively. For the weakly ionized gas, the relative value of  $\varepsilon_p$  is around unity and for  $\varepsilon_d$  has a magnitude up to 7.0 from polystyrene to rubber [46].

On the dielectric barrier, the surface diffusion and desorption can be modeled by the collisions of excited molecules and atoms by their collision frequency and the binding energy [15]. The charge accumulation on surface is considered as the result from the instantaneous recombination of the charge particles after satisfied the imposed boundary condition for the species concentration. For the two-dimensional formulation, equation (2-37) reduces to the following form;

$$\frac{\partial\phi_p}{\partial n} = \frac{\varepsilon_d}{\varepsilon_p} \frac{\partial\phi_d}{\partial n} + \frac{e}{\varepsilon_p} \int (n_+ - n_e - n_-) d\sigma. \quad (2-38)$$

Equation (2-38) is the critical boundary condition to be imposed on the dielectrics. All other physics meaningful boundary conditions on the interface have been demonstrated to be robust and accurately described the behavior of weakly ionized gas generated by electron collision [43-46].

In DBD operation, the distinguish discharge phenomena during an AC cycle is frequently referred to as the forward stroke or negative going and the back stroke or positive going [10,11]. In fact, the discharge is exclusively governed by the polarity of the electrodes [9,44-46]. When the electrical potential is positive,  $\phi(t) > 0$  on the exposed electrode, it performs as the anode on which the electrical potential is dictated by the externally applied AC current source with a frequency of  $\omega$ , and all positively charged ions are repulsed. The imposed boundary condition on the anode or the exposed electrode are;

$$\phi(t) = EMF \sin(\omega t), \quad (2-39)$$

$$n_+ = 0, \quad (2-40)$$

$$\vec{n} \cdot \nabla n_e = 0 \text{ and } \vec{n} \cdot \nabla n_- = 0. \quad (2-41)$$

The  $EMF$  is the external voltage applied to the DBD circuit. It shall be immediately recognized that the electric field potential across the exposed and the dielectric barrier after the breakdown is determined by the external circuit equation;  $EMF = \varphi + R \int \bar{J} dv$  [11,14,15], and the electric current density of the discharge is simply,  $\bar{J} = e(\bar{\Gamma}_+ - \bar{\Gamma}_e - \bar{\Gamma}_-)$ .

At this same instant, the dielectric barrier surface acts as the cathode on which the secondary electron emission is induced by an excessive accumulation of positively charged ions over the dielectric barrier to reduce the effective difference in electric potential. At this AC phase, the imposed boundary conditions on the cathode for the electrical potential and charged particle concentration on the dielectric shall be:

$$\vec{n} \cdot (\nabla \varphi)_p = \vec{n} \cdot \left( \frac{\mathcal{E}_d}{\mathcal{E}_p} \right) (\nabla \varphi)_d + \frac{e}{\mathcal{E}_p} \int (n_+ - n_e - n_-) d\sigma, \quad (2-42)$$

$$\vec{n} \cdot \nabla n_+ = 0 \text{ and } n_- = 0, \quad (2-43)$$

$$\bar{\Gamma}_e = -\gamma_d \bar{\Gamma}_+. \quad (2-44)$$

During this AC cycle, Equation (2-42) ensures diminishing electrical field intensity across the electrodes through the surface charge accumulation. It is also the fundamental mechanism of the self-limiting characteristic in preventing DBD transition to spark. Again, equation (2-44) enforces the electron secondary emission condition for the Townsend's discharge [7,8]

When AC field switches polarity to a negative electric potential,  $\varphi(t) < 0$ , on the exposed electrode: the roles of the exposed electrode and the dielectric barrier surface also reverses. The exposed electrode now functions as the cathode; the secondary emission by the positive-ion accumulation now occurs over the metallic surface. The coefficient of the emission on the metal surface,  $\gamma_m$  is different from that of the dielectrics.

During this AC phase, the boundary conditions on the cathode or the exposed electrode are;

$$\varphi(t) = -EMF \sin(\omega t) \quad (2-45)$$

$$\vec{n} \cdot \nabla n_- = 0 \text{ and } n_+ = 0, \quad (2-46)$$

$$\bar{\Gamma}_e = -\gamma_m \bar{\Gamma}_+. \quad (2-47)$$

On the dielectric surface or the grounded anode at the same time, the boundary conditions are;

$$\varphi(t) = 0, \quad (2-48)$$

$$n_+ = 0, \quad (2-49)$$

$$\vec{n} \cdot \nabla n_e = 0 \text{ and } \vec{n} \cdot \nabla n_- = 0. \quad (2-50)$$

To complete the boundary conditions specification for the DBD simulation, the vanishing gradient condition is imposed uniformly on the farfield boundary of the computational domain for all four dependent variables. For the multiple length- and time-scales phenomenon; the ionization and recombination of charge particles is considered to be instantaneous in comparison

with the time scale of the alternative electric field. Therefore no separate boundary condition treatment is imposed during the switching AC cycle.

It may be noticed the imposed boundary conditions for DBD on the exposed electrode and the dielectric surface are fully reinforced the DBD self-limiting mechanisms. The boundary conditions specification must be synchronized with the alternating polarities of the electrode. The differences appear only in the secondary emission coefficients on the cathode and the effective electrical potential across the discharging domain.

## 2.10 Characteristics of DBD

The partially ionized gas existing in the discharging domain is generated through a succession of random streamer formations in space and time for the duration of few nanoseconds [9-11]. In application, the DBD generally operates at atmospheric pressure with a gap distance on the order of one to a few millimeters between electrodes. An alternative voltage is required to support the random transient streamer formation in the electrode gap and quenching by the localized charge build-up on the dielectric layers. The partially ionized gas between the gap of electrodes is generated through the succession of a large volume of glow discharge and random streamers in space and time [3,9-11]. Gherardi et al. [58] recently have shown that when the DBD occurs in many thin filaments will lead to multiple microdischarges and by a single discharge channel over the entire electrode surface to become a glow discharge. Through the emission spectroscopy and electrical measurements, the transition from the filamentary structure is controlled by the density of metastable nitrogen molecules, but the seeding electrons are always created by the Penning effect.

Specifically, when the exposed electrode is positively biased in an AC cycle, the discharge is characterized by a streamer like structure. In the negatively biased phase, the discharge appears as a more diffusive structure. In essence, the DBD discharges are operated in the micro-discharge mode whose nanoseconds life span is governed by the ionization-recombination process. On the other hand, the propagation of charged particles is synchronized to the frequency of the AC field. Meanwhile the induced electrostatic force by the free-space charge separation in the AC cycle becomes a repetitive dynamic event. In Figure 12, this dynamic event is described in a composite presentation based on experimental observations in a typical voltage-current curve by Moreau [3] and high-speed photography by Enloe et al. [10,11].

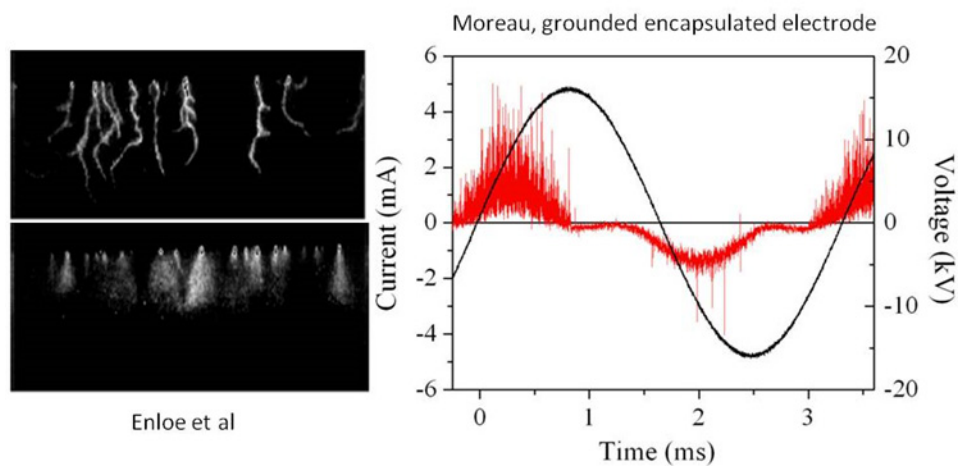


Figure 12 Voltage-current Curve and Discharge Photos Exposed Electrode Anode (U) and Cathode (L)

The important comparison of the periodic voltage-current characteristic of computational results with experimental data over 1,000 microseconds (five AC cycles at 5 kHz) is depicted in Figures 13. The comparison with data at the externally applied electrode potential of 4.0 kV reveals a good overall affinity between data and computational results at the instant of breakdowns. Prior to the breakdown, the electrical current consists only of the displacement component. After the plasma ignition, the electrical current has an additional conductive component of the DBD. The magnitude of this component is relatively minuscule and indicates a current density less than 0.008 mA/cm. This calculated value agrees well with data collected over a wide group of experiments to indicate the ionization model by the chemical-physics kinetics is credible [3,59].

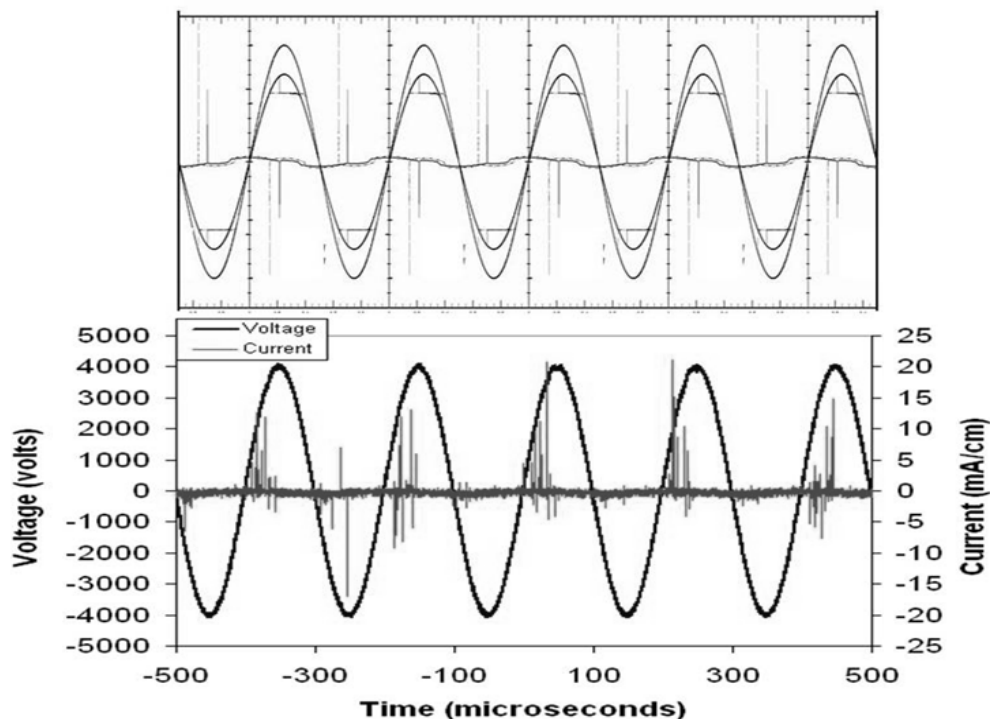


Figure 13 Compare Voltage-current Curves (5kHz) with Experimental Observation

In Figure 14, the fundamental self-limiting characteristic of the DBD is convincingly captured by the computational simulation at the externally applied electrical potential of 3.0 kV and 5.0 kV across the overlapped electrodes. At the quiescent atmospheric condition, the discharge breakdown takes place at a voltage of 2.77 and 2.65 kV, for 5.0 kV and 3.0kV, respectively, before the externally applied electrical field reaches its peak values for both polarities. Then a lower and constant electric potential of 2.5 kV is maintained by the conductive current and by the surface charge accumulation on the electrodes. The numerical result duplicates the pattern of experimental surface potential measurements [10,11]. In the positive polarity phase, the discharge occurs when the positive-going potential exceeded the breakdown voltage and continues until the negative-going external field falls beneath the breakdown threshold. The identical behavior is also observed for the negative polarity phase. During the initial breakdown process, a sudden drop of the electric potential with respect to time induces a surge of the displacement current in the discharge. In experimental measurements, this surge indicates the existence of multiple micro discharges and also knows to induce a train of pulsations in the electrical circuit [3,9-11,59]. Similarly the sudden drop of the electric potential has also



generated non-physical oscillations by the numerical simulation known as the Gibbs phenomenon [37-41,43-45].

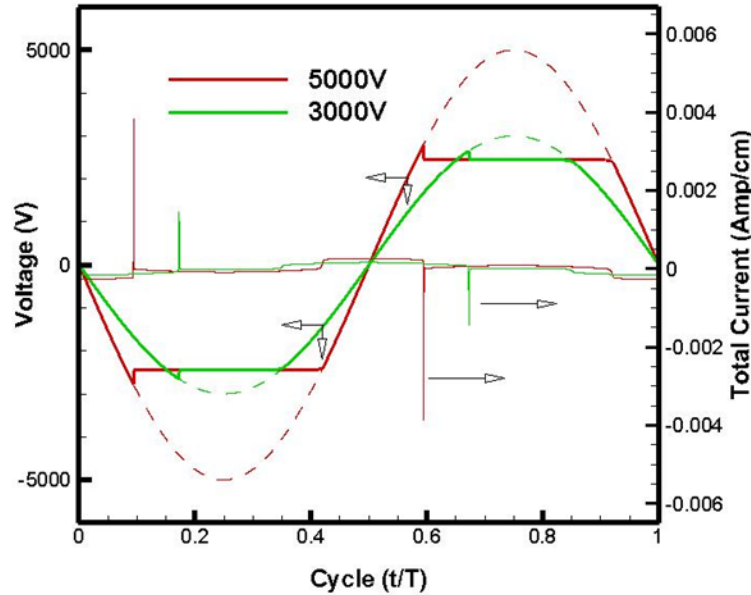


Figure 14 Effect of Discharge duration with Different EMF

The domain of the positively charged ion at the peak positive voltage is compared at 3kV, 5kV, and 8 kV in Figure 15. The discharge domain retains the similar shape but its dimension is noticeably affected by the driving voltage. The charged ion density drops exponentially from its peak value near the corner of the exposed electrode and the dielectric wall to the ambient. The maximum positively charged ion number density increases from  $4.3 \times 10^{11}$ ,  $1.9 \times 10^{12}$ , to  $4.0 \times 10^{12}$  per  $\text{cm}^3$  with the increasing intensity of the applied voltage. The number of electron density is also increasing proportional with the rising intensity, but at a two-order of magnitude lower value than that of the ion. The combination of a higher charge number density and a longer discharge duration leads to a great periodic electrostatic force to agree with experimental observation [3]. The maximum instantaneous magnitude of the force generated at 8 kV is more than double that of 5kV, to be as high as  $2.7 \times 10^5$  dyne/ $\text{cm}^3$ .

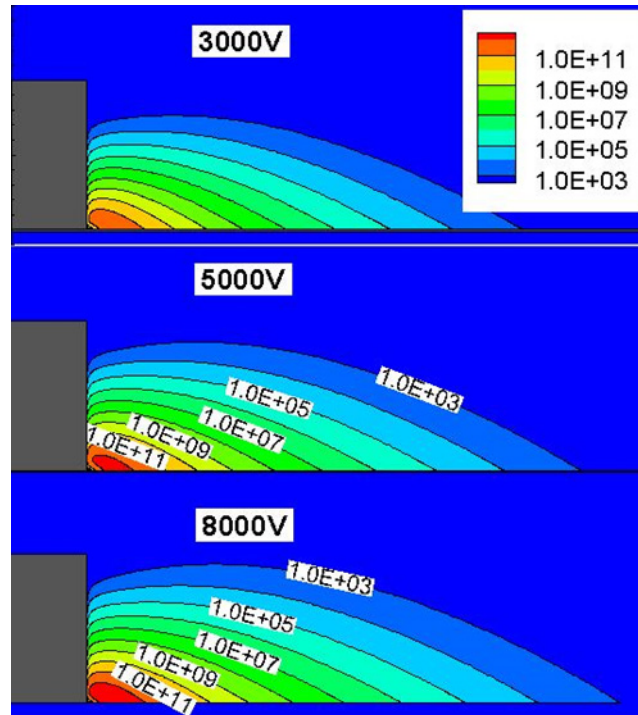


Figure 15 Discharge Domains of DBD by Different Applied EMFs

Figure 16 summarizes the effects of the gap distances between the exposed electrode and the encapsulated electrode. The figure shows the charge density and electric field potential for the gap distance of -1, 0 and 1 mm. It is found that as the distance increases and the domain of DBD decrease, and the effect is mainly caused by the changes in the electric potential field. Overlapping the two electrodes can slightly enhance the DBD effects but it does not significantly increase after overlapping the two electrodes by 1mm. These observations are identical for both the positive and negative polarities in the AC cycle and agree with experimental data [59]. In essence, the computational results based on the electrodynamics honor Paschen's law [7]. One also observes that the discharge is persistently for either the positive- or negative-going potential along the voltage-current trace after the breakdown whether in the positively or the negatively biased EMF polarities.

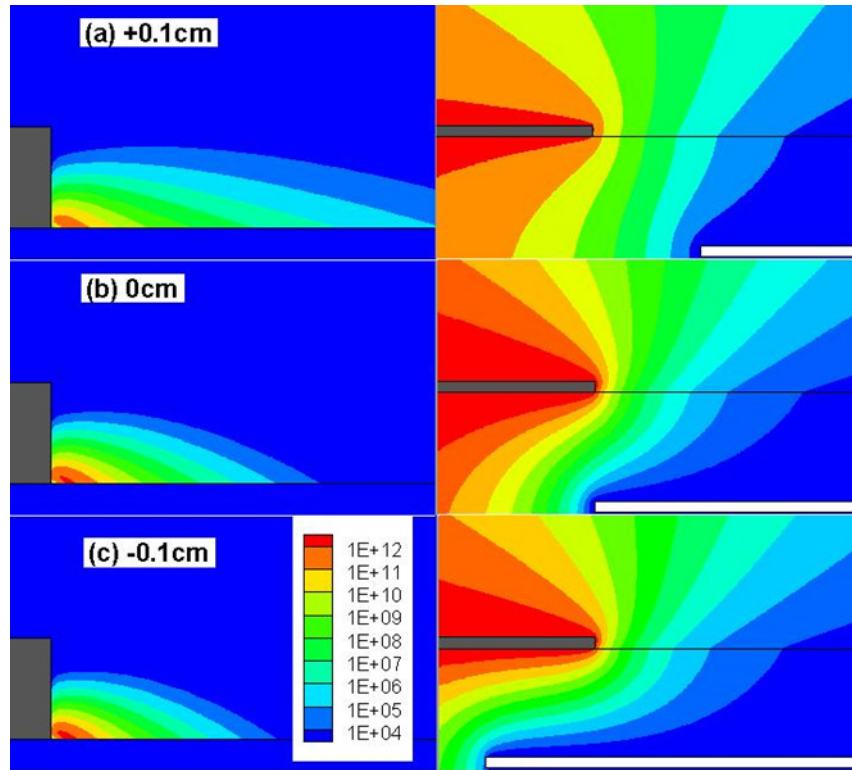


Figure 16 Effect of Gap Distances to DBD Discharge

From the experimental observations, the relative dielectric permittivity for dielectric materials has exerted measurable influence to the characteristic of discharge [3,7,8,10]. The dependence of discharge properties to the dielectric material is studied by the model equations. Calculations were performed at the external applied voltage of 4 kV for three different values of the relative electric permittivity,  $\epsilon$ ; 2.7 (polystyrene), 4.7 (glass), and 6.7 (rubber). Increasing the dielectric permittivity leads to a lower threshold of breakdown voltage and greater amount of conductive current of the discharge. The breakdown voltage drops from the value of 3.1 kV for  $\epsilon = 2.7$  to 2.7kV for  $\epsilon = 4.7$  and then to 2.6 kV for  $\epsilon = 4.7$ . As can be seen from the contour plots for the positive ion, one does not find significantly change beyond  $\epsilon = 4.7$ . The lower breakdown voltage at the higher values of the electric permittivity results in an earlier ignition and a delayed extinguishment; thus extends the discharge duration. The higher electric permittivity also produces a more compact discharge domain as shown in Figure 17.

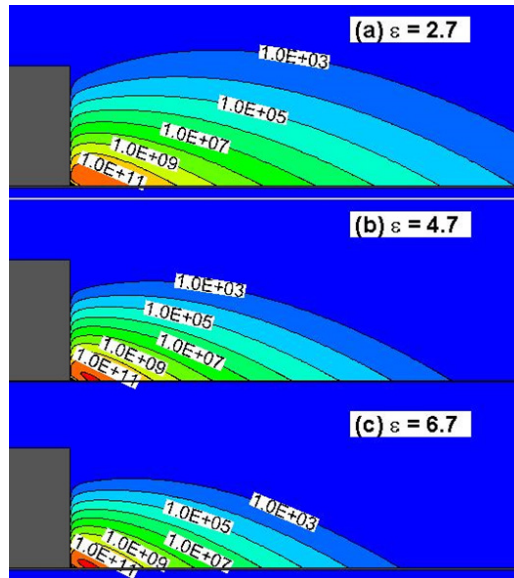


Figure 17 Effect of Permittivity on DBD Domain

The final and the most important verification of the chemical-physics ionizing model is presented by a direct comparison with a measured conductive current during the discharge. The ionization model is built on the Townsend's discharge mechanism together with the bulk and ion-ion recombination, as well as, the electron attachment and detachment. If the ionization model by the chemical-physics kinetics would not able to describe a reasonable discharge composition, the calculated conductive current of a DBD will be clearly erroneous. The experimental data is collected at an AC cycle of 5 kHz and an electrical potential of 4.0 kV [59]. In Figure 18, the calculated conductive current is designated by black line which lies within the scattering traces of the experimental data to reflect the correct magnitude and duration of the discharge. Equally important, the effects of different electrical permittivity and secondary emission coefficients on metallic electrode and dielectric surface are also accurately captured.

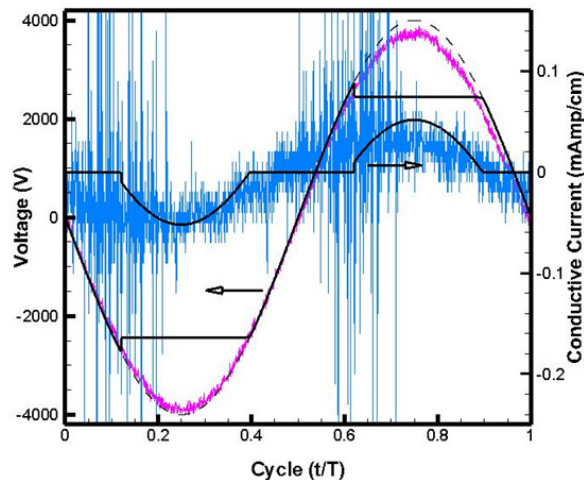


Figure 18 Comparison of Electrical Conductivity Current with Experimental Measurement,  $\phi=4$  kV,  $\omega=10$  kHz

## 2.11 Periodic Electrostatic Force of DBD

The most important phenomenon of the DBD for flow control is the periodic electrostatic force during discharge. A range of formulations have been put forth to calculate the periodic force by Corke et al. [1], Boeuf et al. [38-40], Likanskii et al. [42], Shang et al. [44-46], Singh [47], and Jayaraman et al. [60]. However, the dominant mechanism is the electrostatic force for the aerodynamics-electromagnetics interaction [6];

$$\vec{F} = \rho_e \vec{E} \quad (2-51)$$

From the charge number density of the separated free-space charges, the period force can be calculated as:

$$\vec{F} = e(n_e + n_- - n_+) \nabla \varphi \quad (2-52)$$

In the above equation, the electrostatic force vanishes either in the charge-neutral farfield or when the gradient of an applied electrical field ceased. The maximum instantaneous magnitude of the force based in the normal operational range of DBD is calculated on the order of  $10^4$  dyne/cm<sup>3</sup> at an EMF of 4 kV which have a wide range of variations among all computational simulations [38-40, 44-46]. However, the space-time averaged values of the electrostatic force yield a value range from 0 to 340 dyne/cm<sup>3</sup> in the positive push region to agree well with the estimates by Beouf et al. [38,39], in which have a recorded range of values from 10 to 100 dyne/cm<sup>3</sup>. In their work, even an instantaneous peak value up to  $10^8$  dyne/cm<sup>3</sup> has been estimated. The calculated force has also been documented in the physical unit per electrode length for two-dimensional computational simulation, and has a value up to 24.4 dyne/cm [40]. This numerical result is in general agreement with experimental data from 1.0 to 25 dyne/cm by Hoskinson et al. [61,62]. However in their experiences, the exposed electrode is constructed by cylinders of varying diameters.

The orientation of the force is completely determined by the gradient vector of the electric field potential and the sign of the net balance of charged particles, Equations (2-51) and (2-52). In the two dimensional formulation, the force components in the x and y coordinates becomes;

$$\begin{aligned} F_x &= e(n_e + n_- - n_+) \frac{\partial \varphi}{\partial x} \\ F_y &= e(n_e + n_- - n_+) \frac{\partial \varphi}{\partial y} \end{aligned} \quad (2-53)$$

From the above equation, the orientation and magnitude of the resultant periodic electrostatic force can be unambiguously determined. The uncertainty can only be challenged by the physical fidelity of the ionization process and the transport properties of the charged gas mixture. The shortfall in basic knowledge of the chemical kinetics and quantum chemical-physical kinetics is the stumbling block for all computational simulations [37-47].

The Equation (2-53) shows that the force vector must follow the direction of the electric field vector; it is useful to study how the electric field intensity is modified by the separated free-space charges, i.e. the net balance of the charged number density. If one neglects the effects of the charged density and normalized the electric potential field by the instantaneous potential of the exposed electrode, the solution is dictated by the externally applied AC field, as shown by the subset (a) in Figure 19. The contour and vector plot in the subset (a-1) are the dimensionless

electric potential  $\phi$ , and electric field  $\vec{E}$  respectively, and contours of the magnitude of the electric field, are displayed in the subset (a-2). The subsets (b) and (c) in Figure 19 show the same dimensionless quantities when the EMF of a 5 kHz AC cycles are in its maximum and minimum peaks of 8.0 kV. As can be seen from the figure, the separated charge number density in this case is too small to affect the solution. The instantaneous force field is acting along a fixed externally applied electric field potential and alters direction when the polarity on the exposed electrode changes sign.

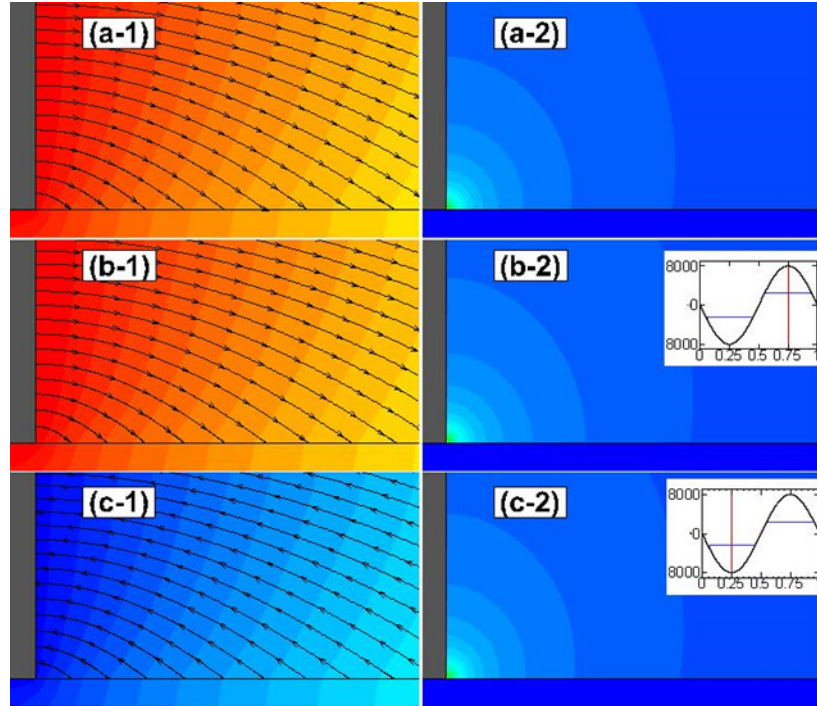


Figure 19. Comparison of Dimensionless Electric Potential  
Electric field and its magnitude for (a) no changed density, (b) maximum potential and (c) minimum potential.

Attention is now focused on the separated charged density term in the RHS of Equation (1-53). In here, the discussion is limited to the  $n_e - n_+$  model. A more complete discussion including  $n_-$  will be elaborated later but the conclusion is identical. Figure 20 depicts the comparison of number density of the positively charged ion and electrons in the peak positive and negative AC cycle. In the positive cycle, the exposed electrode is the anode, shown in subsets (a-1) to (c-1); the positively charged ions are repelled by the exposed electrode and are attached to the dielectric surface. The positively charged ions propagate along the electric field lines and are accumulated on the dielectric surface. The distributions of positively charged ion density (red color) and electron density (black color) are also inserted in the subset (b-1). The magnitude of positively charged ion density is always two orders of magnitude greater than that of the electron number density at the peak AC cycle. This indicates that the separated charge number density, and hence the force, is dominated by the positively charged ion number density. In subset (c-1), the force vector follows the electric field intensity line and its magnitude indicated by the contour that resembles the shape of the positively charged ion density contour. Similar observation can be made in the peak negatively biased AC cycle, as shown in subset (c-1) to (c-2).



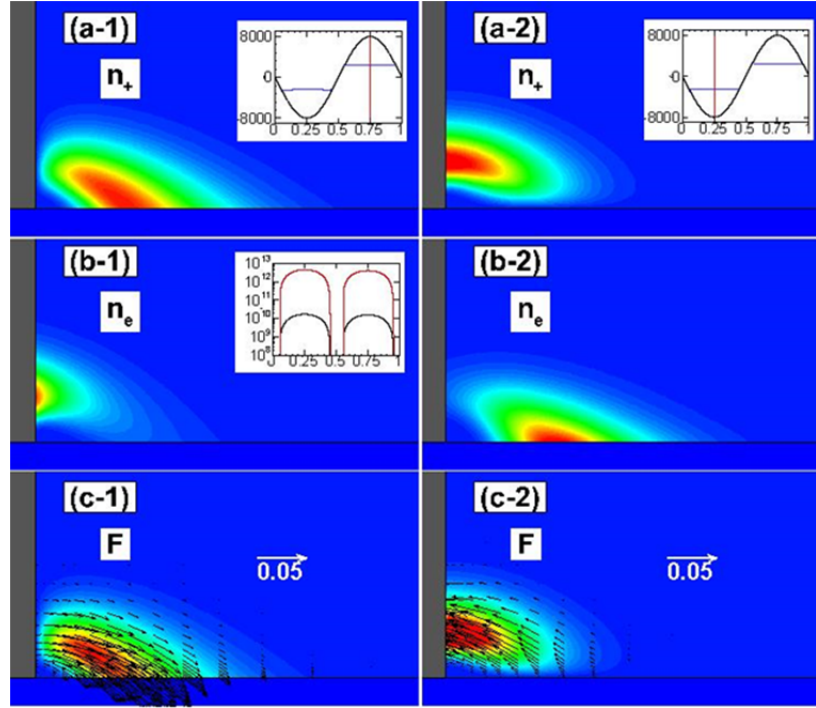


Figure 20. Comparison of (a) Positive Ion Density, (b) Electron Density, and (c) Force Field  
The insert in (b-1) shows the maximum value for the positive ion density (red) and electron density (black).

The global structure of the electric field intensity is easily understood because when the exposed electrode is anode, the electric field intensity decreases toward the dielectrics; thus, the electric field intensity is positive over the dielectrics ( $\vec{E} = -\nabla\phi, \vec{E} > 0$ ). The electric field vector over the dielectric must synchronize with the changing AC polarity, and becomes negative ( $\vec{E} < 0$ ) when polarity reversed. Therefore, the relative number densities of electrons, positively and negatively ions ultimately determine the orientation of the force. This observation has been verified over the entire range of the externally applied electrical potential examined, at different gap distances between electrodes, and variations of electrical permittivity of dielectrics [43-46]. Therefore, the orientation of the instantaneous and the time-averaged periodic electrostatic forces is no more complex than just the push-pull or pull-push combination. It solely depends on the net balance of the positively and negatively charged number density and the local electric field intensity.

Another interesting issue is the effect of the negatively charged ions to the periodic electrostatic force. To address this question, one needs to examine the generation and depletion processes of the negatively charged ions. The theory of nonequilibrium chemical kinetics indicates the key mechanisms are the electron attachment, detachment, and ion-ion recombination. From most detailed analyses [13-15], the number density of the negatively charged ion of DBD is much lower in comparison with the positively charged counterpart – generally appears as a fraction of a few percent. Again all computational simulation within the EMF ranging from 3.0 to 8.0 kV, the number densities of the negatively charged ions are nearly two orders of magnitude lower than the positively charged counterpart; the typical values are around  $n_{+,max} \sim O(10^{12} cm^{-3})$  and  $n_{-,max} \sim O(10^{10} cm^{-3})$ . These values agree very well with the most elaborated calculations from the chemical kinetic models by Bogdanov et al. [13].

In Figure 21, this quantified difference in charged particle number densities difference has been further confirmed by the electrical current-voltage curve during an AC cycle of 5 kHz and driven by an EMF of 8 kV. The computational results by the two- and three-component ionization models are indiscernible. To demonstrate the maximum possible effects of negative ion, the solution with  $k_d = 10^{-14}$  is depicted. The electrical field intensity shows an identical breakdown voltage of 2.9 kV. During the discharge phase for both the three- and two-species ionization models indicate the same constant voltage, 2.4 kV, the more sensitive conductive current also shows identical behavior for the two ionization models, which means the negatively charged ions contribute little to the discharge current.

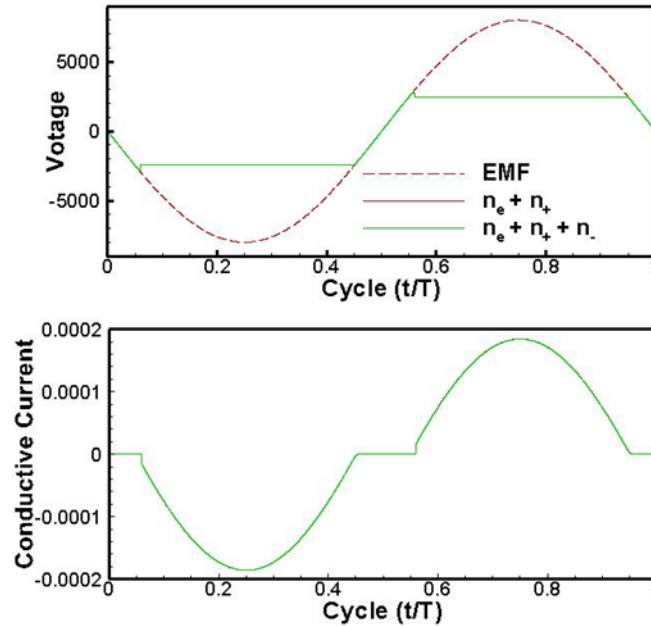


Figure 21. Electric Current Voltage Patterns of the Two-charged-species ( $n_e$ ,  $n_+$ ) and Three-charged-species ( $n_e$ ,  $n_-$ ,  $n_+$ ) Ionization Model, EMF=8.0 kV,  $f=5.0$  kHz

Figure 22 displays the comparison between the two- and three-species ionization models at the instance the electric potential over the exposed electrode is positive and reaches its maximum value. The data are depicted in a composite presentation for the electric field intensity vector  $E$ , the net balance of different number density of charged particles ( $n_e - n_-$ ), and ( $n_+ - n_- - n_e$ ), as well as, the instantaneous electrostatic force vector at an applied EMF of 8.0 kV across the overlapping electrodes. First of all, the discharge patterns are unaltered; all the electric field intensity vectors point along the electric field line, shown in (a-1) and (b-1). The instantaneous and maximum value of ( $n_+ - n_e$ ) over the dielectric barrier attains a value of  $3.96 \times 10^{12} \text{ cm}^{-3}$ . On the other hand, the ( $n_+ - n_e - n_-$ ) indicated a value of  $3.97 \times 10^{12} \text{ cm}^{-3}$  which reflects a relatively insignificant negatively charge ion number density. The resultant force according to equation (8-3) is uniformly directed from the exposed electrode to the dielectric barrier and has an instantaneous maximum magnitude of  $2.133 \times 10^5 \text{ dyne/cm}^3$ . The numerical result is nearly identical to the previous result of  $2.200 \times 10^5 \text{ dyne/cm}^3$  by a two species charged modeling [45]. This result is greater than the maximum force of  $4.10 \times 10^4 \text{ dyne/cm}^3$  generated by the EMF at 4 kV, and of  $1.500 \times 10^5 \text{ dyne/cm}^3$  by the EMF of 6.0 kV [31,45]. However, it needs to be



reminded that the maximum electrodynamics force only exists within the thin plasma sheath and for a very short period during the discharge.

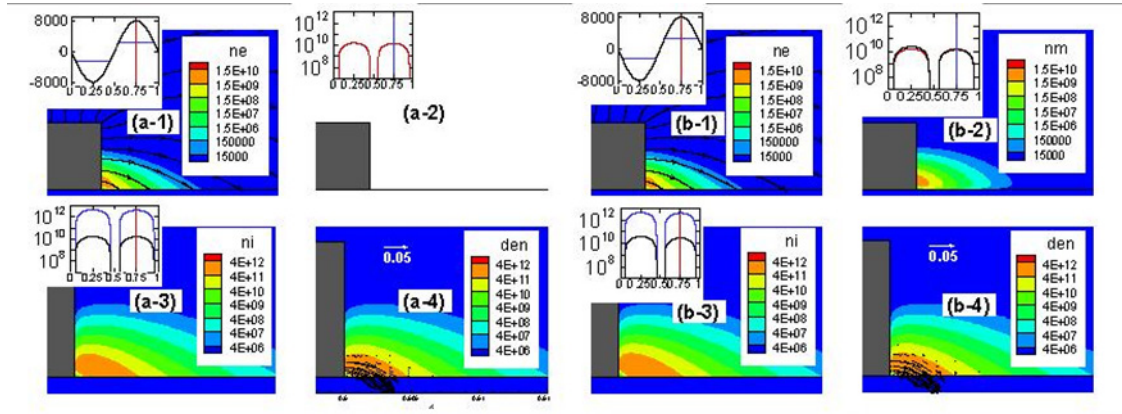


Figure 22. Comparison of Two- and Three-species Ionization Models of DBD at the Peak Positive Cycle (a) two-species model and (b) three-species model. Subset 1 is the electrical field lines and contour is the electron; subset 2 is the negative ion density contour. The insert in subset 2 is the comparison of the maximum values of electron density (red) and negative ion density (black); subset 3 is the positive ion density contour. The insert in subset 2 is the comparison of the maximum values of positive ions (blue) and the sum of electron and negative ion densities (black); subset 4 contain the Electrodynamics force vectors and charge density contour.  $V=8.0$  kV,  $f=5.0$  kHz

Figure 23 displays the electric potential and charged particle number density distributions for the instantaneous DBD field when the exposed electrode is acted as the cathode. All ions are repulsed from the dielectric surface and clustered around the lower corner of the exposed electrode. At the same instant, a large number of faster moving electrons are propagating further over the dielectric barrier away from the corner region of the electrodes. The sign of electric field intensity is now negative; pointed from the dielectric barrier toward the exposed electrode. According to the present computation, the plasma sheath is extremely thin (less than 0.002 mm) and its thickness decreases with a lower value of the electron secondary emission coefficient. The maximum value of charge separation,  $(n_+ - n_e)$  near the intersection of electrodes is  $4.4018 \times 10^{12} \text{ cm}^{-3}$ , the corresponding net number density of charged separation of the three-species model  $(n_+ - n_- - n_e)$  is  $4.4059 \times 10^{12}$ . As a consequence, the forces generated by the two models are very also very close,  $1.0012 \times 10^3 \text{ dyne/cm}^3$  and  $9.9879 \times 10^4 \text{ dyne/cm}^3$  for the three and two species models, respectively. At this instance of the AC cycle, the peak instantaneous electrostatic force is greater than when the electrical potential on the exposed electrode is positively biased but the maximum force occurs on the surface of the exposed electrode.

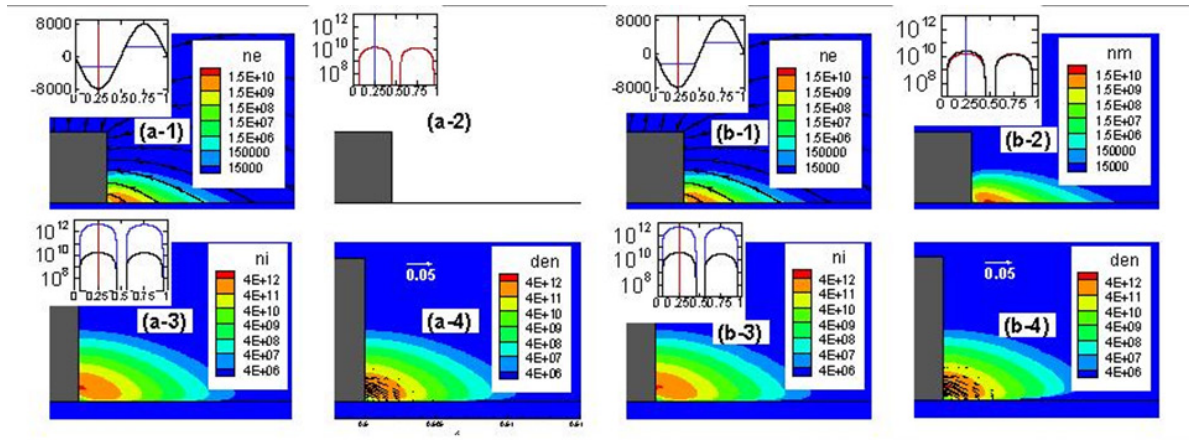


Figure 23 Comparison of Two- and Three-species Ionization Models of DBD at the Peak Negative Cycle (a) two-species model and (b) three-species model. Subset 1 is the electrical field lines and contour is the electron; subset 2 is the negative ion density contour. The insert in subset 2 is the comparison of the maximum values of electron density (red) and negative ion density (black); subset 3 is the positive ion density contour. The insert in subset 2 is the comparison of the maximum values of positive ions (blue) and the sum of electron and negative ion densities (black); subset 4 contain the Electrodynamics force vectors and charge density contour.  $V=8.0$  kV,  $f=5.0$  kHz

When the exposed metallic electrode acts as the cathode, the periodic electrostatic force is oriented from the dielectrics toward the exposed electrode. The magnitude of this force is generated by a sufficiently high electrical intensity and charged particles number density within the intersection of electrodes. This magnitude of the electrodynamics force is not negligible, but it is constrained by the solid surface of electrodes to become ineffective for momentum transfer with the neutral species. Unfortunately, all the key elements are exclusively dependent on the chemical and chemical-physical kinetics processes that are not fully understood to become the key inaccurate contributor to DBD computational simulations at the present.

The time-averaged periodic electrostatic forces by the two- and three-charged species ionization models over an AC cycle and the entire discharge domain is depicted in Figure 24. The overall force structure is indistinguishable from the two ionization models due to the effect of the number density of negative ions is not significant as compared to that of the positive ion. In short, by considering the presence of the negatively charged ions with a chemical-physics kinetics model, the averaged force that produces the well-known electric wind is less than without it, but is also insignificant. However, it must be emphasized that the precise quantification still uncertainty must be accepted as the state-of-the-art for DBD simulations.

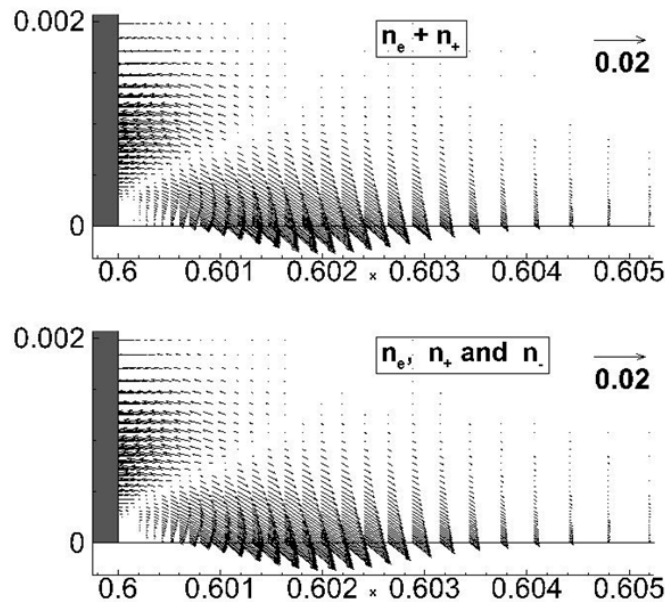


Figure 24 Time-averaged Electromagnetic Force of DBD over a Completely AC Cycle, EMF=8.0 kV,  $f=5.0$  kHz

There are two distinct regions in the direction of the time-averaged forces separated by a null-value line cutting diagonally across the corner from the exposed electrode and the dielectric wall. The region below the line of demarcation is the positive force creating a mean pushed motion along the downstream direction. The region above the cutting line has the negative force and its maximum force is exerting toward the vertical surface of the exposed electrode.

## 2.12 Concluding Remarks

The drift-diffusion model for plasma flow control is a viable approximation for the transport properties of low-temperature partially ionized gas by electron collisions. All ionizing phenomena are occurred across the molecular/atomic scales and beyond the scope of gas kinetics theory; thus must be modeled either by chemical-physics kinetics or nonequilibrium chemical kinetics. Despite this glaring deficiency for plasma modeling and simulation, the fundamental formulation still can be used to delineate the ambiguities from both the experimental observations and computational simulations.

In DCD application, the dominant process of the Joule and electrode heating and the Joule heating is concentrated over the cathode and mostly from the inner edge of the side-by-side cathode-anode configuration. The heat released by the Joule heating is generally lower than six percent of the power input for DCD generation.

The multiple microdischarges within the DBD domain are unsupportable by current computational capability. As the consequence, the different DBD mechanisms during an AC cycle are unable to be duplicated precisely by the drift-diffusion and chemical-physics models. However, the periodic electrostatic force in different phases of the AC cycle still can be described by the polarities of the exposed electrode with the grounded and encapsulated electrode.

The confusion issue on the orientation of the periodic force can be clarified by the net balance of the number density of electrons, the negatively and positively charged ions. The instantaneous periodic electrostatic force is no more complex than by a simple push-pull or push-push description. The maximum time-averaged force has a lower magnitude than the instantaneous counterpart. According to the chemical-physics ionization models, the negatively charged ion contributes very little to the global DBD performance.

A sustained basic research is urgently needed for future advance of nonequilibrium chemical reaction and quantum chemical-physical kinetics at full spectrum of thermal conditions.

## 3 Modeling Fuel Cells

### 3.1 Introduction

In order to investigate SOFCs mathematically, efforts have been put into development of models including mass transportation and electrochemical reactions. Zhu et al. [63] presents a new computational modeling framework for SOFC simulation that takes the whole system including flow channels and planar membrane-electrode assemblies into consideration. His work employed multistep reaction mechanisms in terms of detailed elementary heterogeneous chemical kinetics. Detailed charge transfer reactions are analyzed by separating the mechanism into several elementary steps. Greene et al. [64] focuses on minimizing the concentration overpotential by applying functionally graded electrodes and observes the physical phenomenon of mass transfer throughout the electrodes for multi-gas inputs. However, the activation overpotential in both of their models is directly calculated by the Butler-Volmer equation and do not take the micro structural characteristics into consideration. Theoretically, these micro structural factors are critical to the size of active reaction surface sites and hence affect the rate of electrochemical reaction. M. Ni et al. [65] developed the model from a micro-scale level and the model was able to capture the coupled electrochemical reactions and mass transfer involved in SOFC operation. But all the micro structural parameters are treated separately. Although physically all those parameters are observed to correlate with each other. Once one parameter changes, the rest of the parameters should alter correspondingly. This work expands upon previously developed theories and models [66,67]. The model takes into account electronic, ionic, and gas transport together with electrochemical reaction effects. It can predict the distribution of overpotentials, current densities, and gas concentrations along the electrode. Also, the model takes into account all the microstructural factors that are critical to cell performance. In addition, the model applied the binary random packed sphere model to mimic the microstructural make-up the electrodes [68,69]. However, to the best knowledge, the literatures lack exploring the correlation of microstructural parameters, which is crucial to resemble a real-world cell performance.

The primary focus of our study is to investigate how the microstructural parameters are related to each other and how they affect cell performance. Several studies associated with tortuosity and porosity relations were developed and organized by Matyka et al. [71]. For a spherical particle mixture, Currie [70] proposed that porosity is inversely proportional to tortuosity. This assumption was confirmed by experimental data. Ricardo Dias et al. [71] extended this study and investigated the adjustable parameter,  $n$ , which is crucial to determining the porosity-tortuosity correlation (see equation 31). German [73] summarized that porosity is dependent on the relative composition of two species and the particle size ratio in a binary mixture of spherical particles. The larger the particle size ratio is (i.e. the larger the difference between the sizes of the two particles), the higher the packing density at all compositions will be. Ricardo Dias et al. [74] explored the dependence of packing porosity on particle size ratio, focusing on exploring the significance of particle size ratio.

### 3.2 Numerical Model

#### 3.2.1 Anode

##### 3.2.1.1 Overpotential due to electrochemical reactions and ohmic resistance

The overall charge balance relationship can be written as:

$$\frac{dJ_{e,a}}{dx} = -\frac{dJ_{i,a}}{dx} = -S_v J_{n,a} \quad (3-1)$$

Where  $J_{e,a}$  and  $J_{i,a}$  are the current density ( $\text{A/m}^2$ ) due to transport of electronic and ionic conductors in the anode;  $S_v$  is active surface area per unit volume ( $\text{m}^2/\text{m}^3$ ) of the porous electrode;  $J_{n,a}$  is the transfer current density per unit area of reaction surface ( $\text{A/m}^2$ ). This equation accounts for the electrochemical reaction rate for the fuel cell along the anode.

The active surface area per unit volume indicates the available reactions sites that can be used for electrochemical reactions and was developed by Costamagna et al. [69] from binary random packing and percolation theories. It is represented below:

$$S_v = \pi \sin^2 \theta r_e^2 n_t n_i n_e \frac{Z_e Z_i}{6} P_i P_e \quad (3-2)$$

where  $\theta$  is the contact angle between electronic and ionic conducting particles;  $r_e$  is the radius of electronic conducting particles;  $n_t$  is the total number of particles per unit volume;  $n_i$  and  $n_e$  are the number fraction of ionic and electronic conducting particles, respectively;  $Z_i$  and  $Z_e$  are the coordination number of ionic and electronic conducting particles, respectively;  $P_i$  and  $P_e$  are the probability that a given ionic or electronic conducting particle, respectively, belongs to a percolation cluster. Essentially,  $S_v$  can be expressed as a function of porosity, electronic particle size, number fraction, and particle size ratio [69].

The transfer current density is normally described by the general form of the Butler-Volmer (B-V) equation.

$$J_{n,a} = J_{0,a} \left\{ \frac{y_{H_2}}{y_{H_2}'} \exp\left(\frac{\beta z F \eta_a}{RT}\right) - \frac{1 - y_{H_2}}{1 - y_{H_2}'} \exp\left(-\frac{(1 - \beta) z F \eta_a}{RT}\right) \right\} \quad (3-3)$$

Where  $J_{0,a}$  is the exchange current density of the anode ( $\text{A/m}^2$ );  $y_{H_2}$  is the molar fraction of  $H_2$ .  $y_{H_2}'$  is the molar fraction of  $H_2$  at the fuel channel.  $R$  is the ideal gas constant ( $8.314 \text{ J/mol K}$ ).  $T$  is the operating temperature (K).  $\beta$  is the charge transfer coefficient and is normally chosen to be 0.5 for symmetry [75].

Applying Ohm's law for the electronic and ionic conductors, we get:

$$\frac{dV_e}{dx} = \rho_{e,a}^{eff} J_{e,a}; \frac{dV_i}{dx} = \rho_{i,a}^{eff} J_{i,a} \quad (3-4)$$

$\rho_{e,a}^{eff}$  is the effective resistivity ( $\Omega \cdot m$ ) of the anode electronic conductors;  $\rho_{i,a}^{eff}$  is the effective resistivity of anode ionic conductors;  $V_e$  and  $V_i$  are the electronic and ionic potential (V), respectively. The effective resistivity can be determined as:

$$\rho_{e,a}^{eff} = \frac{\tau}{\varphi_e(1-\varepsilon)\sigma_{e,a}}; \rho_{i,a}^{eff} = \frac{\tau}{(1-\varphi_e)(1-\varepsilon)\sigma_{i,a}} \quad (3-5)$$

Where  $\varphi_e$  is the volume fraction of electronic conductors;  $\tau$  is tortuosity of the anode;  $\varepsilon$  is porosity of the anode;  $\sigma_{e,a}$  is the electronic conductivity (S/m) of the anode electronic conductors; and  $\sigma_{i,a}$  is ionic conductivity (S/m) of the anode ionic conductors.

The anode overpotential  $\eta_a$  can be determined by the difference of equilibrium potential and practical potential.

$$\eta_a = (V_e^{eq} - V_i^{eq}) - (V_e - V_i) \quad (3-6)$$

$V_e^{eq}$  and  $V_i^{eq}$  are the equilibrium electronic and ionic potential (V), respectively, and are constant throughout the cell.

The first derivative of  $\eta_a$  can be written as:

$$\frac{d\eta_a}{dx} = -\left(\frac{dV_e}{dx} - \frac{dV_i}{dx}\right) = \rho_{i,a}^{eff} J_{i,a} - \rho_{e,a}^{eff} J_{e,a} \quad (3-7)$$

Combing the charge balance and B-V equation, the second derivative of  $\eta_a$  is equal to:

$$\begin{aligned} \frac{d^2\eta_a}{dx^2} &= \rho_{i,a}^{eff} \frac{dJ_{i,a}}{dx} - \rho_{e,a}^{eff} \frac{dJ_{e,a}}{dx} = S_v J_{n,a} (\rho_{i,a}^{eff} + \rho_{e,a}^{eff}) \\ &= S_v J_{0,a} (\rho_{i,a}^{eff} + \rho_{e,a}^{eff}) \left\{ \frac{y_{H_2}}{y_{H_2}'} \exp\left(\frac{\beta z F \eta_a}{RT}\right) - \frac{1 - y_{H_2}}{1 - y_{H_2}'} \exp\left(-\frac{(1-\beta) z F \eta_a}{RT}\right) \right\} \end{aligned} \quad (3-8)$$

### 3.2.2 Overpotential due to Mass transport

Diffusion processes within a porous electrode structure can be distinguished as two types. First, there is normal diffusion in which one gas diffuses through another, with negligible influence of the pore walls on the rate of diffusion. This applies when the mean free path of the molecules is much less than the pore diameter. Second, when the mean free path of the molecules is greater than the pore diameter, this is referred to as Knudsen diffusion. For most of SOFCs, the Knudsen effects cannot be neglected [76]. Therefore, for a binary gas system going through the pore

structure, the overall effective diffusion coefficient  $D_i^{eff}$  can be written by combining effective normal binary diffusion coefficient  $D_{i,j}^{eff}$  and the effective Knudsen diffusion coefficient  $D_{i,K}^{eff}$ . [77]

$$\frac{1}{D_i^{eff}} = \frac{1}{D_{i,j}^{eff}} + \frac{1}{D_{i,K}^{eff}} \quad (3-9)$$

The effective diffusion coefficient depends on the microstructure of the porous anode, quantified through the porosity and tortuosity values. Thus, the effective binary diffusion coefficient can be written as:

$$D_{i,j}^{eff} = \frac{\varepsilon}{\tau} D_{i,j} \quad (3-10)$$

For Knudsen diffusion, the coefficient can be described as in [63],

$$D_{i,K} = \frac{2}{3} d_0 \sqrt{\frac{8RT}{\pi M_i}} \quad (3-11)$$

where  $d_0$  is the pore diameter (m) and is assumed to be approximately equal to the hydraulic diameter. [78]

$$d_0 \approx d_h \frac{4}{A_0} \frac{\varepsilon}{1 - \varepsilon} \quad (3-12)$$

$A_0$  is the specific surface area based on the solid volume. For randomly packed binary spheres,  $A_0$  is expressed as:

$$A_0 = \frac{6}{d_e} \frac{n_e + (1 - n_e)\alpha^{-2}}{n_e + (1 - n_e)\alpha^{-3}} \quad (3-13)$$

where  $d_e$  is the diameter (m) of electrically conducting particles,  $\alpha$  is the particle size ratio of ionic to electronic conducting particles.

Similarly as with the effective binary diffusion coefficient, the effective Knudsen diffusion coefficient can be expressed as:

$$D_{i,K}^{eff} = \frac{\varepsilon}{\tau} D_{i,K} \quad (3-14)$$

The general form of the Fick's law takes into account both diffusion and convection mass transfer and can be expressed as [79]:



$$N_{H_2} = -D_{H_2}^{eff} \frac{dc_{H_2}}{dx} + c_{H_2} v \quad (3-15)$$

$$N_{H_2O} = -D_{H_2O}^{eff} \frac{dc_{H_2O}}{dx} + c_{H_2O} v \quad (3-16)$$

Where  $N_i$  is molar flux ( $\text{mol}/\text{m}^2 \cdot \text{s}$ ) of species  $i$ ;  $D_i^{eff}$  is the effective diffusion coefficient ( $\text{m}^2/\text{s}$ ) of species  $i$  (from equation 10);  $c_i$  is the concentration ( $\text{mol}/\text{m}^3$ ) of specie  $i$ ;  $v$  is the convection velocity ( $\text{m}/\text{s}$ ).

Under constant operating temperatures, the ideal gas law can be written as:

$$\frac{dp}{dx} = -\frac{dc}{dx} RT \quad (3-17)$$

If pressure is uniform throughout the electrode, then  $dp/dx$  is constant. According to eqn. (3-17),  $dc/dx$  will also be constant. Then we will have:

$$\frac{dc_{H_2}}{dx} = -\frac{dc_{H_2O}}{dx} \quad (3-18)$$

For equimolar counter-current mass transfer, we have  $N_{H_2} = -N_{H_2O}$ . Combine this condition with eqn. (3-15) and eqn. (3-16), the  $H_2$  flux can be expressed as:

$$N_{H_2} = -\left(y_{H_2O} D_{H_2}^{eff} + y_{H_2} D_{H_2O}^{eff}\right) \frac{dc_{H_2}}{dx} \quad (3-19)$$

Based on flux-current relations as well as ideal gas law, we have

$$N_{H_2} = \frac{J_{e,a}}{2F}; \frac{dc_{H_2}}{dx} = \frac{dy_{H_2}}{dx} \frac{P}{RT} \quad (3-20)$$

Eqn. (3-20) turns into:

$$\frac{dy_{H_2}}{dx} = -\frac{1}{(1 - y_{H_2}) D_{H_2}^{eff} + y_{H_2} D_{H_2O}^{eff}} \frac{RT}{P} \frac{J_{e,a}}{2F} \quad (3-21)$$

### 3.2.3 Anode governing equations and boundary conditions

Combining the equations and solving for the molar fraction of fuel, electronic current density, and overall overpotential; we get a total of three governing equations for the anode.

$$\frac{d^2\eta_a}{dx^2} = S_v J_{0,a} (\rho_{i,a}^{eff} + \rho_{e,a}^{eff}) \left\{ \frac{y_{H_2}}{y_{H_2}^I} \exp\left(\frac{\beta z F \eta_a}{RT}\right) - \frac{1-y_{H_2}}{1-y_{H_2}^I} \exp\left(-\frac{(1-\beta)zF\eta_a}{RT}\right) \right\}$$

$$\frac{dJ_{e,a}}{dx} = -S_v J_{0,a} \left\{ \frac{y_{H_2}}{y_{H_2}^I} \exp\left(\frac{\beta z F \eta_a}{RT}\right) - \frac{1-y_{H_2}}{1-y_{H_2}^I} \exp\left(-\frac{(1-\beta)zF\eta_a}{RT}\right) \right\}$$

$$\frac{dy_{H_2}}{dx} = -\frac{1}{(1-y_{H_2})D_{H_2}^{eff} + y_{H_2}D_{H_2O}^{eff}} \frac{RT}{P} \frac{J_{e,a}}{2F}$$

The computational domain is shown in Figure 25. The boundary conditions for the governing equations can be derived as follows: at the fuel gas inlet, which is also the location of the current collector, the hydrogen molar fraction is equal to the bulk flow value. The total current density only comes from the transport of electrons. As a result, the boundary conditions can be expressed as:

$$\begin{aligned} y_{H_2}|_{inlet} &= y_{H_2}(bulk) \\ J_{i,a}|_{inlet} &= 0 \\ J_{e,a}|_{inlet} &= J_{total} \\ \frac{d\eta_a}{dx}|_{inlet} &= \rho_{i,a}^{eff} J_{i,a} - \rho_{e,a}^{eff} J_{e,a} = -\rho_{e,a}^{eff} J_{total} \end{aligned}$$

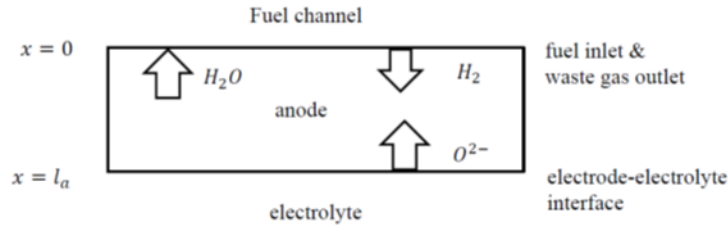


Figure 25 Anode Computational Domain

At the electrode-electrolyte (EE) interface, the transport of ions is the only factor that contributes to the overall current density. Therefore, ion current density equals to the overall current density. This defines the boundary condition of the overpotential at the EE interface.

$$\begin{aligned} J_{i,a}|_{EE} &= J_{total} \\ \frac{d\eta_a}{dx}|_{EE} &= \rho_{i,a}^{eff} J_{i,a} - \rho_{e,a}^{eff} J_{e,a} = \rho_{i,a}^{eff} J_{total} \end{aligned}$$

After solving the three coupled governing equations,  $\eta_a$ ,  $J_{e,a}$  and  $y_{H_2}$  distributions can be obtained. Now the overall overpotential of the anode can be written as follows:

$$\eta_a|_{overall} = (V_e^{eq} - V_i^{eq}) - (V_e|_{inlet} - V_i|_{EE}) = \eta_a|_{inlet} + \eta_a|_{EE} \quad (3-22)$$

### 3.3 Cathode

#### 3.3.1 Overpotential due to electrochemical reactions and ohmic resistance

The electrochemical reaction equations in the cathode are similar to the ones in the anode and can be derived in a similar fashion, to produce the following:

$$\frac{d^2\eta_c}{dx^2} = S_v J_{0,c} (\rho_{i,c}^{eff} + \rho_{e,c}^{eff}) \left\{ \frac{y_{O_2}}{y_{O_2}'} \exp\left(\frac{\beta z F \eta_c}{RT}\right) - \exp\left(-\frac{(1-\beta) z F \eta_c}{RT}\right) \right\} \quad (3-23)$$

$$\frac{dJ_{e,c}}{dx} = -S_v J_{0,c} \left\{ \frac{y_{O_2}}{y_{O_2}'} \exp\left(\frac{\beta z F \eta_c}{RT}\right) - \exp\left(-\frac{(1-\beta) z F \eta_c}{RT}\right) \right\} \quad (3-24)$$

where  $\eta_c$  is the cathode overpotential,  $J_{0,c}$  is the cathode exchange current density,  $\rho_{e,c}^{eff}$  is the effective resistivity of cathode electrically conducting particles, and  $J_{e,c}$  is the electronic current density.

#### 3.3.2 Overpotential due to mass transport

Following the derivation in Berger [80], an effective Knudsen diffusion coefficient of  $O_2$  can be defined as:

$$N_{O_2} = -D_{O_2,K}^{eff} \left( \frac{dc_{O_2}}{dx} \right)_{Knudsen} \quad (3-25)$$

The effective normal diffusion of oxygen taking both conduction and convection transport can be defined by

$$N_{O_2} = -D_{O_2,N_2}^{eff} \left( \frac{dc_{O_2}}{dx} \right)_{normal} + c_{O_2} v = -D_{O_2,N_2}^{eff} \left( \frac{dc_{O_2}}{dx} \right)_{normal} + c_{O_2} \frac{N_{total}}{c_{total}} \quad (3-26)$$

Total concentration of  $O_2$  is equal to the summation of Knudsen concentration and normal concentration.

$$\frac{dc_{O_2}}{dx} = \left( \frac{dc_{O_2}}{dx} \right)_{Knudsen} + \left( \frac{dc_{O_2}}{dx} \right)_{normal} = - \left( \frac{1}{D_{O_2,K}^{eff}} + \frac{1}{D_{O_2,N_2}^{eff}} \right) N_{O_2} + \frac{c_{O_2}}{c_{total}} \frac{1}{D_{O_2,N_2}^{eff}} N_{total} \quad (3-27)$$

On the cathode side, nitrogen does not involve any electrochemical reaction, so flux of nitrogen at steady state is zero. Then we have  $N_{total} = N_{O_2}$ . The  $O_2$  flux turns into

$$N_{O_2} = - \left( \frac{1}{D_{O_2,K}^{eff}} + \frac{1-y_{O_2}}{D_{O_2,N_2}^{eff}} \right)^{-1} \frac{dc_{O_2}}{dx} \quad (3-28)$$

By combining flux-current relations and the ideal gas law, Eqn. (2-28) becomes:

$$\frac{dy_{O_2}}{dx} = - \frac{RT}{P} \left( \frac{1}{D_{O_2,K}^{eff}} + \frac{1-y_{O_2}}{D_{O_2,N_2}^{eff}} \right) \frac{J_{e,c}}{4F} \quad (3-29)$$

### 3.3.3 Cathode governing equations and boundary conditions

Similar to the anode, three coupled governing equations for the cathode can be defined.

$$\begin{aligned} \frac{d^2 \eta_c}{dx^2} &= S_v J_{0,c} \left( \rho_{i,c}^{eff} + \rho_{e,c}^{eff} \right) \left\{ \frac{y_{O_2}}{y_{O_2}'} \exp \left( \frac{\beta z F \eta_c}{RT} \right) - \exp \left( - \frac{(1-\beta) z F \eta_c}{RT} \right) \right\} \\ \frac{dJ_{e,c}}{dx} &= -S_v J_{0,c} \left\{ \frac{y_{O_2}}{y_{O_2}'} \exp \left( \frac{\beta z F \eta_c}{RT} \right) - \exp \left( - \frac{(1-\beta) z F \eta_c}{RT} \right) \right\} \\ \frac{dy_{O_2}}{dx} &= - \frac{RT}{P} \frac{1-y_{O_2}}{D_{O_2}^{eff}} \frac{J_{e,c}}{4F} \end{aligned}$$

The boundary conditions in the cathode can also be obtained using the same approach used with the anode.

$$\begin{aligned} y_{O_2} \Big|_{inlet} &= y_{O_2(bulk)} \\ J_{i,c} \Big|_{inlet} &= 0 \\ J_{e,c} \Big|_{inlet} &= J_{total} \\ \frac{d\eta_c}{dx} \Big|_{inlet} &= \rho_{i,c}^{eff} J_{i,c} - \rho_{e,c}^{eff} J_{e,c} = -\rho_{e,c}^{eff} J_{total} \\ J_{i,c} \Big|_{EE} &= J_{total} \\ \frac{d\eta_c}{dx} \Big|_{EE} &= \rho_{i,c}^{eff} J_{i,c} - \rho_{e,c}^{eff} J_{e,c} = \rho_{i,c}^{eff} J_{total} \end{aligned}$$

After solving the governing equations, the cathode overall overpotential can be calculated as:

$$\eta_c \Big|_{overall} = (V_e^{eq} - V_i^{eq}) - (V_e \Big|_{inlet} - V_i \Big|_{EE}) = \eta_c \Big|_{inlet} + \eta_c \Big|_{EE} \quad (3-30)$$

### 3.4 Analysis of Microstructure Parameters Correlations and Percolation Threshold

#### 3.4.1 Relationship between porosity and tortuosity

Figure 26 plots the data from the experiments of Currie [70] for mixtures of spherical particles. The tortuosity ( $\tau$ ) is assumed to be inversely proportional to porosity ( $\epsilon$ ). By applying eqn. (2-31) as the relationship, it can be observed from Figure 26 that most of the data falls in the region where the  $n$  value is between 0.4 and 0.5.

$$\tau = \frac{1}{\epsilon^n} \quad (3-31)$$

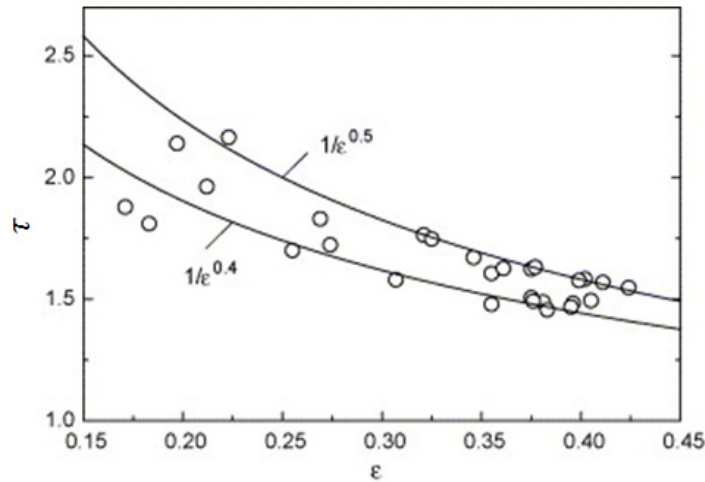


Figure 26 Dependence of Tortuosity on the Packing Porosity

In order to further investigate the adjustable parameter  $n$ , Ricardo [71] performed an experimental study of binary mixtures of spherical particles, as shown in Figure 27. In this figure,  $\phi_L$  represents volume fraction of large particles. It can be observed that for particle size ratios that are less or equal to 3.33, the value of  $n$  is approximately 0.5 regardless of the volume fraction. For most SOFCs, the sizes of ionic and electronic conductors are comparable, so it is reasonable to choose a value of  $n$  to be equal to 0.5 in the numerical model. However, if we happen to encounter a large particle size ratio, the plot in Figure 27 will be used for selecting the appropriate  $n$  value.

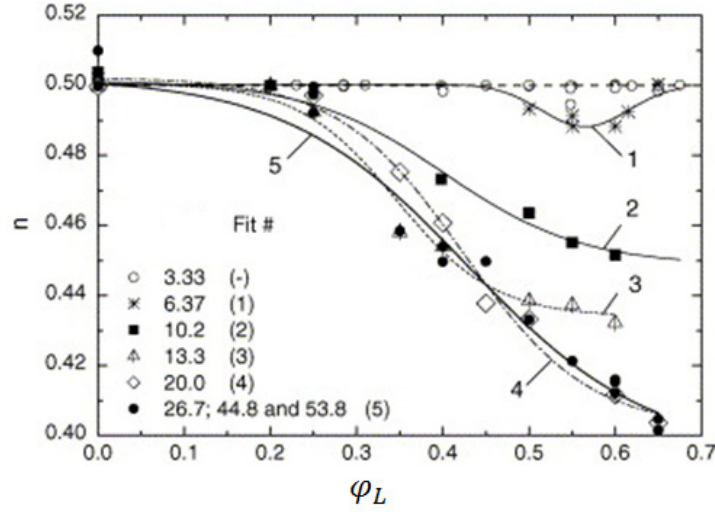


Figure 27 Dependence of  $n$  on  $\phi_L$  for Different Particle Size Ratios

### 3.4.2 Relationship between porosity and particle size

For common SOFCs the particle sizes of electronic and ionic conductors will be close, and hence the ratio will be close to 1. S. Yerazunis et al. [80] performed experiments to analyze the binary spherical mixtures with comparable particles sizes as shown in Figure 28. The particles were densely-packed to ensure good connection of particles, as in most electrode configurations of SOFCs. Based on the experimental data, porosity can be expressed as a function of particle size ratio and volume fraction as shown in eqn. 39.

$$1 - \varepsilon = \frac{0.64}{1 - \left( 0.362 - 0.315 \left( \frac{D_s}{D_L} \right)^{0.7} \right) \phi_L + 0.955 \left( \frac{D_s}{D_L} \right)^4 \left( \frac{\phi_L^2}{1 - \phi_L} \right)} \quad (3-32)$$

Where  $\phi$  is volume fraction and the subscript L and S indicates the larger particle size and smaller particle size, respectively. It can be deduced from the experimental data that the porosity value approaches 0.36 as the particle size ratio approaches 1. Therefore, we assume that when ionic particle size is equal to electronic particle size, the porosity is set to be 0.36. It is noted that in this particular circumstance bimodal mixtures can be expressed as monomodal.

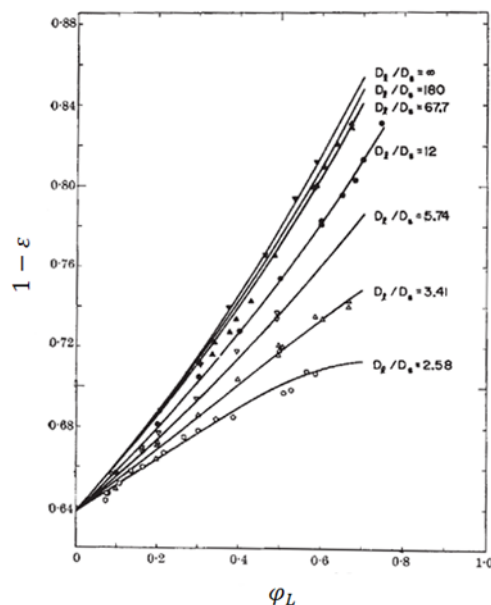


Figure 28 Packing Density vs. Composition for Different Particle Size Ratios

### 3.5 Percolation Threshold

In this model, the electrode was assumed to be represented as a collection of randomly packed spherical particles made up of either electronically conductive or ionically conductive materials. By applying a coordination number model together with percolation theory, this model guarantees that the same type of particles (ionic or electronic conductors) contact each other and form a network or particle chain through the electrode. That is to say, for any given combination of compositions and particle size ratios of electronic and ionic conductors, the coordination model can be used to differentiate if it is above or below the percolation threshold. If above the percolation threshold, pathways are guaranteed to be formed through the electrode for the conduction of ions and electrons. If below the percolation threshold, these pathways are not guaranteed to span the entire electrode and may not provide continuous pathways for conduction. In these cases, the model assumptions are not valid.

#### 3.5.1 Model Validation

In order to determine if the correlations of microstructure parameters have the potential to accurately predict cell performance, model validation was carried out. Three experimental investigations from literature [81] [82] [83] focusing on different perspectives of SOFC performance were selected to facilitate the comparison between predicted results and experimental data.

There are two types of inputs to the model: operational inputs and physical inputs. The operational inputs of the model include: operating temperature and pressure; fuel gas composition; and current density. The physical inputs include: exchange current density; thicknesses of the anode, cathode and electrolyte; volume fraction (or mass fraction) of electronic and ionic conductors; particle size of electronic (or ionic) conductors; particle size ratio of ionic to electronic conductors; porosity; and tortuosity.

The first experimental data selected is from S.P. Jiang et al. [81]. The objective of the experiment was to investigate the effect of impregnation of different volume fractions of nano-sized YSZ particles into nickel anodes on the electrode behavior. Table 2 lists the parameters provided by the experimental study. In order to solve this problem using the developed numerical model, Ni particle size, tortuosity, and anode exchange current density needed to be determined.

Table 1  $\epsilon_i$  and  $\xi_i/k_B$  values

	<b>N<sub>2</sub></b>	<b>O<sub>2</sub></b>	<b>CH<sub>4</sub></b>	<b>H<sub>2</sub>O</b>	<b>CO</b>	<b>H<sub>2</sub></b>	<b>CO<sub>2</sub></b>
<b><math>\epsilon_i</math></b>	3.798	3.467	3.758	2.641	3.69	2.827	3.941
<b><math>\xi_i/k_B</math></b>	71.4	106.7	148.6	809.1	91.7	59.7	195.2

Table 2 Value of input parameters for model validation case No. 1

<b>Parameter (provided by paper)</b>	<b>Value</b>
Operating Temperature	1073K
Pressure	1.0 atm
Anode Thickness	30 $\mu$ m
Electrolyte Thickness	1mm
Anode Gas Composition	97% H <sub>2</sub> (3% H <sub>2</sub> O)
Volume Fraction of NiO/YSZ	Ni: 100%/0% Ni+2.7mg/cm <sup>2</sup> YSZ: 83%/17% Ni+4.0mg/cm <sup>2</sup> YSZ: 79%/21%
Porosity	30%
YSZ Particle Size	0.1-0.3 $\mu$ m

Let us take the Ni+4.0mg/cm<sup>2</sup> YSZ case, for example. The volume fraction of Ni/YSZ for Ni+4.0mg/cm<sup>2</sup> YSZ is given as 79% Ni/21% YSZ. The number fraction of the electronic conductor can be expressed as a function of particle size ratio from eqn. (3-33). The probability that one cluster that belongs to a percolation cluster can be obtained from eqn. (3-34). Then the upper and lower bounds of particle size ratio and electronic number fraction are calculated and listed in Table 3. The values within the two bounds will maintain percolation and hence ensure good conductivity.



$$\varphi_e = \frac{n_e}{(1-n_e)\alpha^3 + n_e} \quad (3-33)$$

$$P_e = \left[ 1 - \left( \frac{4 - Z_{e-e}}{2} \right)^{2.5} \right]^{0.4} \quad (3-34)$$

where

$$Z_{e-e} = \left[ \frac{6n_e}{n_e + (1-n_e)\alpha^2} \right]$$

Substituting the porosity value and the volume fraction of the electronic conductor into the porosity-particle size ratio correlation gives us a particle size ratio of  $\alpha=0.4$ . By choosing the average YSZ particle size, which is 0.2  $\mu\text{m}$ , Ni particle size can be derived as 0.5  $\mu\text{m}$ .

Table 3 Upper and lower bounds for particle size ratio and electronic volume fraction for 79% Ni/ 21% YSZ

$\varphi_e=0.79$	Lower bound	Upper bound
$\alpha$	0.13	0.53
$n_e$	0.09	0.36

Tortuosity can be obtained from the porosity-tortuosity correlation. Since the particle ratio in this case is less than 3.33, it is reasonable to set n equals to 0.5.

$$\tau = \frac{1}{\varepsilon^n} = \frac{1}{0.3^{0.5}} = 1.826$$

Exchange current density was calculated from the provided electrochemical impedance spectroscopy (EIS) data and charge transfer resistance is determined by applying the simplified B-V equation. After all the parameters applied in the model are calculated, the mathematical simulation is performed. From Figure 29, it can be seen that the numerical results and experimental data agree reasonably well with each other.

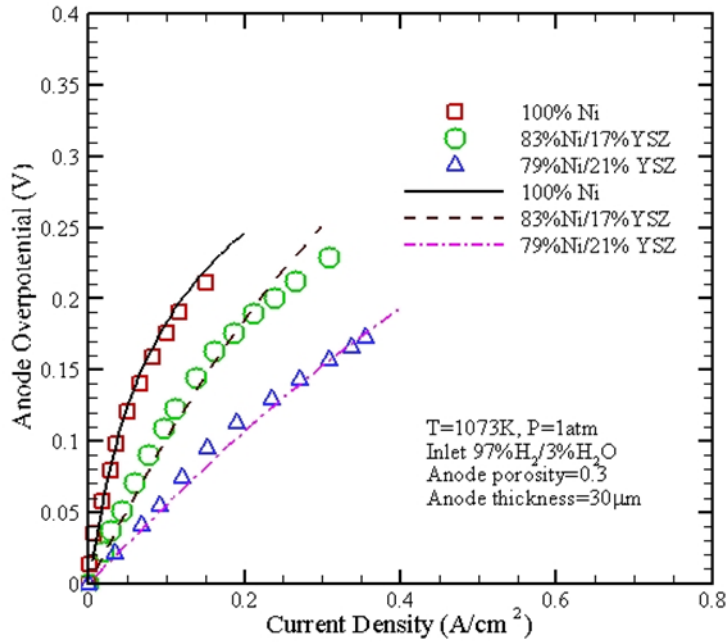


Figure 29 Comparison between Numerical Results and Experimental Data for Case No. 1

The second experiment comes from Kim et al [82]. The objective of this experiment was to investigate the performance and durability of Ni-coated YSZ anodes for intermediate temperature solid oxide fuel cells. Applying the same approach as the previous case, ionic particle size in anode, electronic particle size in cathode, and tortuosity is calculated by using the adopted sub-model correlations. The anode and cathode exchange current density are calculated by the provided EIS plot from experimental measurement. After that, the current-voltage (I-V) curve is calculated by applying the mathematical model. Again, a good consistency between numerical results and experimental data for both of the operating temperatures can be seen from Figure 30.

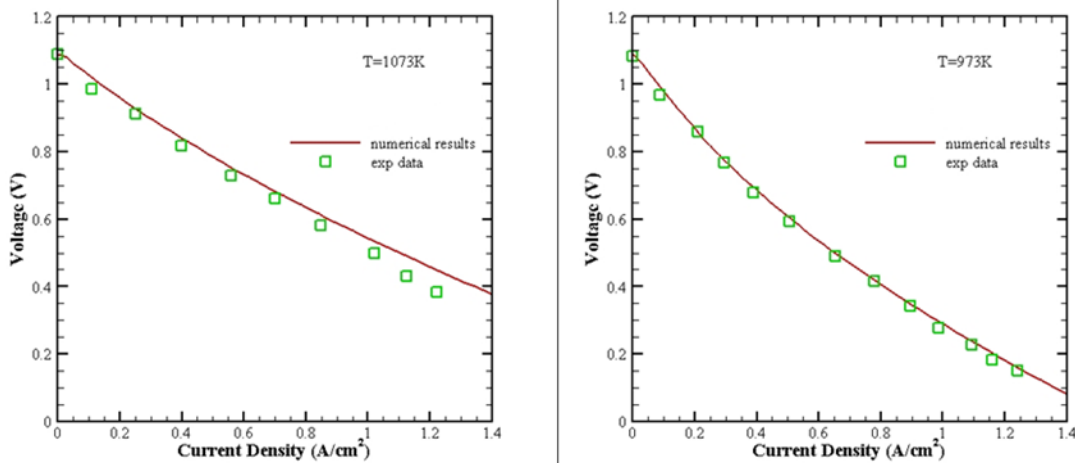


Figure 30 Comparison between numerical results and experimental data for case No. 2

The last experimental data is from S. P. Jiang [83]. The objectives of his experiments were to examine the influence of sintering temperature on cell performance by using an anode half-cell.

The paper provided SEM pictures of the anode microstructure at four different sintering temperatures. In Figure 31, the electronic and ionic particle sizes are approximated from the SEM pictures. The green and red circles are used denote Ni and 8 mol%  $\text{Y}_2\text{O}_3\text{-ZrO}_2$  (YZ8Y) particles, respectively. The range of particle size ratio that can maintain the percolation threshold is calculated to be between 0.5 and 2 for this volume fraction composition. At 1,300 °C, YSZ particle size is approximately 0.5  $\mu\text{m}$ , while the Ni particle size is about 2  $\mu\text{m}$  resulting in a particle size ratio of  $r = 0.25$ . Under these conditions, the assumptions of the model break down because the percolation threshold is not satisfied. Therefore the predicted results would not be valid. However, we can still use the closest limiting particle size ratio (i.e.  $r = 0.5$ ) to calculate an I-V curve to compare with the experimental data. For this case, the mathematical predictions should have better performance than experimental data because percolation threshold is assumed to be satisfied. This same approach is used for the 1,350 °C sintering temperature case, as well, because of the extreme particle size difference of two types of conductors (0.6  $\mu\text{m}$  for Ni and 2  $\mu\text{m}$  for YSZ resulting in  $r = 0.3$ ). For 1,400 °C, the Ni and YSZ particle size are estimated as 1.25  $\mu\text{m}$  and 1.5  $\mu\text{m}$ , respectively, resulting in  $r = 0.83$ . For 1,500 °C, both Ni and YSZ particle size are estimated as 2  $\mu\text{m}$ , resulting in  $r = 1$ . The particle size ratios are within the percolation threshold for the 1,400 and 1,500 °C sintering temperature cases and the numerical simulation can be applied. Once the particle sizes of electronic and ionic conductors are determined, the porosity is obtained by using the porosity-particle size ratio correlation. The method of calculating tortuosity in this case is a little different from the previous ones, in order to better match the provided experimental results. Since the paper provides the values of anode ohmic resistance, Equation (5) can be applied to estimate the tortuosity. However, if the porosity-tortuosity correlation is still applied, the estimated tortuosity would be an order of magnitude less the values which correspond to the resistance measurements.

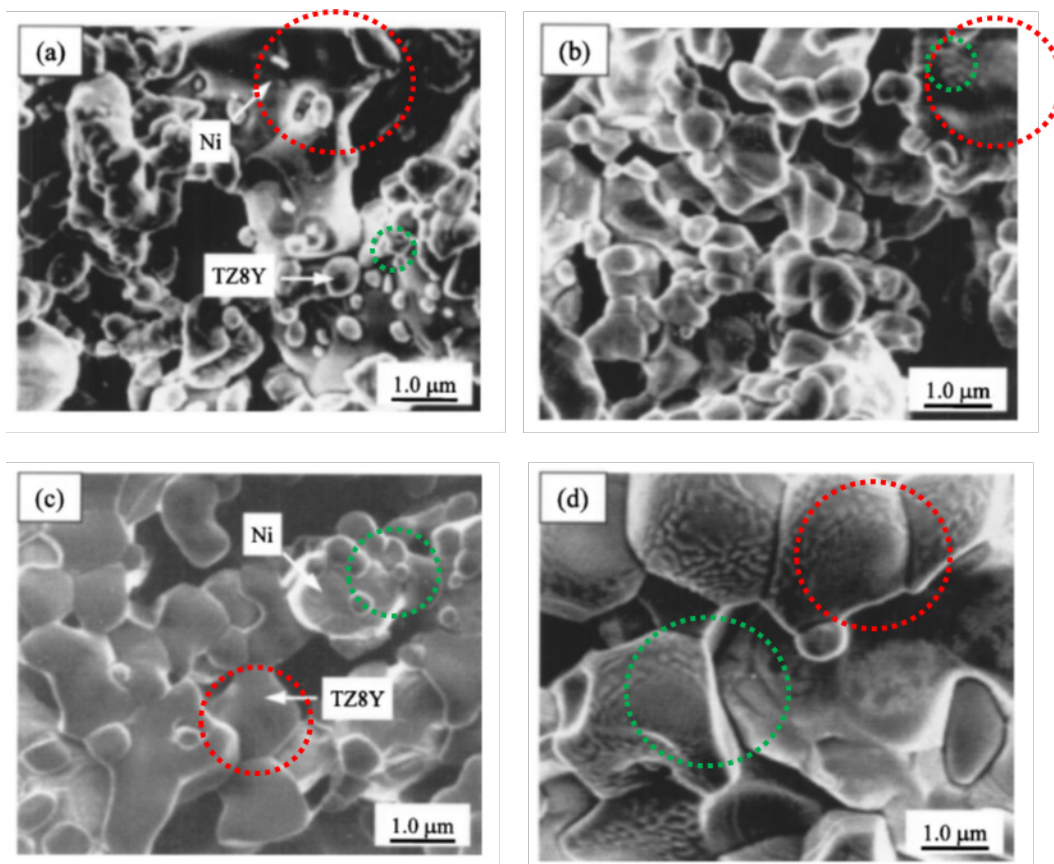


Figure 31 SEM of Ni/ 8 mol%  $\text{Y}_2\text{O}_3\text{-ZrO}_2$  (Ni/TZ8Y) Cermet Anodes Sintered at (a) 1300°C, (b) 1350°C, (c) 1400°C, (d) 1500°C

Figure 32 shows the comparison of model predictions vs. experimental data. It can be seen that for 1,400 and 1,500 °C sintering temperatures, the numerical results matched reasonably well with the experimental data. However, for the remaining two sintering temperatures, there is a noticeable difference between model results and experimental data, as expected. For these cases, the numerical model calculated a scenario where particle size ratio was artificially selected to satisfy the percolation threshold. However, in reality the particle size ratio falls outside the percolation threshold range indicating poor connectivity between the particles of the ionic and electronic conductors. Therefore, observed experimental data, where the terminal voltage drops rapidly and reaches zero at a very small current density value, follows with expected behavior based on our model assumptions.

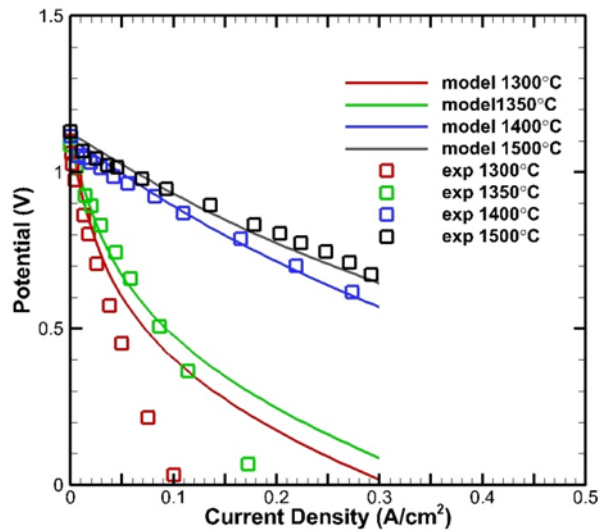


Figure 32 Comparison between Numerical Results and Experimental Data for Case No. 3

### 3.6 Model Sensitivity Study

The model validation showed a reasonable ability to predict experimental performance results from given cell microstructural parameters. Next, a sensitivity study is performed to investigate the effect of sub-model correlations on model predictions. The first experimental case from the model validation section is selected as a baseline. This is because the experiment has been tested and validated indicating a good consistency with the results from the numerical model. Also, it involves an anode half-cell only, so there is no need to worry about differentiating effects between the anode and cathode. Selected variables will be varied to test the sensitivity of model predictions to these variations, while the rest of the parameters will be obtained from the experiment validation case. In the sensitivity study, two different volume fractions are selected to perform the tests in order to expand the sample sizes.

Table 4 Value of input parameters for model validation case No. 2

<b>Parameter (provided by paper)</b>	<b>Value</b>
Operating Temperature	700°C / 800°C
Pressure	1.0 atm
Anode Thickness	1200 $\mu$ m
Electrolyte Thickness	7 $\mu$ m
Cathode Thickness	30 $\mu$ m
Anode Gas Composition	97% H <sub>2</sub> (3% H <sub>2</sub> O)
Cathode Gas Composition	air
Volume Fraction of NiO/YSZ	40%/60%
Mass Fraction of LSM/YSZ	50%/50%
Porosity	40%
NiO Particle Size (anode)	20-30nm
YSZ Particle Size (anode)	<300nm

### 3.6.1 Tortuosity vs. Porosity

There are two places containing the tortuosity parameter in the model. They are related to ohmic resistance in electrode and mass diffusion. First of all, since electronic conductivity is several orders of magnitude higher than the ionic conductivity, ohmic overpotential is primarily dominated by the resistance due to ionic conduction. Based on Equation (2-5), it can be found that increasing tortuosity will result in an increase in effective ionic resistivity and hence worsen the performance of the SOFC. Physically, this follows from the fact that as tortuosity increases, the path length for conduction from one end of the electrode to the other end increases. Secondly, the parameter of tortuosity also appears in the effective diffusivity to impact the gas diffusion process. From the eqn. (2-10), it can be seen that the increase of tortuosity will result in a decrease in the effective diffusion coefficient (or a corresponding increase in mass transfer resistance). In that case, a larger tortuosity will lead to a lower concentration of fuel at electrode-electrolyte interface and hence increase the concentration overpotential.

Table 5 Value of input parameters for model validation case No. 3

Parameter (provided by paper)	Value
Operating Temperature	1273 K
Pressure	1.0 atm
Anode Thickness	20-40 $\mu$ m
Electrolyte Thickness	0.9 $\pm$ 0.03mm
Anode Gas Composition	97% H <sub>2</sub> (3% H <sub>2</sub> O)
Volume Fraction of NiO/YSZ	50%/50%
NiO Particle Size	Approximate from SEM
YSZ Particle Size	Approximate from SEM

For this test case, the porosity is given as 30%. The idea is to vary the unknown parameter  $n$  in the porosity-tortuosity correlation given in eqn. (2-31) in order to find out how tortuosity impacts the model. The  $n$ -value is chosen to vary from 0.01 to 1 for 79%/21% Ni/YSZ and from 0.01 to 1.3 for 83%/17% Ni/YSZ, respectively. The overpotential values calculated from the corresponding varying  $n$  values are compared with the baseline experimental data, which is represented by the model with  $n = 0.5$  (which was used for the model validation case). The purpose is to explore how the  $n$ -value affects the predicted anode overpotential. Figure 33 shows a plot of tortuosity (which is a function of  $n$ ) versus the %-error difference when compared with the baseline experimental data (i.e.,  $n = 0.5$ ). The dashed region indicates the range of  $\pm 5\%$  difference between the predicted and experimental values of anode overpotential. In order to maintain the predicted overpotential between the 5% error bars, the range of the  $n$ -value is approximately from 0.275 to 0.685 for 79%/21% Ni/YSZ and from 0.08 to 0.79 for 83%/17% Ni/YSZ, respectively. Correspondingly, the tortuosity value and percentage range is about 1.4 - 2.25 (-23.3% - 33.7%) for 79%/21% Ni/YSZ, and 1.1 - 2.5 (-39.6% - 36.9%) for 83%/17% Ni/YSZ. This illustrates that a relatively large variation in the tortuosity value ( $\sim \pm 40\%$ ) results in a small impact on the predicted overpotential ( $\pm 5\%$ ).

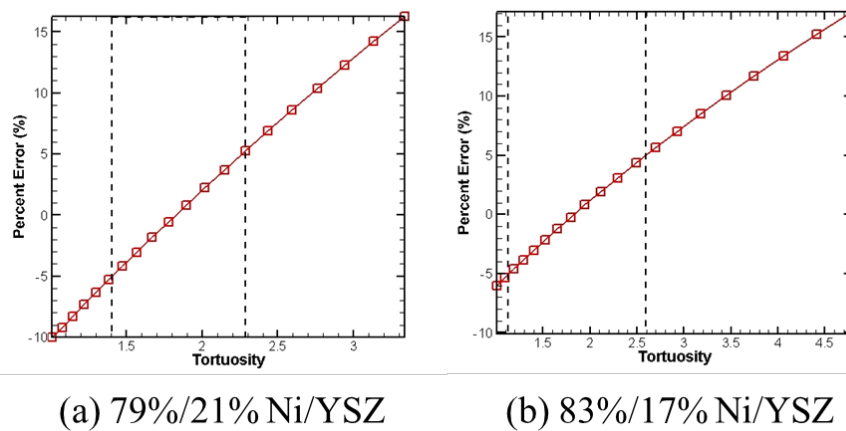


Figure 33 Comparison of Predicted Anode Overpotential at Different n-values

### 3.6.2 Particle size ratio vs. porosity

The anode governing equations indicates that both mass diffusion and electrochemical reaction rate depend on the particle size ratio. For 79%/21% volume fraction Ni/YSZ, the range of particle size ratio is calculated to be between 0.13 and 0.53 to maintain percolation threshold. For 83%/17% volume fraction Ni/YSZ, the range of particle size ratio is calculated to be between 0.1 and 0.4 to maintain percolation threshold. This means that the ionic conducting particles will always be smaller than the electronic conducting particles for this case. Based on the calculation from the numerical model, it can be found that as the particle size ratio increases (getting closer to 1), the active surface area decreases and results in an increase in cell overpotential as shown in Figure 34. This is because as particle size ratio ( $\alpha=r_i/r_e$ ) gets smaller (ionic particles get smaller or electronic particles get larger), the size difference of two types of conductors is expected to be more significant. Therefore electrochemical reactions rate will be boosted by increased contact area between the electronic and ionic conducting materials at the TPB region and hence improve the cell performance. For mass transfer, as particle size ratio increases (getting closer to 1), the diffusion coefficient will get smaller based on eqns. (2-11), (2-12), and (2-13), leading to an increase in the concentration overpotential. However, in this case, the particle size ratio impact for gas diffusion is not as significant due to an extremely thin anode thickness.

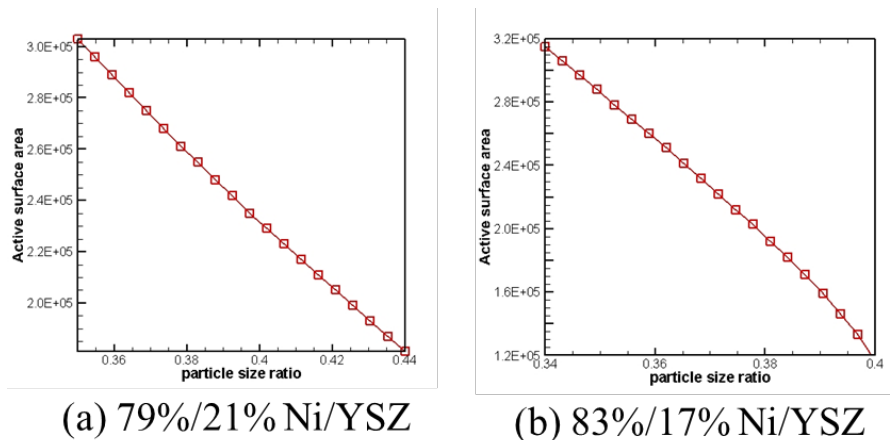


Figure 34 Effect of particle size ratio on active surface area



For both of the test volume fractions, the varying factor will be particle size ratio only. The particle size ratio is chosen to vary from 0.35 to 0.44 for 79%/21% Ni/YSZ and the experimental data is represented by selecting  $\alpha=0.4$ , which was used for the model validation case. For 83%/17% Ni/YSZ, the particle size ratio is varied from 0.34 to 0.4 and the experimental data is represented again by the  $\alpha$  value used for the validation case, which was 0.382. As shown in Figure 35, if the overpotential difference between numerical results and experimental data is expected to be within 5% error (dashed line region), the deviation of particle size ratio and its percentage needs to be 0.386 - 0.414 (-3.5% - 3.5%) for 79%/21% Ni/YSZ, and 0.376 - 0.385 (-1.3% - 1.1%) for 83%/17% Ni/YSZ, respectively. For both of the two volume fractions, the model performance predictions are strongly sensitive to the particle size ratio.

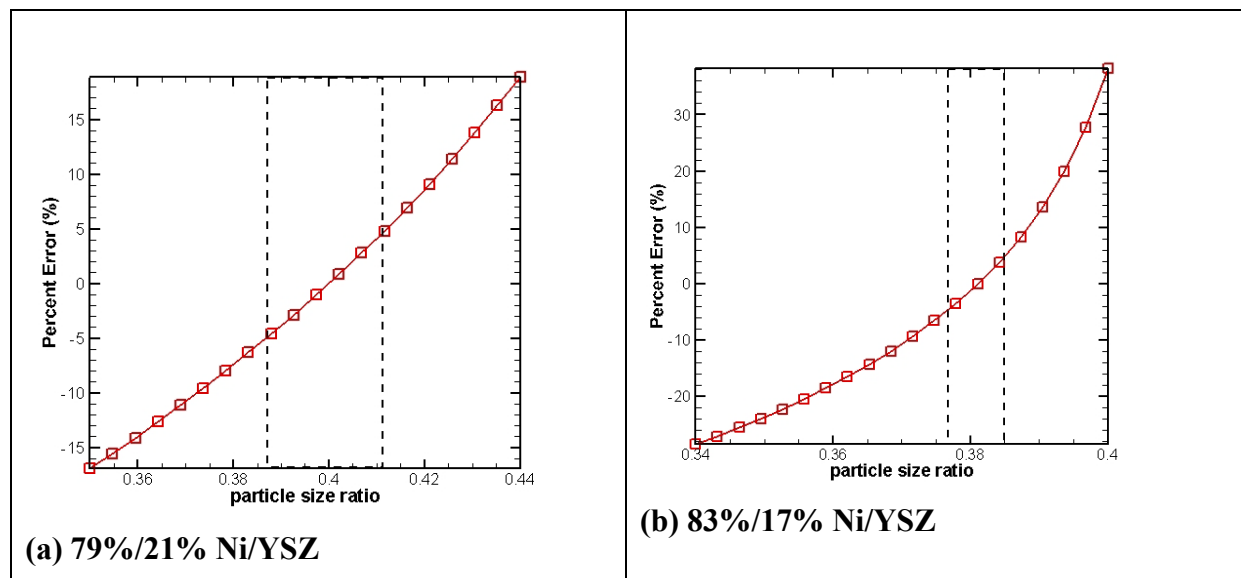


Figure 35 Comparison of Predicted Anode Overpotential at Different Particle Size Ratio Values

### 3.6.3 Discussion

To sum up, Table 6 lists the results of the sensitivity study for the sub-model correlations at two different volume fractions. It can be seen that the model is extremely sensitive to the porosity-particle size ratio correlation. These parameters can only be deviated within a narrow range, which is within  $\pm 3.5\%$  in order to maintain a  $\pm 5\%$  variation in the predicted overpotential for both of the volume fraction cases. Therefore, it is critical that this value to accurately determined and represented in the model. However, the model does not seem to be very sensitive to the porosity-tortuosity correlation. For a small variation in the predicted overpotential ( $\pm 5\%$ ), the tortuosity can have a deviation of up to  $\pm 20\%$  to  $\pm 30\%$ . Therefore, the porosity-tortuosity correlation adapted here should be valid to approximate tortuosity for model predictions.

Table 6 Results of sensitivity study

<i>Percent change corresponding to <math>\pm 5\%</math> change in predicted overpotential compared with experimental data</i>		
<b>Sample</b>	<i>79%Ni / 21% YSZ</i>	<i>83% Ni / 17% YSZ</i>
<b>Tortuosity</b>	-23.3% - 33.7%	-39.6% - 36.9%
<b>Particle size ratio</b>	-3.5% - 3.5%	-1.3% - 1.1%

#### 3.6.4 Conclusion

In this study, SOFC performance was investigated numerically by applying two sub-model correlations (porosity-tortuosity, porosity-particle size ratio) aiming to tie microstructural parameters to physically measurable parameters. The model was validated against available experimental data and demonstrated the potential to predict real SOFC performance numerically rather than spending tremendous time on performing expensive experiments. The sensitivity analysis was performed on the adopted sub-model correlations. It was determined that the porosity-particle size ratio correlation had a greater effect on predicted cell performance results than the porosity-tortuosity correlation. Since the model has the capability to differentiate which microstructural parameter plays a more important role in affecting the cell performance, this study has the potential to help improve cell efficiency and optimize cell performance by adjusting microstructural parameters.

## 4 Fabrication and Testing of Advanced Solid Oxide Fuel Cells

### 4.1 Impact of In-line Mixer for Printing Anode Interlayer:

One of the problems with printing anode interlayer is the fact that the two phases, NiO and YSZ do not mix well [84]. Layering effects were seen with phase segregation of NiO and YSZ. In order to improve the mechanical mixing, a mixer insert (a Teflon spiral) was introduced downstream. Four button cells were fabricated, two of which served as control cells. The anode interlayers for the control cells (a) and (b) were printed without the use of the mixer insert. Anode interlayers for cells (c) and (d) were printed using the mixer insert. The anode interlayers were printed on a NiO-YSZ support substrate. To print, NiO-YSZ interlayers, NiO ink and YSZ inks were prepared. YSZ ink was prepared by mixing the powder (Yttria stabilized zirconia) with solvent, plasticizers and dispersants. NiO ink was prepared in a similar manner using NiO powder. Details of ink preparation, mixing etc. can be obtained from ref (1). The same procedure for mixing described in ref. (1) was used. Several passes of the anode interlayer was printed on the NiO-YSZ support. For the electrolyte printing, YSZ ink was prepared. Several passes of YSZ was printed on the anode interlayer. Traditional slurry pasted LSM/YSZ cathode interlayer, and cathode current collection layer, LSM was used to complete the cell fabrication. Out of the four cells, one control cell failed. Results of the remaining three cells, (a), (c) and (d) are shown in Figure 36. The power densities of the cells fall in the range from 350 mW/cm<sup>2</sup> to 430 mW/cm<sup>2</sup> at 850 °C. Cells (a) and (c) show very similar values of current density and power density. The current density at 850 °C, at 600 mV overpotential is about 800 mA/cm<sup>2</sup>. Cell (d) shows somewhat improved performance. The current density at 850 °C, at 600 mV overpotential is about 1 A/cm<sup>2</sup>. The scatter in the results makes it difficult to make a conclusive statement about the impact of the in-line mixer. These experiments will be repeated. In order to evaluate the microstructure of these cells, scanning electron microscopy was carried out after electrochemical characterization. Fig 4-2 shows the scanning electron image (SEI) of the cross-section of a typical cell with anode interlayer. A dense electrolyte can be seen, about 12 μm thick. The remaining layers, anode interlayer Ni-YSZ, and cathode layers, LSM/YSZ and LSM are porous. The cathode interlayer and cathode current collection layer are not readily distinguishable from each other. Similarly the anode interlayer is not distinguishable from the anode substrate. Fig 4-3 shows the SEI of the region immediately below the electrolyte. In the case of cell (a) that contains no anode interlayer, the region seen is the anode substrate, Ni-YSZ. In the case of cells (c) and (d), the region seen is the anode interlayer, presumably 10-20 μm thick. The region is porous. However, the Ni and YSZ phases are not distinct. The phase contrast requires low voltage SEM work. No striking difference is seen between cell (a) and cells (c) and (d). In the current study the cell performance of all cells is better than the performance observed previously (Technical report submitted to Optomec Inc. /AFRL, October 2010). However the impact of in-line mixer remains unclear and needs further clarification/investigation.

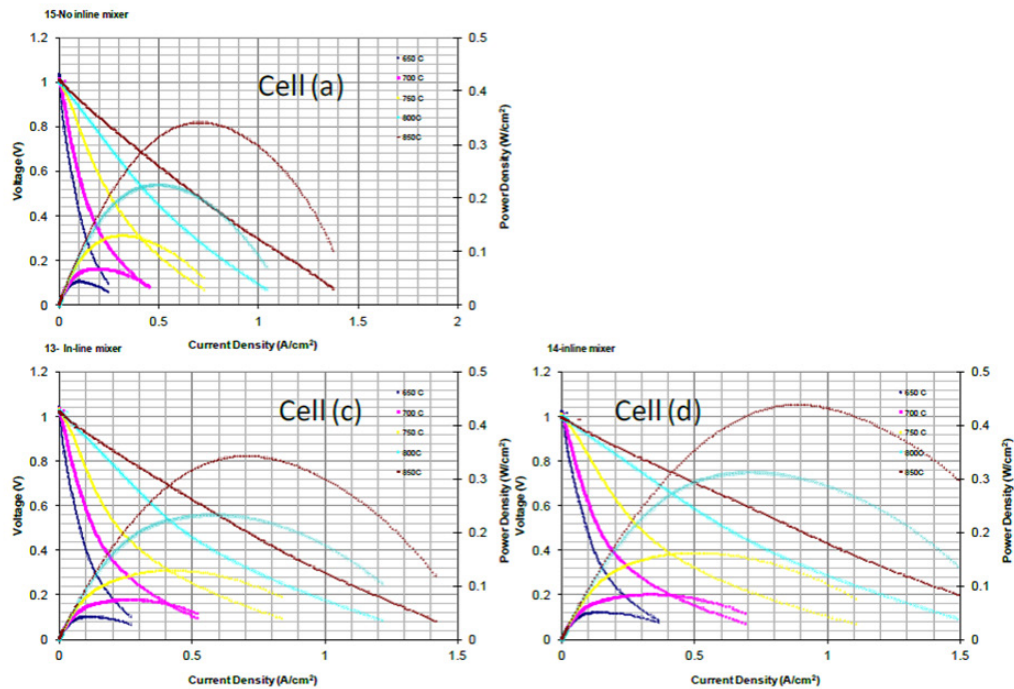


Figure 36 Cell (a) –no anode interlayer, (c) and (d)-cells with anode interlayer

## 4.2 Graded Braze Power Electronics

It was determined after showing some progress with silver nano paste but not having the micro pen operational that we should try different routes to achieve two tone metallic brazing. We decided to pursue a tape casting route.

Tape caste of silver nano particles was performed with success allowing for a solid tape that could be handled, hole punched and used as the center of the die attach layer. The first experiments used 4 single layers of Ag tape as the die attach layer. The results were documented into a power point while one of the images is shown in Figure 39. The next series of experiment used the hole-punched Ag tape as the center of the two tone layer. Unfortunately the escaping gasses skewed the layer resulting in a failed die attach. It has been determined that a small jig should be fabricated that will constrain the sample and allow for an even, consistent, and adequate pressure to be applied during the sintering process. Along with developing a jig it was also determined that a material set be purchased that would mimic the actual die attach scheme. Purchasing of DBC, Sic and effective back side metallization of the Sic wafers was investigated. Sources have been found and a proper back side metallization has been determined (Ti, Ni, Au).

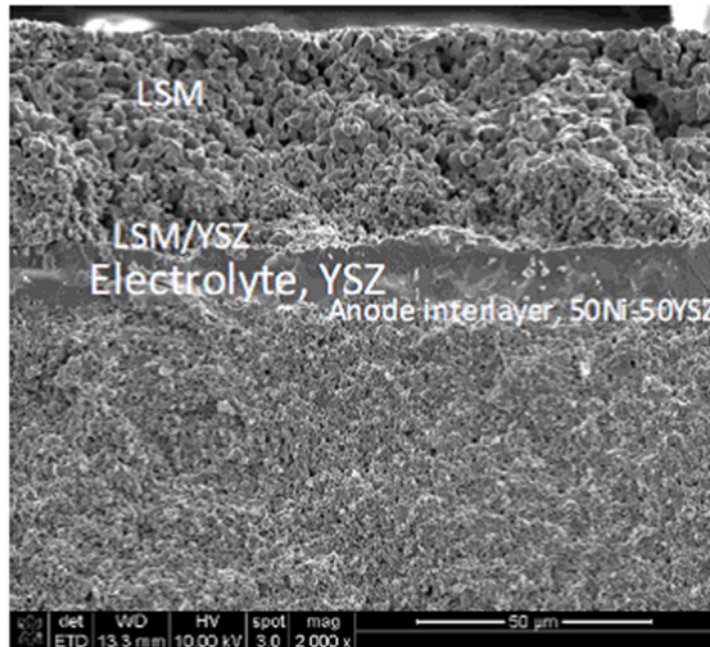


Figure 37 Cross Section of a Typical Cell with Anode Interlayer

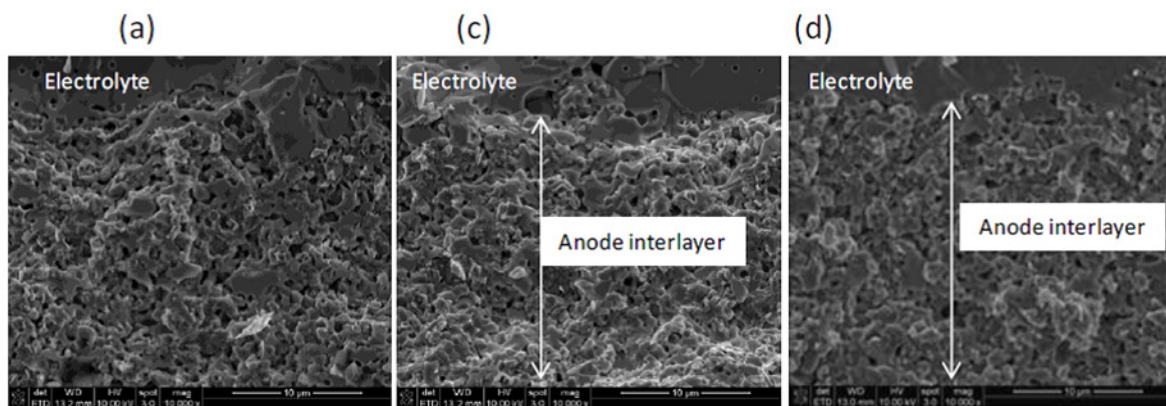


Figure 38 Scanning Electron Image of Cells (a), (c), and (d)

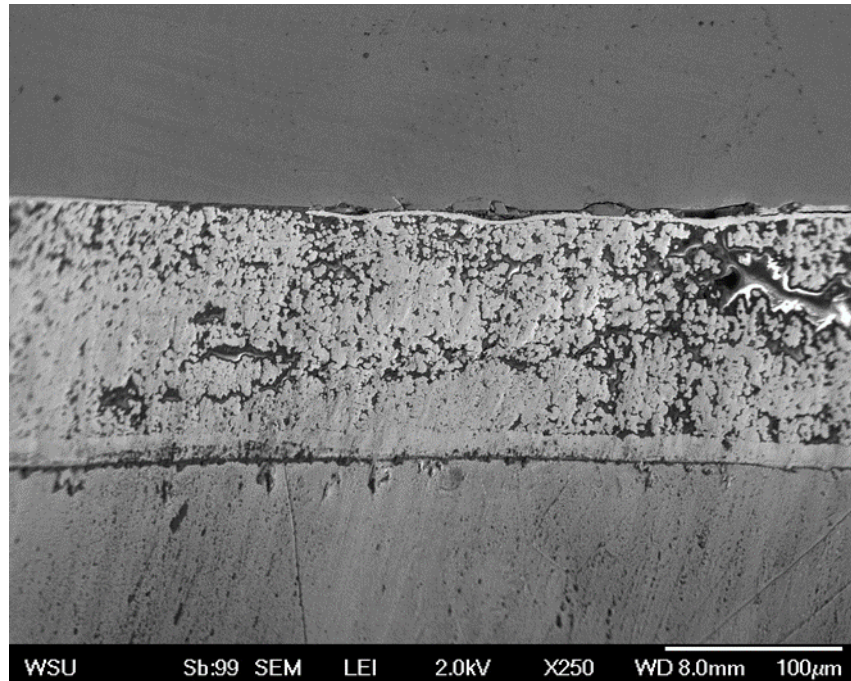


Figure 39 As Sintered @320C Ag Tape Die Attach Layer

While waiting for the finalization of the material set, side experiments have been investigated. It was mentioned in a paper that finding a way to increase the oxygen content in the die attach layer may help in the decomposition of the plastic deep in the center of the layer. It was thought that adding CuO to the Ag tape may supply additional oxygen while leaving behind copper metal during decomposition at elevated temperatures. A tape cast of CuO was made and fired at 300 °C to determine if the plastic decomposition would reduce the CuO into Cu during sintering. This did occur but the material quickly returned to CuO before the Cu could stabilize due to being in an O<sub>2</sub> environment at elevated temperatures. From this result it was determined that even if the CuO expedited the decomposition of the plastic it would re-oxidize and be ineffective as a thermal conductor and bonding material.

The idea of the addition of a flux has been tossed around so incorporating a flux into the tape was investigated. The most probable chemical reaction that could occur between the Ag nano particles with the plastic tape and the environment were determined to be oxidation of the Ag particles. The Gibbs free energy of this reaction was looked at within the processing temperature range. It was determined that after approximately 200C Ag oxidation ceases. Knowing this, future investigation into the synthesis of the tape caste has been performed looking for ways to protect the Ag nano particle from oxidation until it is above 200 °C. It has been determined that the dispersant will play the biggest role in preventing oxidation. This has led to looking at a few different tape caste recipes that use a more aggressive dispersant with strong surface absorption characteristics.



## 5 Measurement of Static and Dynamic Performance Characteristics of Small Electric Propulsion Systems

Unmanned aerial vehicles are being utilized by numerous groups around the world for various missions. Most of the smaller vehicles that have been developed use commercially-off-the-shelf parts, and little information about the performance characteristics of the propulsion systems is available in the archival literature. In light of this, the aim of the present research was to determine the performance of various small-scale propellers in the 4.0 to 6.0 inch diameter range driven by an electric motor. An experimental test stand was designed and constructed in which the propeller/electric motor was mounted in a wind tunnel for both static and dynamic testing, and the results were compared to those from previous studies. For static testing, the coefficient of thrust, the coefficient of propeller power, and the total propulsive efficiency, defined as the ratio of the propeller output power to the electrical input power, were plotted versus the propeller rotational speed. For dynamic testing, the rotational speed of the propeller was held constant at regular intervals while the airspeed was increased from zero to the windmill state. The coefficient of thrust, the coefficient of propeller power and the propeller efficiency were plotted versus the advance ratio for various rotational speeds. The thrust and torque were found to increase with rotational speed, propeller pitch and diameter, and decrease with airspeed. Using the present results and data from archival and non-archival sources, it was found that the coefficient of thrust could not be correlated with propeller diameter for square propellers where  $D = P$ . For a family of propellers (same manufacturer and application), correlations for the coefficient of thrust, the coefficient of propeller power and the propeller efficiency could be improved by modifying either the coefficients or the advance ratio with  $D/P$ . This dimensionless ratio allows for the propeller pitch to be accounted for in the performance coefficients.

### 5.1 Introduction

Interest in the performance of small propellers operating at low Reynolds numbers has grown recently. The aerospace industry has developed numerous unmanned aerial vehicles (UAVs) and has kept most of the data about the propulsion systems proprietary. Very little information is available in the archival literature about the performance characteristics of these motor and propeller combinations. The present research and others like it have aimed to gather and compare information about these small propulsion systems so that proper motor and propeller combinations can be selected for a given mission profile. Several papers were reviewed that relate directly to the present work and provide direction for the research.

Brandt and Selig experimentally determined efficiency as well as coefficients of thrust and power for low Reynolds number propellers [85]. The parametric ranges were as follows: Propeller diameter  $9 \leq D \leq 11$  inches, propeller rotational speed  $1500 \leq n \leq 7500$  RPM, and the incoming air velocity  $V_\infty'$  ranged from zero (static) to the windmill state of each propeller, i.e., that point at which the propeller generates zero thrust. A test stand was built inside the UIUC wind tunnel to measure thrust, torque, and propeller rotational speed. Freestream air velocity was measured using a Pitot tube and one of two differential pressure transducers depending on the airspeed range. Velocity corrections were applied to account for the change in upstream airspeed at the Pitot tube created by the propeller as well as the pressure change created by the fairing and the constriction of the propeller slipstream caused by the walls. In total, 79 propellers from four different manufacturers were tested to find the coefficient of thrust, the coefficient of power and

the propeller efficiency, all of which were plotted against advance ratio. The designs of the propellers ranged from those for electric motors to those used for fuel-powered engines. For each test, the rotational speed of each propeller was fixed while the freestream airspeed was varied. Four different values of propeller rotational speed ( $n = 3000, 4000, 5000, \text{ and } 6000 \text{ RPM}$ ) were tested for each of the propellers. The results show that the propeller efficiency increases with the propeller speed. This is primarily due to the increase in Reynolds number as the propeller spins faster. Overall, the propeller efficiency ranged from  $28 \leq \eta_p \leq 65\%$ . The propellers were also tested statically, but the data is only available in the UIUC propeller database [96].

Gamble designed an intricate LabVIEW program to automatically collect data and generate propeller performance plots [89]. A dynamometer was constructed using beam-type load cells to measure thrust and torque. The development of the LabVIEW program was detailed as well as a procedure for carrying out the experiment. Propellers were tested for repeatability by performing identical experiments over several days with two identical propellers. The results primarily focus on the effect of the Reynolds number on thrust and power coefficients and efficiency versus advance ratio. Thrust versus velocity was compared for propellers with constant diameter and varying pitch. Lastly, advance ratio was modified by replacing diameter with pitch in the equation for advance ratio. The optimal advance ratio is shown using this technique. This allows for the optimal pitch of a model propeller to be selected to achieve maximum efficiency. The diameter can then be chosen from plots of thrust versus velocity to produce the required thrust for the airframe.

Deters and Selig performed static tests on smaller propellers ranging from  $2.5 \leq D \leq 5$  inches in diameter [88]. Static coefficients of thrust and power as well as the figure of merit ( $\text{FOM} = C_T^{3/2} / \sqrt{2} C_P$ , typically used to measure the efficiency of helicopters) using modified coefficients of thrust and power that use disk area and tip speed were determined experimentally. The test stand utilized a 0.3 kg load cell and a 25 oz-in torque transducer to measure thrust and torque, respectively. Propeller rotational speeds ranging from  $2500 \leq n \leq 27,000 \text{ RPM}$  were measured using an infrared detector. A schematic of the test stand indicated the locations of the components and a fairing surrounding the load cell and torque transducer. Calibrations of the components were performed and data was collected using a data acquisition board. The geometry of each propeller was found using PropellerScanner software to find the chord and twist distribution [92]. This was used to calculate the Reynolds number at the 75% chord location. Results show that over the rotational speed range tested, the figure of merit remained fairly constant throughout the test. The results also show that a larger diameter propeller is more efficient than a smaller one, and a propeller with a lower pitch is more efficient than one with a higher pitch.

Ol et al. took a more analytical approach to studying small propellers operating at low Reynolds numbers [95]. Iterative methods were used to calculate the coefficient of thrust, the coefficient of torque, and the propeller efficiency using propeller momentum theory and blade-element methods. Propellers were discretized by cutting and tracing sections as well as digital scans. Leading and trailing edges were fitted to the UIUC propeller library so that the resulting analysis in XFOIL would successfully converge. The iterative process for thrust was dependent on the various Reynolds numbers across the propeller blade at a given rotational speed. Two separate experimental setups were constructed to compare the numerical results. Propellers in the  $6 \leq D \leq 12$  inch range were tested in the Langley Research Center Basic Aerodynamics Research Tunnel (BART) and larger propellers in the  $14 \leq D \leq 20$  inch range were tested in the AFRL Vertical



Wind Tunnel (VWT). Static tests were performed with the wind tunnel sides open to alleviate the induced airflow velocity inside the wind tunnel. Blockage corrections were applied to BART tests but not to VWT tests, since the tunnel diameter of the VWT was greater than five times the diameter of the propellers tested. Drag on the test stand was corrected by sweeping tunnel velocity and generating curve fits that were used to adjust the actual data. A large sensitivity to twist distribution was observed in the tests and the analysis. Ol et al. postulated that plots of torque coefficient versus advance ratio are sometimes misleading because they do not account for Reynolds number effects. It was also shown that when the ratio of diameter to pitch is scaled ( $10 \times 10$  to  $12 \times 12$ , for example) the experimental data fits together well within the bounds of error. Modifications to the dimensionless terms to factor in propeller pitch were presented, however more research was deemed necessary to apply this theory.

Corrigan and Altman examined different methods for wind tunnel blockage corrections [87]. These methods included the Glauert correction as well as a correction by Hackett et al. [90, 91]. These methods were described in detail and their applications were shown. A wind tunnel experiment was designed and constructed to record the necessary variables to calculate total propulsive efficiency. This is in contrast to other works that primarily explored propeller efficiency. The stand was constructed using a beam-type load cell and a reaction torque sensor. Three propellers ( $D = 10, 12$ , and  $14$  inches) were tested using different motors for each propeller. Static pressure taps were used on the wall of the wind tunnel test section to record the changes in pressure forward and aft of the propeller disk plane for the velocity corrections. The Glauert method did not provide sufficient correction for large blockage conditions. The Hackett method yielded more correction at higher airspeeds and larger propeller diameters, but the method could not be validated and therefore further work was found to be necessary.

Merchant and Miller performed dynamic tests on propellers in the  $6 \leq D \leq 22$  inch range [94]. A test stand was constructed to record propeller performance parameters, where the thrust and torque were collected by a combined thrust/torque cell. The load/torque cell was calibrated using dead weights in the axial (thrust) and transverse (torque) directions. Wind tunnel velocity was measured directly using a Pitot probe and a differential pressure transducer. Since the propellers were large compared to the test section, blockage corrections developed by Glauert were applied to the results. Readings were taken at wind-off-zero conditions before and after each test [90]. These values were then averaged and subtracted from the test data to account for zero drift and temperature effects. Data was collected at constant propeller rotational speeds and the wind tunnel velocity was varied to sweep through values of advance ratio. The results were compared to other works and were shown to be acceptable. The setup was also tested for variations in flow angularity. Pitch and yaw variations between  $-3$  and  $+3$  arc degrees were examined and it was shown that only the coefficient of thrust was affected by a change in pitch. However, it was shown that pitch variations of  $-3$  and  $+3$  degrees yielded the same results, which indicated that the system was symmetric in the pitch direction. Lastly, two identical propellers made by the same manufacturer were tested and compared, which showed that for some propellers there may be significant differences in performance due to manufacturing. Very limited results were presented, however, and the results shown only give a small sample of the entire test range.

The objective of the present research was to determine the performance of various commercially-available small-scale propellers driven by an electric motor. An experimental test stand was designed and constructed in which the electric motor was mounted in a wind tunnel at Wright State University for both static and dynamic testing. The freestream airspeed was varied from

zero to the windmill state for each propeller. The rotational speed was varied over the operational range recommended by the propeller manufacturers, while ensuring that the electric motor did not overheat. The primary measurement devices were calibrated, and an extensive uncertainty analysis was performed. The results from the present experiment were compared to those from previous studies for both static and dynamic data. For static testing, the coefficient of thrust, the coefficient of propeller power and the total propulsive efficiency were plotted versus the propeller rotational speed. For dynamic testing, the rotational speed of the propeller was held constant at regular intervals while the freestream airspeed was increased from zero to the maximum. The coefficient of thrust, the coefficient of propeller power and the propeller efficiency were plotted versus the advance ratio for various rotational speeds.

## 5.2 Background

The performance characteristics to be determined by the experimental setup are as follows. The coefficients of thrust, torque and propeller power, and the propeller efficiency are Merchant and Miller [94]:

$$C_T = \frac{T'}{\rho n^2 D^4}, \quad C_Q = \frac{Q}{\rho n^2 D^5}, \quad C_P = \frac{P_p}{\rho n^3 D^5}, \quad \eta_P = \frac{J C_T}{C_P}$$

The three performance coefficients and the propeller efficiency defined above are typically plotted against the advance ratio for dynamic testing:

$$J = \frac{V'_\infty}{nD} \quad (5-1)$$

where the corrected freestream velocity is :

$$V'_\infty = V_\infty \left[ 1 - \frac{\tau_4 \left( \frac{A_p}{A_{WT}} \right)}{2\sqrt{1+2\tau_4}} \right] \quad (5-2)$$

The uncorrected freestream velocity is:

$$V_\infty = \sqrt{\frac{2P_{\text{diff}}}{\rho}} \quad (5-3)$$

The Glauert correction variable is:

$$\tau_4 = \frac{T'}{\rho A_p V_\infty^2} \quad (5-4)$$

The propeller disk area and wind tunnel area are, respectively:

$$A_p = \frac{\pi D^2}{4}, \quad A_{WT} = W^2 \quad (5-5)$$

The corrected thrust is defined as the measured thrust minus the drag force due to the flow of air over the motor, torque cell and load cell [97]:

$$T' = T - F_D \quad (5-6)$$

The total propulsive efficiency is the ratio of the propeller output power to the electrical input power:

$$\eta_T = \frac{P_P}{P_e} = \frac{2\pi n Q}{VI} \quad (5-7)$$

The density of air is given by the perfect gas law:

$$\rho = \frac{P_{\text{atm}}}{RT_{\text{atm}}} \quad (5-8)$$

### 5.3 Experimental setup

The objective of the present experiment was to determine the performance characteristics of small electric motor/propeller combinations from static conditions to the windmill state. The overall design of the dynamic test rig is shown in Figure 40. The electric motor was directly attached to a 25 oz-in torque cell (Transducer Techniques, Model RTS-25), which was able to withstand 10 kg in thrust and 1.7 kg in shear. The torque cell was in turn mounted onto a 1-kg single point beam-type load cell (Transducer Techniques, Model LSP-1). Each cell was driven by a signal conditioner (Transducer Techniques, Model TMO-1) that produced a 0 to 5 Volt linear output. The assembly of the motor, torque cell and load cell is shown in Figure 41. The motor was held in place with a custom-designed clam-shell clamp, in which fins were incorporated to increase the convective heat transfer from the electric motor.

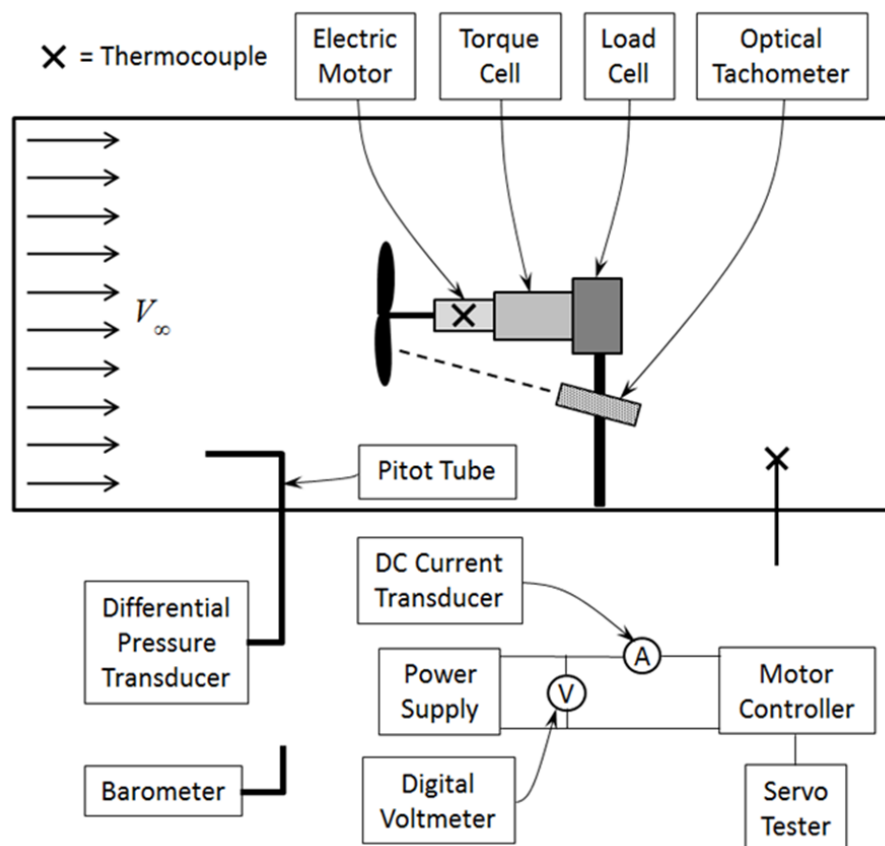


Figure 40 Schematic Diagram of the Experimental Setup

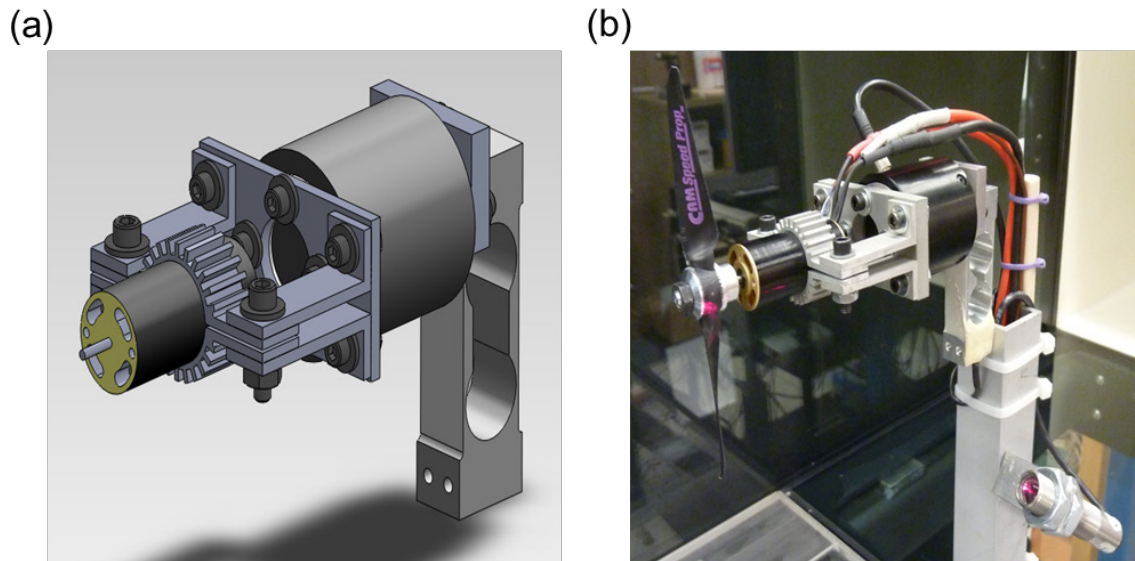


Figure 41 Assembly of Motor, Torque Cell and Load Cell: (a) Solid Model Representation; (b) Photograph

The load cell was attached to a section of 1.25-inch square aluminum tubing, which acted as a riser to place the propeller in the middle of the test section. The bottom of the riser was connected to an optical breadboard table (Melles-Griot, Model BBSS-25-610-1219) using flanges of angle aluminum. A hole was milled in the acrylic floor of the wind tunnel for the aluminum riser to pass through. The low-speed wind tunnel at Wright State University is an open circuit design capable of producing speeds from 0.6 to 36 m/s with a contraction ratio of 6.25:1. The square entrance of the wind tunnel has a 3.8 m<sup>2</sup> opening with aluminum hexagonal honeycomb sections that serve as a flow straightener. The height and width of the square test section is  $W = 0.6096$  m, and its length is 2.438 m. Doors on one side of the test section allow for an entire wall to be opened for easy access.

The data acquisition system used to collect data from the instrumentation consisted of a DAQ board (National Instruments, Model SCC-68) and a DAQ card (National Instruments, Model PCI-6221) installed in a PC. Shielded wires were used to connect the outputs of the transducers to the DAQ board. The electric motor driving the propeller was energized using a precision DC power supply (Hewlett-Packard, Model 6012B). A servo tester (GWS, Model MT-1) was used to control the rotational speed of the propeller. The voltage supplied to the electric motor was measured using a digital multi-meter (National Instruments, Model USB-4065). To measure the current, a DC Hall effect current transducer (CR Magnetics, Model CR5210-30) with a range of 0 to 30 A was placed in-line between the power supply and the motor speed controller.

A remote optical sensor (Monarch Instrument, Model ROS-W) connected to a panel meter (Monarch Instrument, Model ACT-3X) was used to measure propeller rotational speed. Reflective tape supplied with the sensor was placed near the hub on the leeward side of the propeller so that the optical sensor did not have to be adjusted between runs.

Atmospheric pressure was measured to determine the density of the air. To record atmospheric pressure, a barometer (Vaisala, Model PTB110) capable of measuring 500 to 1100 mbar with accuracy of  $\pm 0.3$  mbar was used. The differential pressure produced by the Pitot tube was measured using a differential pressure manometer (MKS, Model 226A). The height of the Pitot

tube from the floor of the wind tunnel was selected by traversing the boundary layer thickness using the Pitot tube as outlined. The height was set to  $H = 2.5$  inches, and the Pitot tube was made parallel to the wind tunnel walls by using a bubble level and a custom-made jig.

The temperature of the motor was measured using a Type T thermocouple while the temperature of the air inside the wind tunnel was measured using a Type E thermocouple probe (Omega, Model EMQSS-125G-12). The Type T thermocouple junction was placed on the center of the motor and was held in place by the aluminum clam-shell clamp. The Type E probe was mounted in the floor of the wind tunnel ahead of the motor/propeller so that the sensing junction extended into the airflow. The thermocouples were connected to thermocouple modules (National Instruments, Model SCC-TC01) on the data acquisition board. The signals from the eight sensors were read using custom-designed LabVIEW virtual instruments.

The twenty-four propellers selected for analysis ranged from  $4.0 \leq D \leq 6.0$  inches in diameter and  $2.0 \leq P \leq 5.5$  inches in pitch, as shown in Table 7. Some of the propellers were selected to overlap with previous research so that the procedures and test setup used for the measurements could be compared and validated. The GWS  $4.5 \times 3.0$  and GWS  $5.0 \times 4.3$  inch propellers were tested statically and compared to Deters and Selig [88]. An APC  $8.0 \times 3.8$  inch Slow Flyer was tested dynamically and compared to the results posted on the UIUC Propeller Database while an APC  $6.0 \times 4.0$  inch propeller was tested dynamically and compared to the results presented by Ol et al. [95, 96].

Table 7 Summary of Propellers Studied.

<b>Manufacturer</b>	<b>Nominal <math>D/P</math> (in <math>\times</math> in)</b>	<b>Designation</b>
APC	$4.10 \times 4.10$	Speed 400 Electric
APC	$4.20 \times 2.00$	Sport
APC	$4.20 \times 4.00$	Free Flight
APC	$4.50 \times 4.10$	Speed 400 Electric
APC	$4.70 \times 4.25$	Speed 400 Electric
APC	$4.75 \times 4.75$	Speed 400 Electric
APC	$4.75 \times 5.50$	Speed 400 Electric
APC	$5.10 \times 4.50E$	Thin Electric
APC	$5.25 \times 4.75$	Speed 400 Electric
APC	$5.50 \times 2.00$	Free Flight
APC	$5.50 \times 4.50$	Speed 400 Electric
APC	$6.00 \times 2.00$	Sport
APC	$6.00 \times 4.00 E$	Speed 400 Electric
APC	$8.00 \times 3.8$	Slow Flver
Graupner	$4.00 \times 3.00$	Cam Speed
Graupner	$4.70 \times 4.00$	Cam Speed
Graupner	$4.70 \times 4.70$	Cam Speed
Graupner	$5.50 \times 4.30$	Cam Speed
Graupner	$5.50 \times 5.50$	Cam Speed
GWS	$4.00 \times 2.50$	
GWS	$4.00 \times 4.00$	
GWS	$4.50 \times 3.00$	
GWS	$5.00 \times 3.00$	
GWS	$5.00 \times 4.30$	

#### 5.4 Uncertainty analysis

The uncertainties of all of the calculated results described in the above equations were determined using the root-sum-square uncertainty method [93]. During experimentation, eight primary measurements were made using the data acquisition system: Uncorrected thrust ( $T$ ); torque ( $Q$ ); propeller rotational speed ( $n$ ); atmospheric pressure ( $P_{\text{atm}}$ ); atmospheric temperature ( $T_{\text{atm}}$ ); Pitot tube pressure difference ( $P_{\text{diff}}$ ); motor voltage ( $V$ ); and motor amperage ( $I$ ). The uncertainty of a given measurement was estimated to be the sum of the calibration uncertainty and the confidence interval of the collected data set at a confidence level of 99%:

$$\Delta U = \Delta U_{\text{CAL}} + \Delta U_{99} \quad (5-9)$$

In order to calibrate the torque cell, two identical arms were attached to the sides of the motor clamp so that the torque cell could be calibrated in both directions of rotation simultaneously. Varying weights were hung from one of the arms to calibrate in the clockwise direction, and then the process was repeated for the counterclockwise direction. The load cell used to measure thrust was calibrated in situ as follows: A strand of fishing line was attached to the front of the propeller using aircraft wire. This strand was then passed over a smooth cylinder with bearings mounted in the wind tunnel. Varying weights were suspended from the fishing line over the expected range of thrust, and voltage readings were recorded.

The drag of the fixture was measured versus airspeed by removing the propeller and replacing it with a propeller hub with the blades removed. The airspeed was increased systematically while data was collected from the load cell and the Pitot tube. The free-stream velocity was then calculated and the measured drag was plotted against the velocity. A second-order regression was applied to the points and this equation was used in the calculation of the corrected thrust.

Table 8 gives the uncertainties for each device or transducer used to collect the data. The principal equations used for determining the uncertainties of the computed quantities shown in the graphs in the Results and Discussion section are shown below.

*Coefficient of Thrust:*

$$\Delta C_T = \left[ \left( \frac{\Delta T}{\rho n^2 D^4} \right)^2 + \left( \frac{-T \Delta \rho}{\rho^2 n^2 D^4} \right)^2 + \left( \frac{-2T \Delta n}{\rho n^3 D^4} \right)^2 + \left( \frac{-4T \Delta D}{\rho n^2 D^5} \right)^2 \right]^{\frac{1}{2}} \quad (5-10)$$

*Coefficient of Torque:*

$$\Delta C_Q = \left[ \left( \frac{\Delta Q}{\rho n^2 D^5} \right)^2 + \left( \frac{-Q \Delta \rho}{\rho^2 n^2 D^5} \right)^2 + \left( \frac{-2Q \Delta n}{\rho n^3 D^5} \right)^2 + \left( \frac{-5Q \Delta D}{\rho n^2 D^6} \right)^2 \right]^{\frac{1}{2}} \quad (5-11)$$

*Coefficient of Power:*

$$\Delta C_P = \left[ \left( \frac{\Delta P_P}{\rho n^3 D^5} \right)^2 + \left( \frac{-P_P \Delta \rho}{\rho^2 n^3 D^5} \right)^2 + \left( \frac{-3P_P \Delta n}{\rho n^4 D^5} \right)^2 + \left( \frac{-5P_P \Delta D}{\rho n^3 D^6} \right)^2 \right]^{\frac{1}{2}} \quad (5-12)$$

*Propeller Efficiency:*

$$\Delta\eta_P = \left[ \left( \frac{C_T \Delta J}{C_P} \right)^2 + \left( \frac{\Delta C_T J}{C_P} \right)^2 + \left( \frac{-J C_T \Delta C_P}{C_P^2} \right)^2 \right]^{\frac{1}{2}}$$

(5-13)

*Advance Ratio:*

$$\Delta J = \left[ \left( \frac{\Delta V'_\infty}{nD} \right)^2 + \left( \frac{-V'_\infty \Delta n}{n^2 D} \right)^2 + \left( \frac{-V'_\infty \Delta D}{nD^2} \right)^2 \right]^{\frac{1}{2}}$$

(5-14)

*Total Propulsive Efficiency:*

$$\Delta\eta_T = \left[ \left( \frac{2\pi n \Delta Q}{VI} \right)^2 + \left( \frac{2\pi Q \Delta n}{VI} \right)^2 + \left( \frac{-2\pi n Q \Delta V_e}{V^2 I} \right)^2 + \left( \frac{-2\pi n Q \Delta I}{VI^2} \right)^2 \right]^{\frac{1}{2}}$$

(5-15)



Table 8 Uncertainties of Primary Measurement Sensors and Calibration Sources.

Measurement	Sensor	Uncertainty
Thrust, $T$	Transducer Techniques LSP 1kg Load Cell	$\Delta T_{\text{cal}} = \pm 7.70 \text{ g}$
Torque, $Q$	Transducer Techniques RTS 25 oz-in Reaction Torque Sensor	$\Delta Q_{\text{cal}} = \pm 0.0498 \text{ g-m}$
Atmospheric Temperature, $T_{\text{atm}}$	Omega Type E Thermocouple	$\Delta T_{\text{atm,cal}} = \pm 0.0334 \text{ }^{\circ}\text{C}$
Calibration Mass	Ohaus Digital Scale	$\Delta m = \pm 1.00 \times 10^{-3} \text{ g}$
Propeller Diameter, $D$	Digital Vernier Calipers	$\Delta D = \pm 1.00 \times 10^{-5} \text{ m}$
Propeller Rotational Speed, $n$	Monarch Instruments Remote Optical Sensor (ROS) and ACT 3x Panel Tachometer	$\Delta n = \pm 1 \text{ RPM}$
Motor Voltage, $V$	National Instruments USB-4065 Digital Multi-Meter	$\Delta V = \pm 1.00 \times 10^{-3} \text{ V}$
Motor Current, $I$	CR Magnetics CR5210-30 Current Transducer	$\Delta I = \pm (1\% \times \text{Reading})$
Atmospheric Pressure, $P_{\text{abs}}$	Vaisala PTB110 Barometer	$\Delta P_{\text{atm}} = \pm 30.0 \text{ Pa}$
Pitot Tube Differential Pressure, $P_{\text{diff}}$	MKS 226A Differential Pressure Manometer	$\Delta P_{\text{diff}} = \pm (0.3\% \times \text{Reading})$

## 5.5 Experimental procedures

Two separate procedures were developed for the static and dynamic tests. For all of the tests, the power supply driving the motor controller for the propeller motor was turned on and set to a nominal output of 11.1 Volts, which matches the voltage output of a standard 3-cell lithium-polymer battery. Then, the data acquisition system and the signal conditioners driving the sensors were powered up for the warm-up periods recommended by the manufacturers.

### 5.5.1 Static test procedure

After the warm-up period, the load cell and torque cell were zeroed by adjusting the balance potentiometers on the signal conditioners so that the voltage outputs were as close as possible to zero. At this point, five hundred data points were collected with the propeller motor off to obtain baseline values for the load cell and torque cell. The propeller motor was then set to the first desired speed setting and one thousand data points were collected. The propeller motor was then

turned off and another set of 500 data points was acquired. The average values for thrust and torque from the two propeller-off states were averaged and this value was used to correct the thrust and torque measurements to account for zero drift and temperature effects (Merchant and Miller, 2008). The process was then repeated for increased values of rotational speed until the maximum speed was achieved.

### 5.5.2 Dynamic test procedure

After the warm-up period, the differential pressure transducer reading the Pitot tube and the signal conditioners reading the load cell and the torque cell were zeroed. Five hundred data points were taken with the propeller motor off and the wind tunnel motor off. At the end of the first five hundred points, the propeller motor was set to the desired rotational speed setting and the wind tunnel airspeed was set to the first desired setting. After the system reached steady state, one thousand data points were acquired. Next, the wind tunnel airspeed setting was changed and the propeller rotational speed was adjusted to match the original setting. This process was repeated until the windmill state of the propeller was reached. The propeller motor and the wind tunnel motor were both stopped at this point, and then five hundred data points were collected in order to again account for drift in the sensors. Data sets were collected for approximately ten wind tunnel airspeed settings for each of the four rotational speed settings for each propeller tested.

## 5.6 Results and discussion

To ensure that the collected data was repeatable and correct, tests were necessary to validate the static and dynamic results. The first type of test checked for repeatability of the same propeller as well as the repeatability across three identical propellers. The second type of test was to compare the results of the present experiment to published results from researchers using the same propeller. A complete summary of the data collected from the static and dynamic tests is provided by Brezina [86].

### 5.6.1 Validation of the static test

To check the repeatability of the experiment, three identical Graupner  $4.7 \times 4.7$  inch propellers were tested under static conditions three times each, thus creating a total of nine sets of data. This was done to determine the repeatability of the experiment for multiple runs of the same propeller as well as establishing whether manufacturing variability affected the performance of identical propellers. Figure 42 shows typical results for a static propeller, where both the thrust and torque increase monotonically with rotational speed. The coefficients of thrust and propeller power were relatively constant, whereas the total efficiency reached a peak value at approximately  $n = 20,000$  RPM. The uncertainties of the coefficients of thrust and propeller power increased significantly at the lowest propeller rotational speed. This was driven by the uncertainty of the load cell and the torque cell at relatively small values of thrust and torque. Figure 43 shows that the repeatability of the reduced data (coefficient of thrust, coefficient of propeller power and total propulsive efficiency) was excellent. The data from all nine tests fall within the uncertainty bounds for the first run. The duplicate propellers also fall directly in line, meaning that, at least for this type of propeller, manufacturing differences can be neglected.

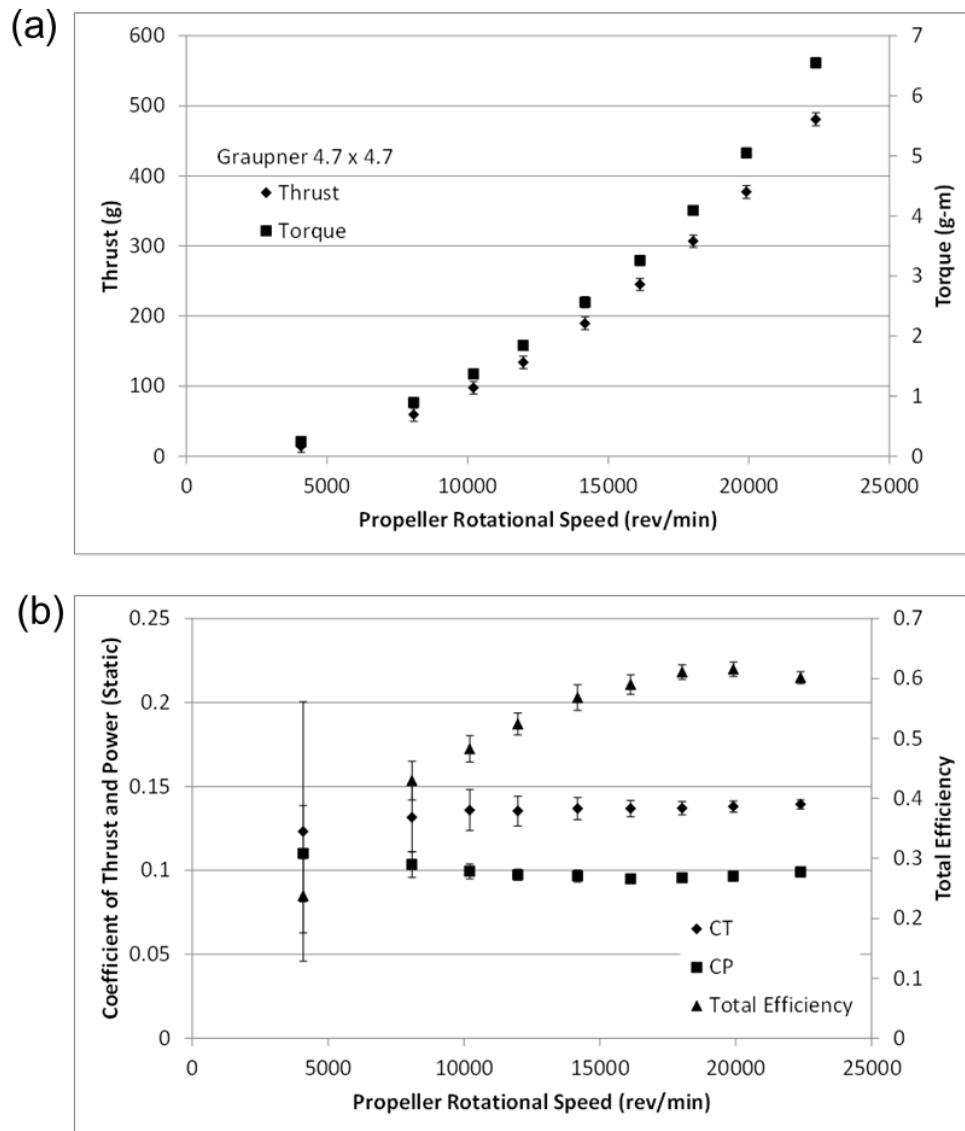


Figure 42 Typical Static Test Results  
 (Graupner  $4.7 \times 4.7$  inch Propeller): (a) Thrust and Torque versus Rotational Speed, (b) Coefficient of Thrust, Coefficient of Propeller Power and Total Propulsive Efficiency versus Rotational Speed.

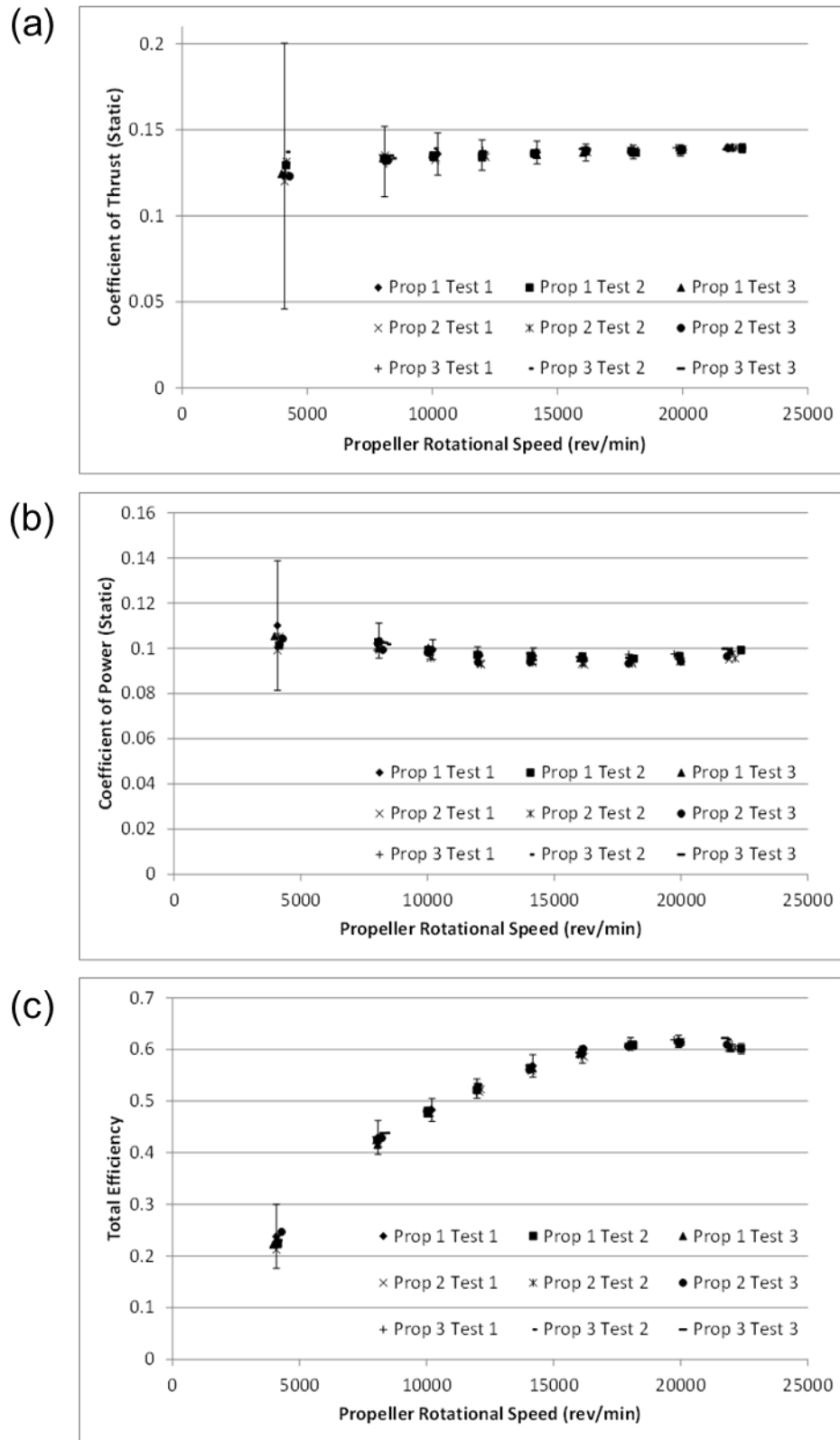


Figure 43 Comparison of Three Identical Propellers under Static Testing  
(Graupner 4.7 × 4.7): (a) Coefficient of Thrust, (b) Coefficient of Propeller Power, (c) Total Propulsive Efficiency.

Static tests were performed on two propellers (GWS  $4.5 \times 3.0$  and GWS  $5.0 \times 4.3$ ) which matched tests performed by Deters and Selig [88]. The coefficient of thrust and the coefficient of power were compared to data provided by Deters and Selig as shown in Figure 44, where the results for both propellers show good agreement.

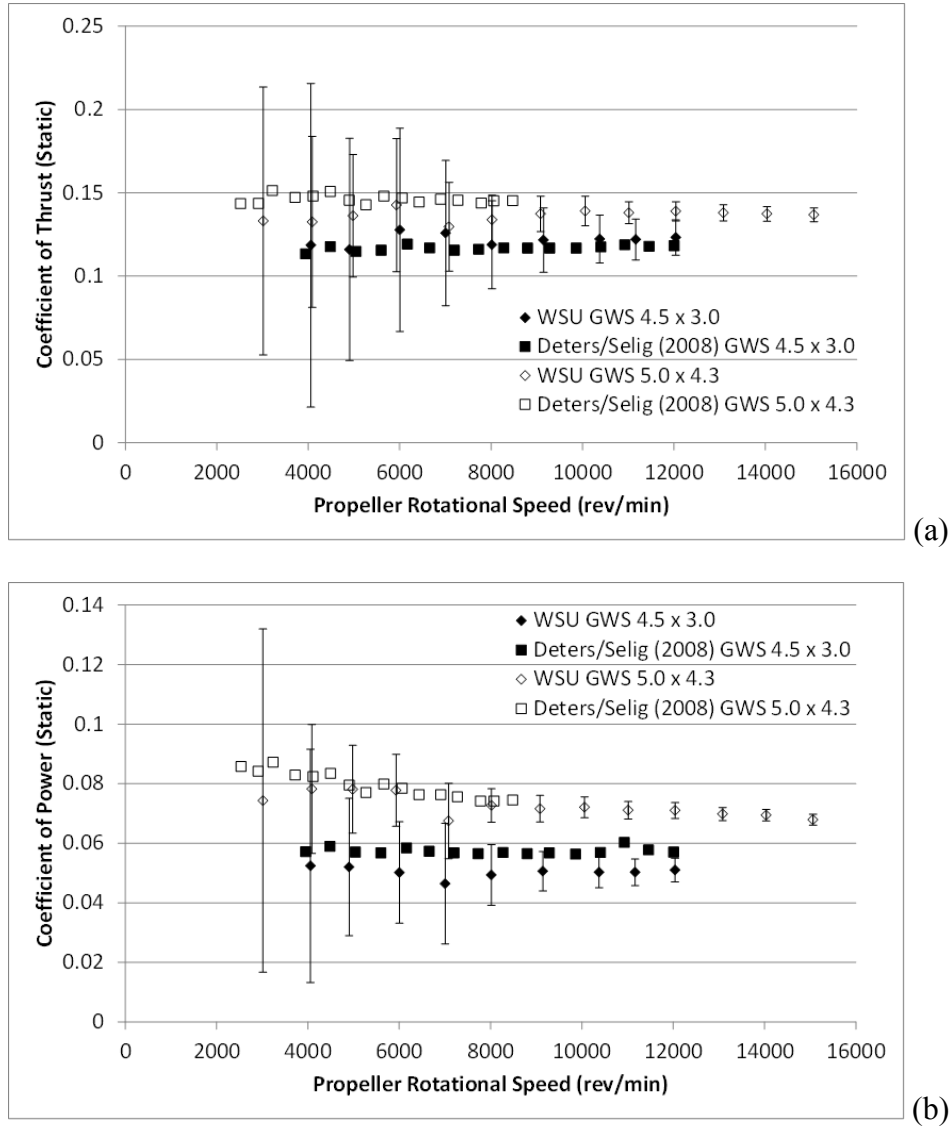


Figure 44 Comparison of the Present Static Results to Deters and Selig (2008) (GWS  $4.5 \times 3.0$  and GWS  $5.0 \times 4.3$  Propellers): (a) Coefficient of Thrust, (b) Coefficient of Propeller Power.

### 5.6.2 Static test results

Having established the validity of the experimental results, static test data was collected for all of the propellers shown in Table 7. Figure 45 shows a comparison between propellers with constant diameter and varying pitch, while Figure 46 gives a comparison between propellers with varying diameter and constant pitch. In Figure 45, the coefficients of thrust and propeller power were relatively constant while the propeller efficiency increased with propeller rotational speed. Increasing the pitch (while holding the propeller diameter constant) significantly increased all

three measures of performance. This same trend can be found in the data provided by Deters and Selig [88] for the coefficient of thrust and coefficient of propeller power for the GWS  $4.0 \times 4.0$  propeller versus that for the GWS  $4.0 \times 2.5$  propeller. In Figure 46, the variation of the three performance parameters with propeller diameter is also shown to be significant, where increasing the diameter decreased the thrust coefficient and the propeller power coefficient but increased the total propulsive efficiency. This trend is also apparent in the data reported by Deters and Selig for the following propellers: GWS  $3.0 \times 3.0$ , GWS  $4.5 \times 3.0$ , and GWS  $5.0 \times 3.0$ .

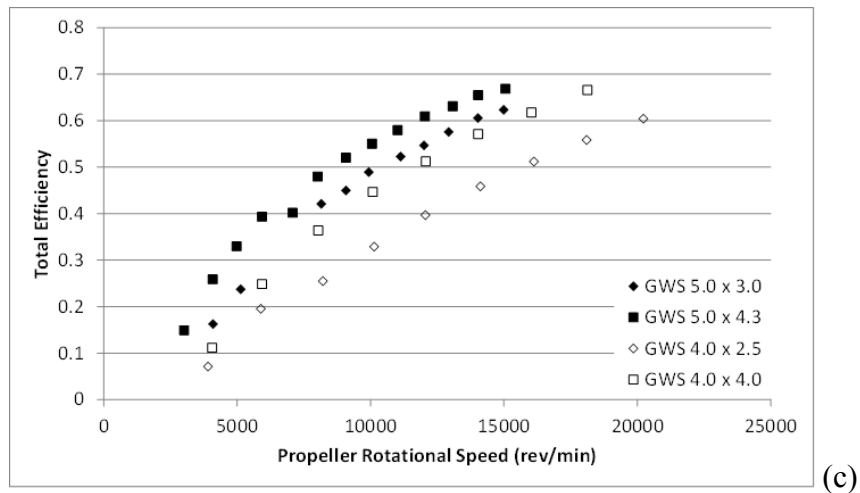
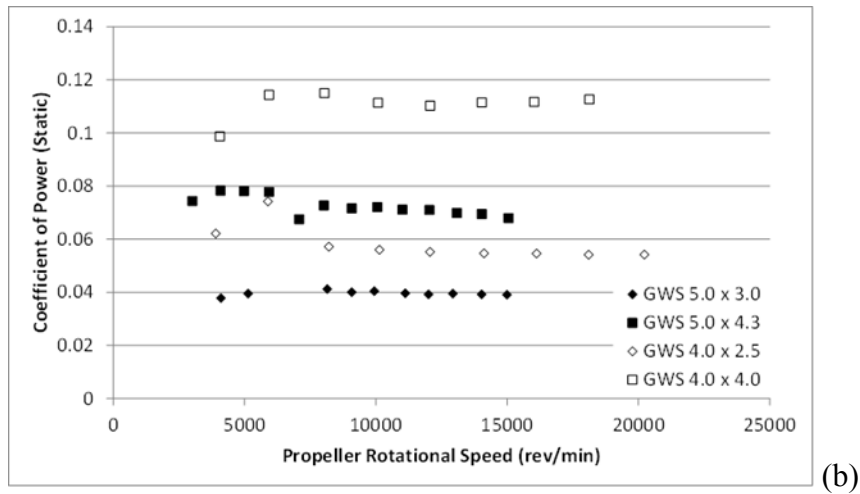
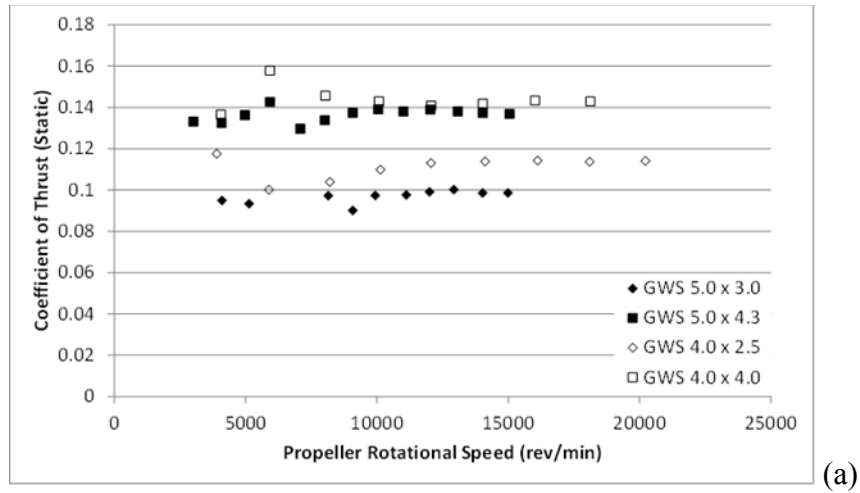


Figure 45 The Effect of Varying Pitch While Holding Diameter Constant (Static Testing)  
 (a) Coefficient of Thrust, (b) Coefficient of Propeller Power, (c) Total Propulsive Efficiency.

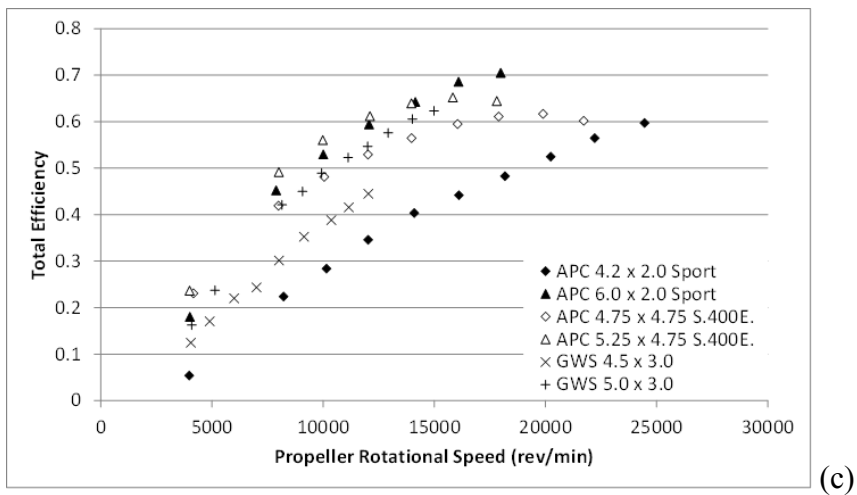
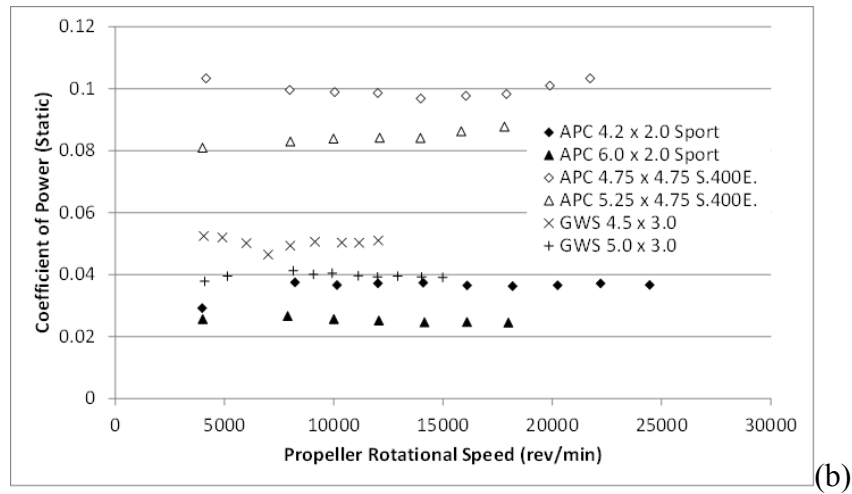
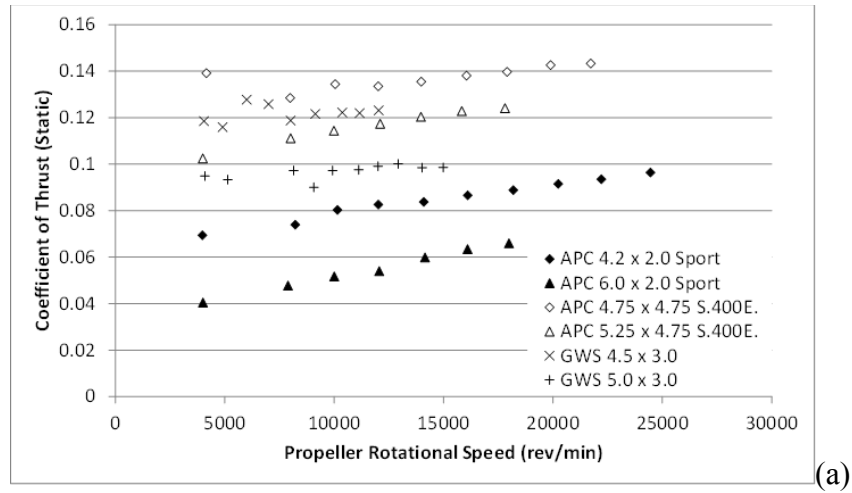


Figure 46 The Effect of Varying Diameter While Holding Pitch Constant (Static Testing)  
 (a) Coefficient of Thrust, (b) Coefficient of Propeller Power, (c) Total Propulsive Efficiency.



### 5.6.3 Validation of the dynamic test

The dynamic test procedure and experiment were validated by comparing the present results to non-archival and archival literature sources. Figure 47 shows typical dynamic results for the thrust and torque generated by one propeller over the full range of airspeed and various levels of rotational speed. Both the thrust and torque increased with rotational speed and decreased with airspeed, as expected. For a given rotational speed, the coefficients of thrust and propeller power decreased with advance ratio, whereas the propeller efficiency increased with advance ratio. The APC  $8.0 \times 3.8$  inch Slow Flyer propeller was tested at nominal propeller rotational speeds of  $n = 4000$  and  $7000$  rpm, and the results for the coefficient of thrust, the coefficient of propeller power, and the propeller efficiency versus advance ratio were compared to those reported on the UIUC propeller database [96], as shown in Figure 48. The agreement with the data from the UIUC database is excellent for both rotational speeds, even where the propeller efficiency drops off steeply with advance ratio.

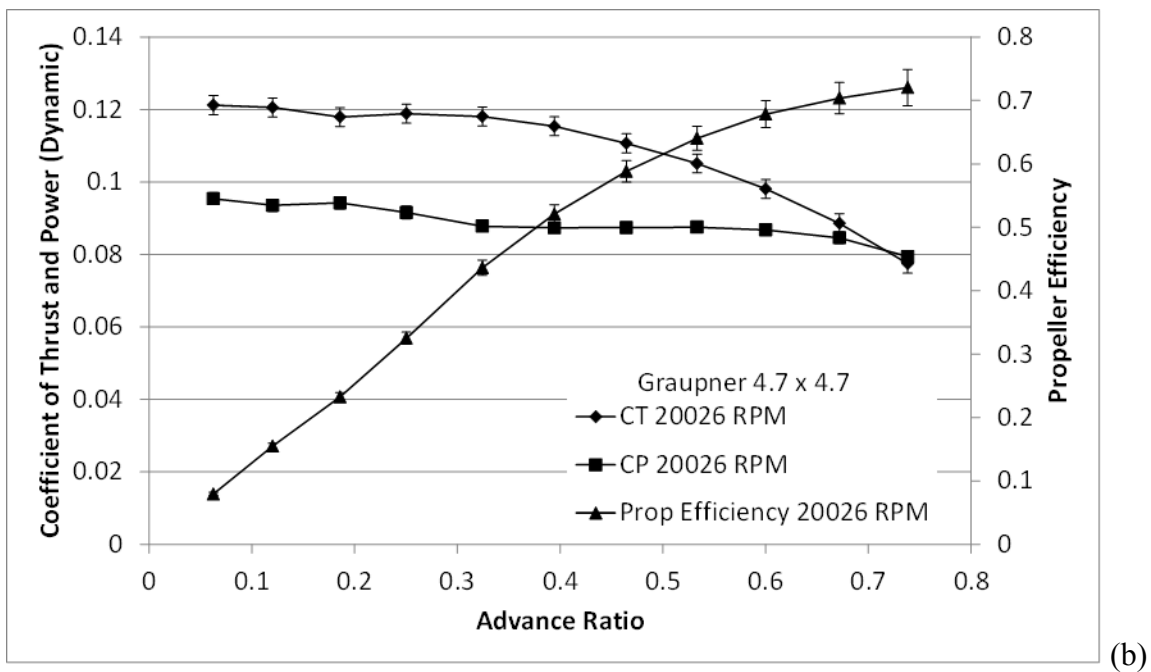
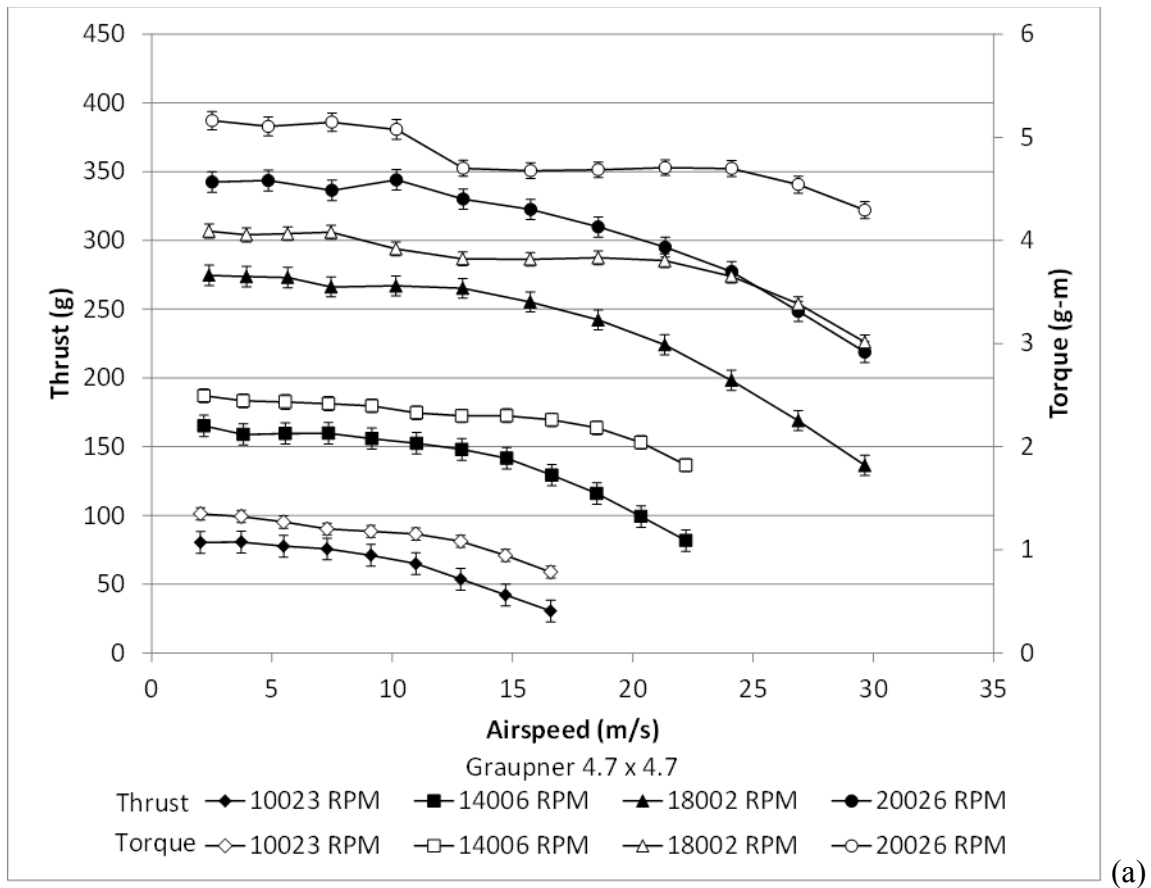


Figure 47 Typical Dynamic Test Results (Graupner 4.7 × 4.7 inch Propeller)  
 (a) Thrust and Torque versus Airspeed for Various Rotational Speeds, (b) Coefficient of Thrust, Coefficient of Propeller Power and Propeller Efficiency versus Advance Ratio.

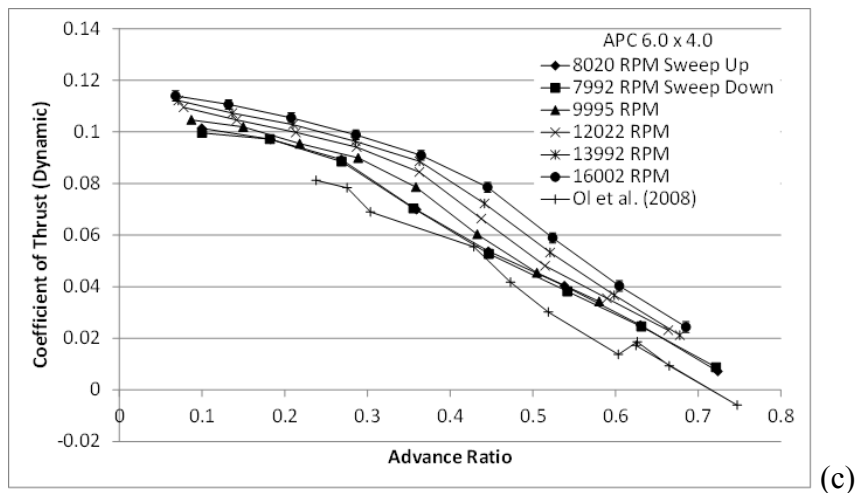
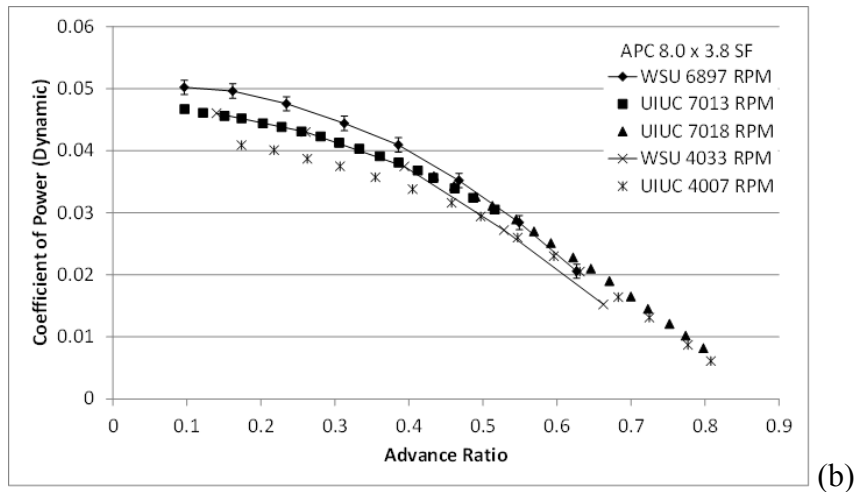
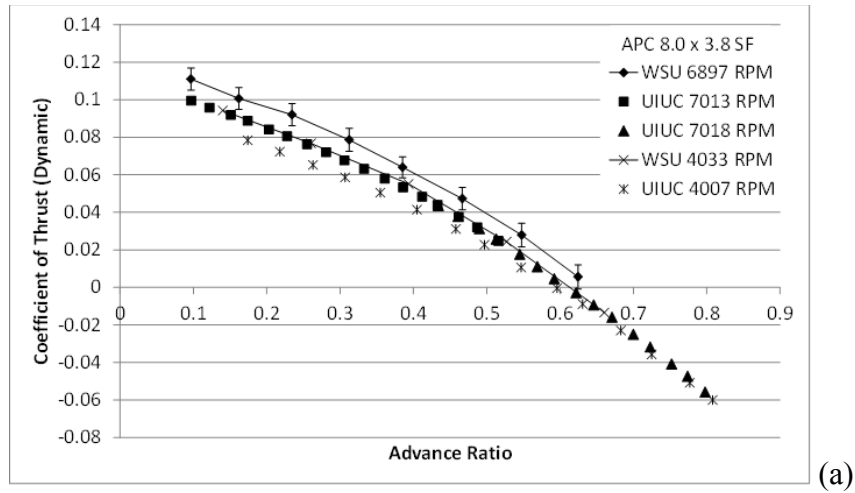


Figure 48 Comparison of Present Dynamic Results to Selig (2012) (APC 8.0 x 3.8 SF)  
(a) Coefficient of Thrust, (b) Coefficient of Propeller Power, (c) Propeller Efficiency.

To further validate the dynamic results, an APC 6.0 x 4.0 inch propeller was tested at nominal propeller rotational speeds of  $n = 8000$  to  $16000$  rpm by intervals of  $2000$  rpm and compared to

the results reported by Ol et al. [95], as shown in Figure 49. The coefficients of thrust and torque decrease with advance ratio and the propeller efficiency increases to a peak and then decreases. Since the exact propeller rotational speed tested by Ol et al. is unclear, it can only be compared to the trends in the data. The present data agrees well with that shown by Ol et al. At a rotational speed of  $n = 8000$  rpm, the propeller was tested by sweeping the advance ratio from low to high values, and then sweeping from high to low values to examine the potential for hysteresis in the experiment. As can be seen, there is not a noticeable difference between these two sets of data.

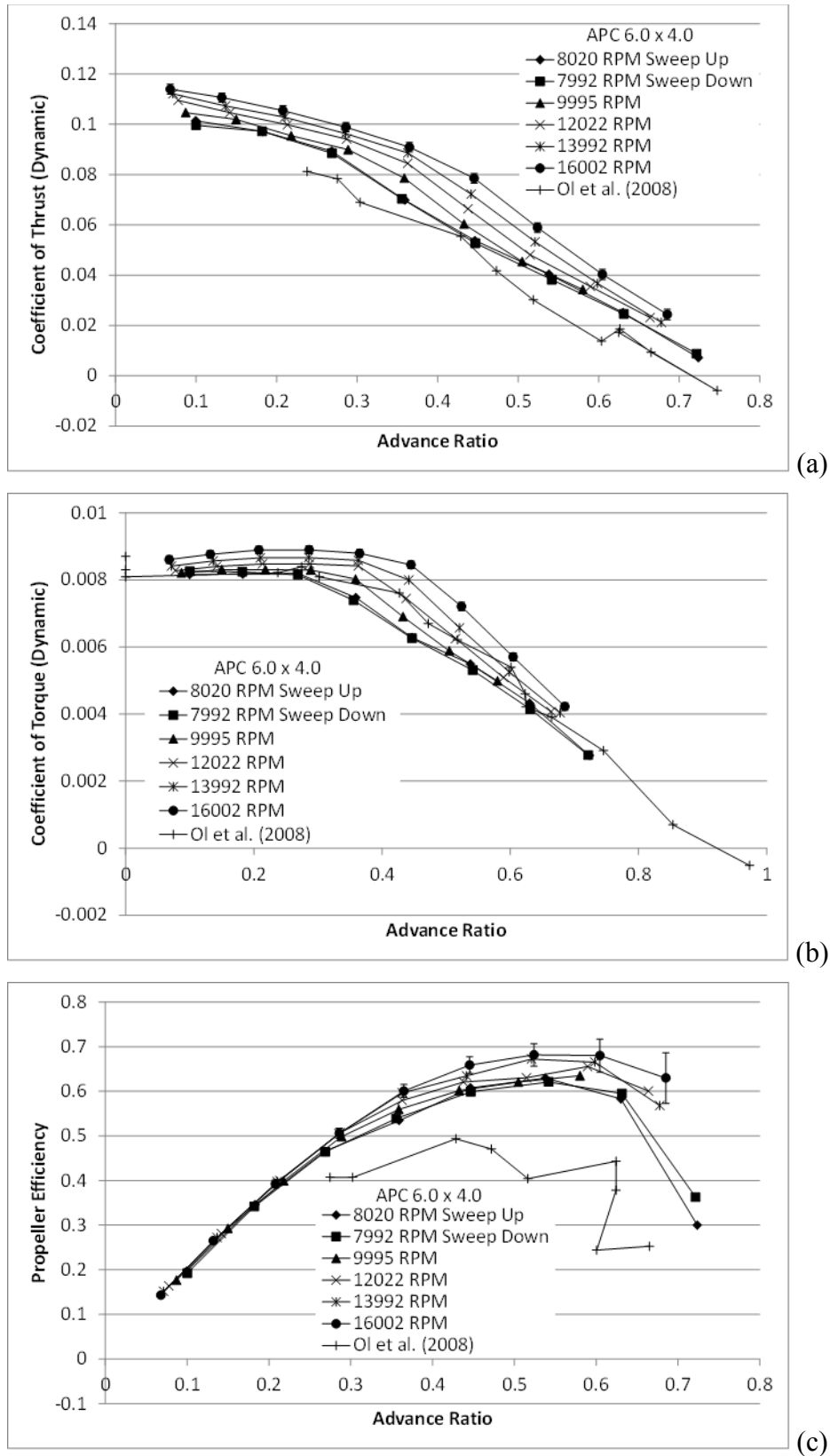


Figure 49 Comparison of Present Dynamic Results to Ol et al. (2008) (APC 6.0  $\times$  4.0)  
(a) Coefficient of Thrust, (b) Coefficient of Torque, (c) Propeller Efficiency.

#### 5.6.4 Dynamic test results

With the dynamic results validated, data was collected for all of the propellers. Comparisons were drawn between propellers with constant diameter and varying pitch in Figure 50 and between propellers with constant pitch and varying diameter in Figure 51, both at a nominal rotational speed of  $n = 16000$  rpm. In Figure 50, propellers with larger pitch generally had larger coefficients of thrust and power, and the windmill state occurred at higher values of the advance ratio, which indicates that larger pitch values tend to allow for higher airspeed. Figure 50(c) shows that the propeller efficiency decreases with increasing pitch for lower values of advance ratio, and the peak efficiency occurs at higher values of advance ratio. An increase in pitch essentially means that the angle of attack of the airfoil is higher, which should increase both thrust and torque prior to reaching stall. In Figure 51, increasing the propeller diameter for a given pitch tends to decrease the coefficient of thrust and the coefficient of power, and the propeller efficiency increases with diameter for lower values of advance ratio. Increasing the diameter for a given rotational speed and airspeed actually increases the thrust and torque due to the increased wingspan of the propeller, but this effect is negated due to the factor of  $D^4$  in the denominator of  $C_T$  and the factor of  $D^5$  in the denominator of the  $C_P$ .

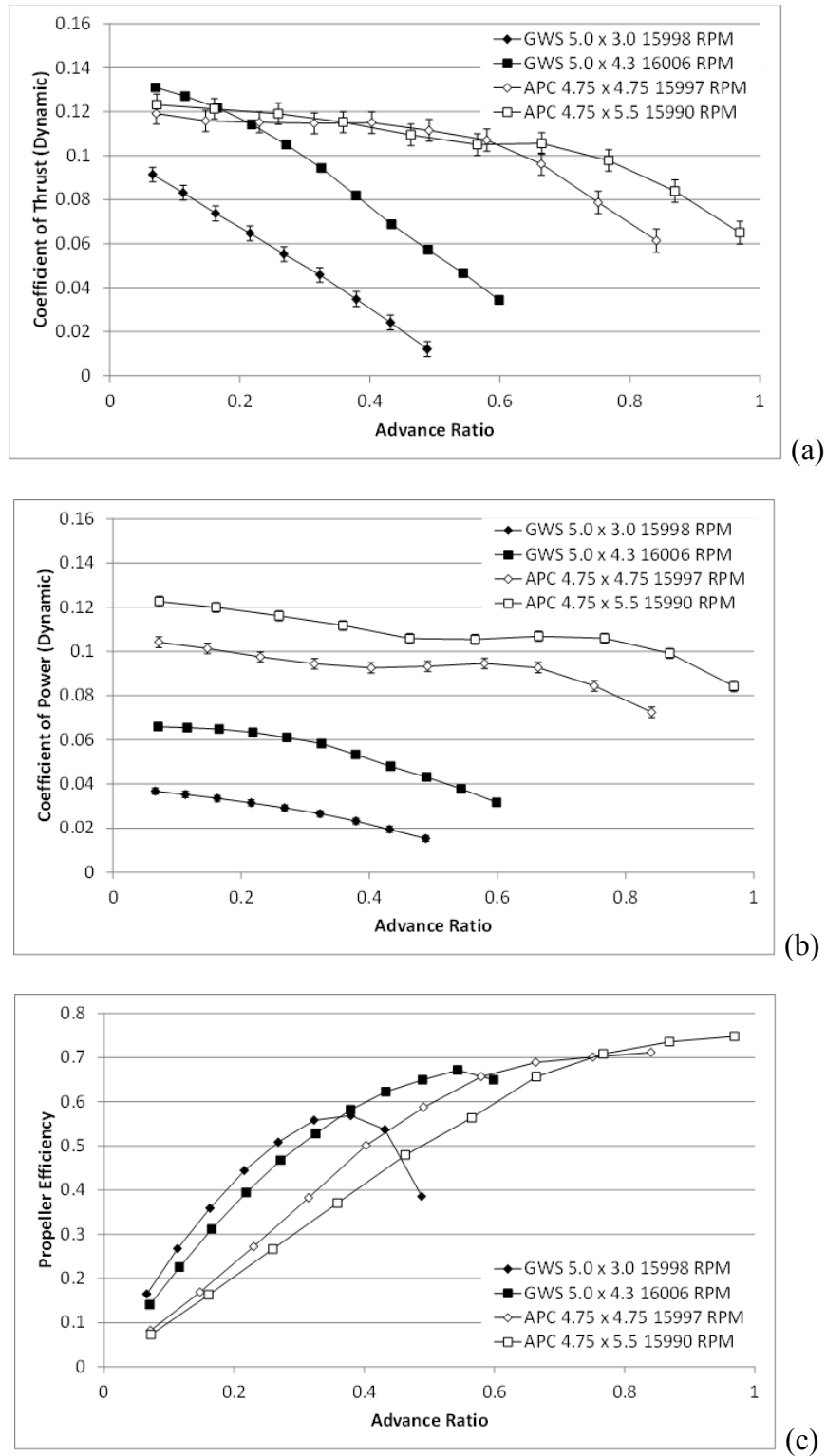


Figure 50 The Effect of Varying Propeller Pitch while holding Diameter Constant (Dynamic Testing)  
 (a) Coefficient of Thrust, (b) Coefficient of Propeller Power, (c) Propeller Efficiency.

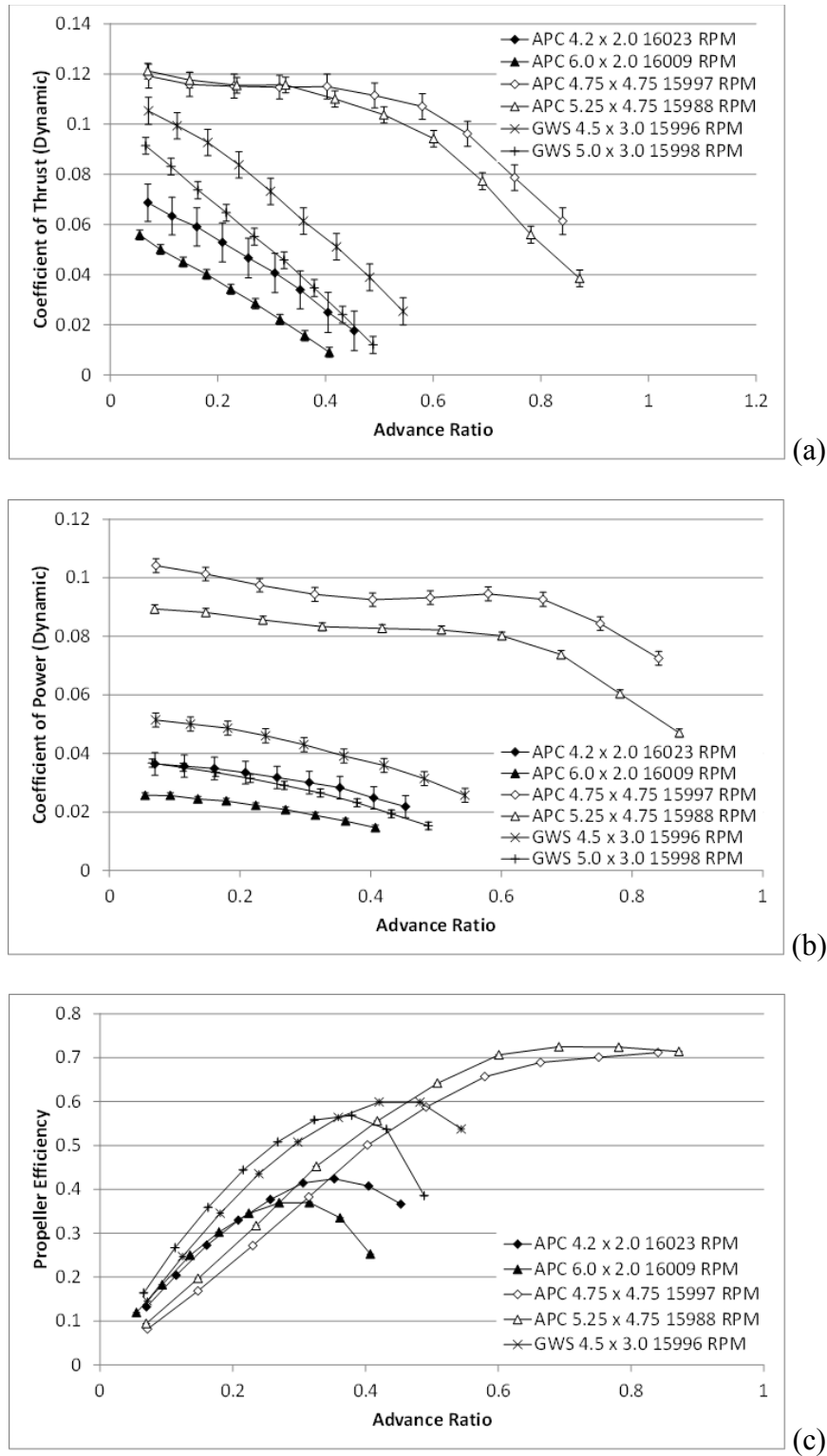


Figure 51 The Effect of Varying Propeller Diameter while holding Pitch Constant (Dynamic Testing)  
 (a) Coefficient of Thrust, (b) Coefficient of Propeller Power, (c) Propeller Efficiency.



Figure 52 presents results for square propellers, where  $D = P$ , from Ol et al. [95], Selig [96], and the present experiment for a fairly wide range in propeller diameter ( $4.0 \leq D \leq 18$  inches). Ol et al. had conjectured that the coefficient of thrust should collapse for square propellers. The results are grouped from small to large propeller diameter, where the three researchers essentially covered different diameter ranges. The data does not appear to collapse in that the propeller diameter still affects the coefficient of thrust. It should be noted, however, that this set of data covers multiple manufacturers and propeller types (i.e., Thin Electric, Sport). Geometric differences in the blades, such as the twist and chord distributions, as well as blade stiffness (and hence deflection under loading) may significantly affect performance.

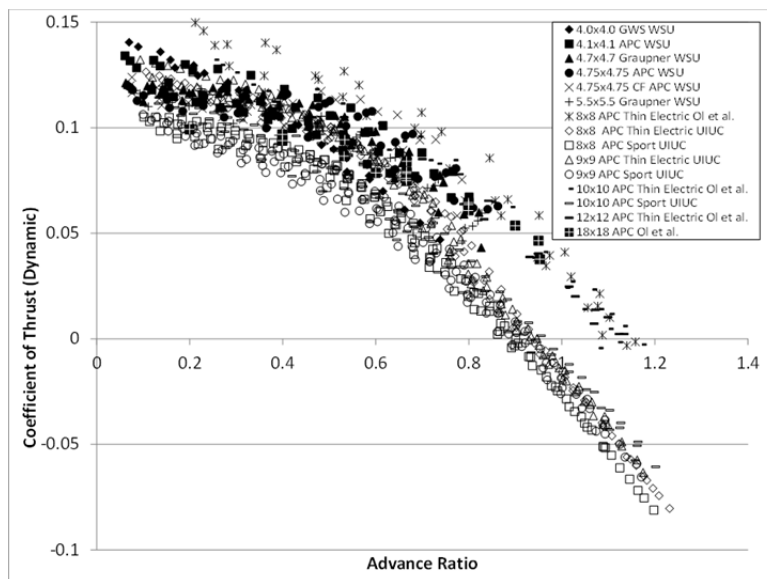


Figure 52 Coefficient of Thrust versus Advance Ratio for Square Propellers ( $D/P = 1.0$ ) with Propeller Diameter Ranging from  $4.0 \leq D \leq 18$  inches.

Figure 52 presents the coefficient of thrust for the same family of propellers (APC Speed 400 Electric). It was assumed that using a group of similar propellers may reduce the effects of geometric blade variations. In this case, the diameter-to-pitch ratio for this family of propellers has a relatively small range ( $0.86 \leq D/P \leq 1.5$ ). Figure 53(a) shows the coefficient of thrust versus advance ratio for all of the collected data for the APC Speed 400 Electric propellers with an uncertainty level of  $\Delta C_T \leq 20\%$ . As can be seen, the results are not correlated well, as witnessed by the low goodness of fit parameter,  $R^2 = 0.529$ . Figure 53(b) shows the coefficient of thrust modified by  $D/P$  plotted against advance ratio, where the goodness of fit parameter is improved to  $R^2 = 0.680$ . This correlation can be further improved by modifying the advance ratio by  $D/P$  as seen in Figure 53(c), where the goodness of fit parameter increases to  $R^2 = 0.720$ , which is a significant improvement over the original data correlation. This analysis shows that the inclusion of the propeller pitch into the correlations for the performance coefficients can be beneficial for this family of propellers.

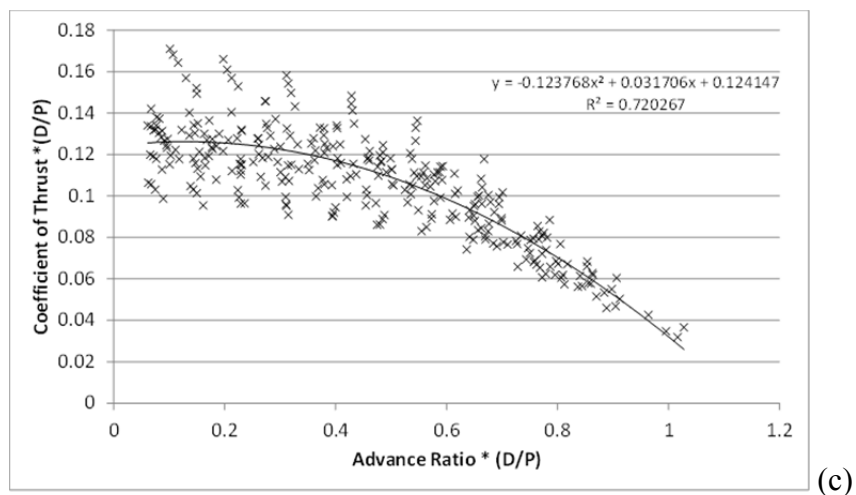
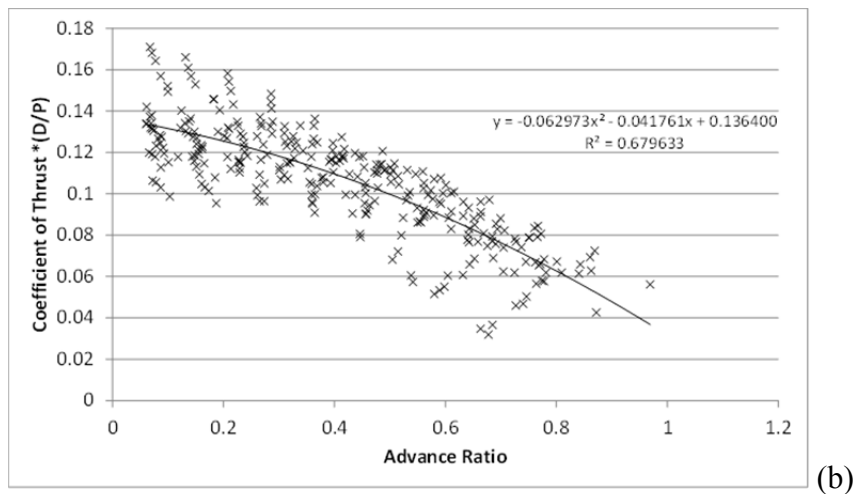
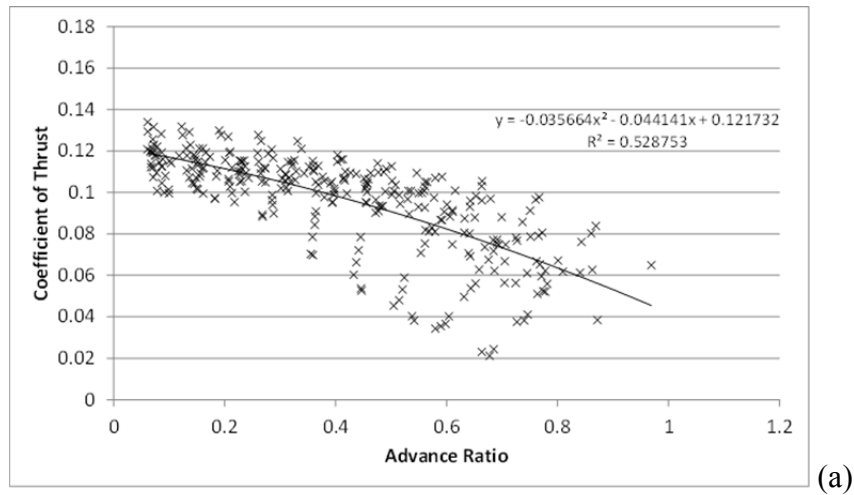
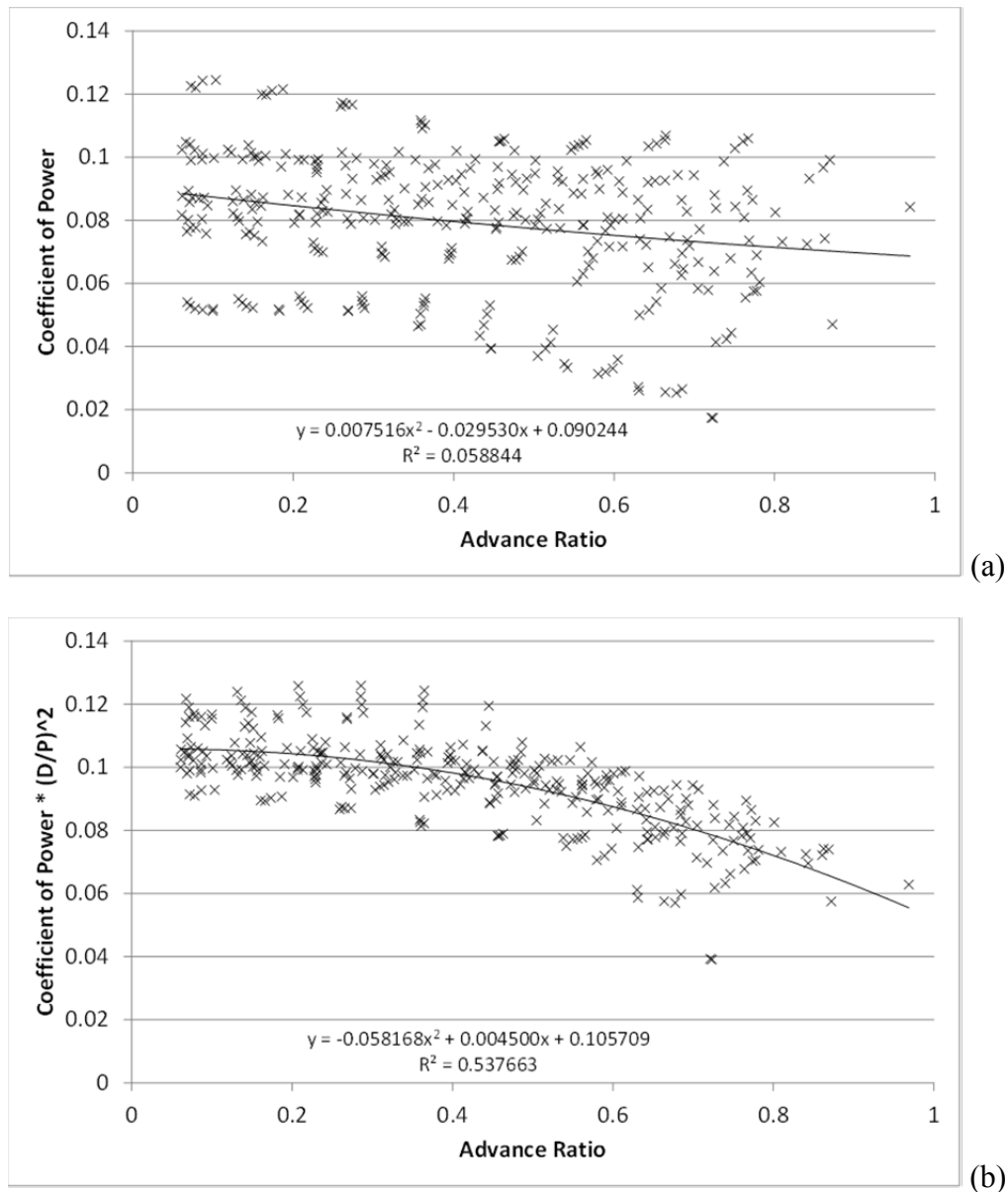


Figure 53 Coefficient of Thrust vs. Advance Ratio for the APC Sport 400 Electric Propellers ( $\Delta C_T \leq 20\%$ )  
 (a) Original Representation of  $C_T$ ; (b)  $C_T$  Modified by  $D/P$ , (c)  $C_T$  and  $J$  Modified by  $D/P$ .

Figure 54(a) shows the coefficient of power versus advance ratio for all of the collected data with an uncertainty level of  $\Delta C_P \leq 20\%$ . As can be seen, the results are not correlated well, as

witnessed by the very low goodness of fit parameter,  $R^2 = 0.059$ . Figure 54(b) shows a coefficient of power that is modified by  $D/P$ , which improves the goodness of fit parameter to  $R^2 = 0.538$ . This is still relatively low, and probably should not be used in most engineering analyses. Figure 55 shows a similar comparison for the propeller efficiency versus the advance ratio. Here, the diameter to pitch ratio was used to modify the original advance ratio to increase the goodness of fit parameter from  $R^2 = 0.938$  to  $0.983$ , which is deemed to be very accurate for most applications, especially for advance ratios less than  $J \leq 0.6$ .



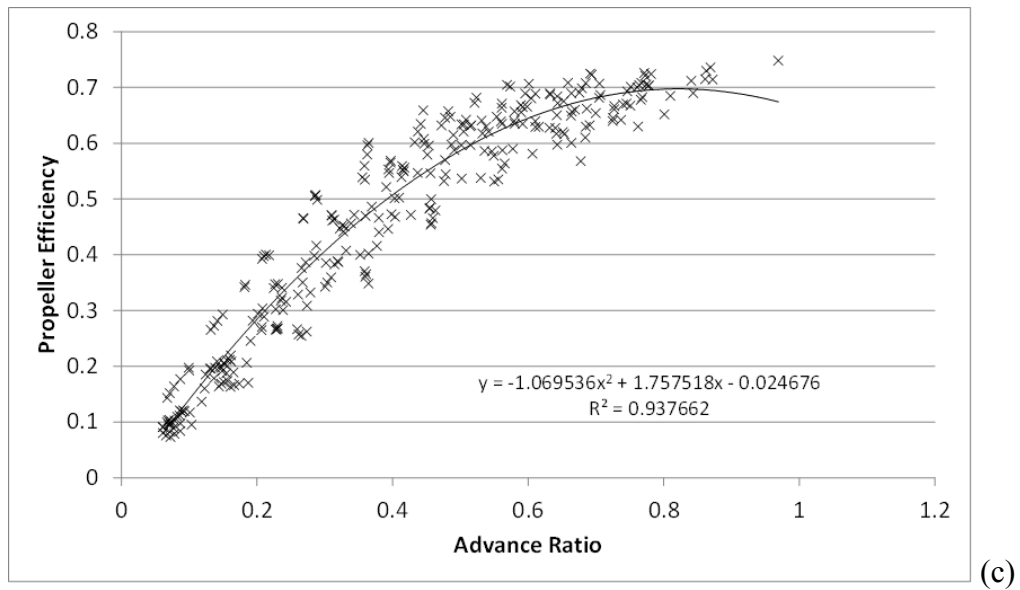


Figure 54 Coefficient of Propeller Power versus Advance Ratio for the APC Sport 400 Electric Propellers ( $\Delta C_p \leq 20\%$ )  
 (a) Original Representation of  $C_p$ ; (b)  $C_p$  Modified by  $D/P$ .

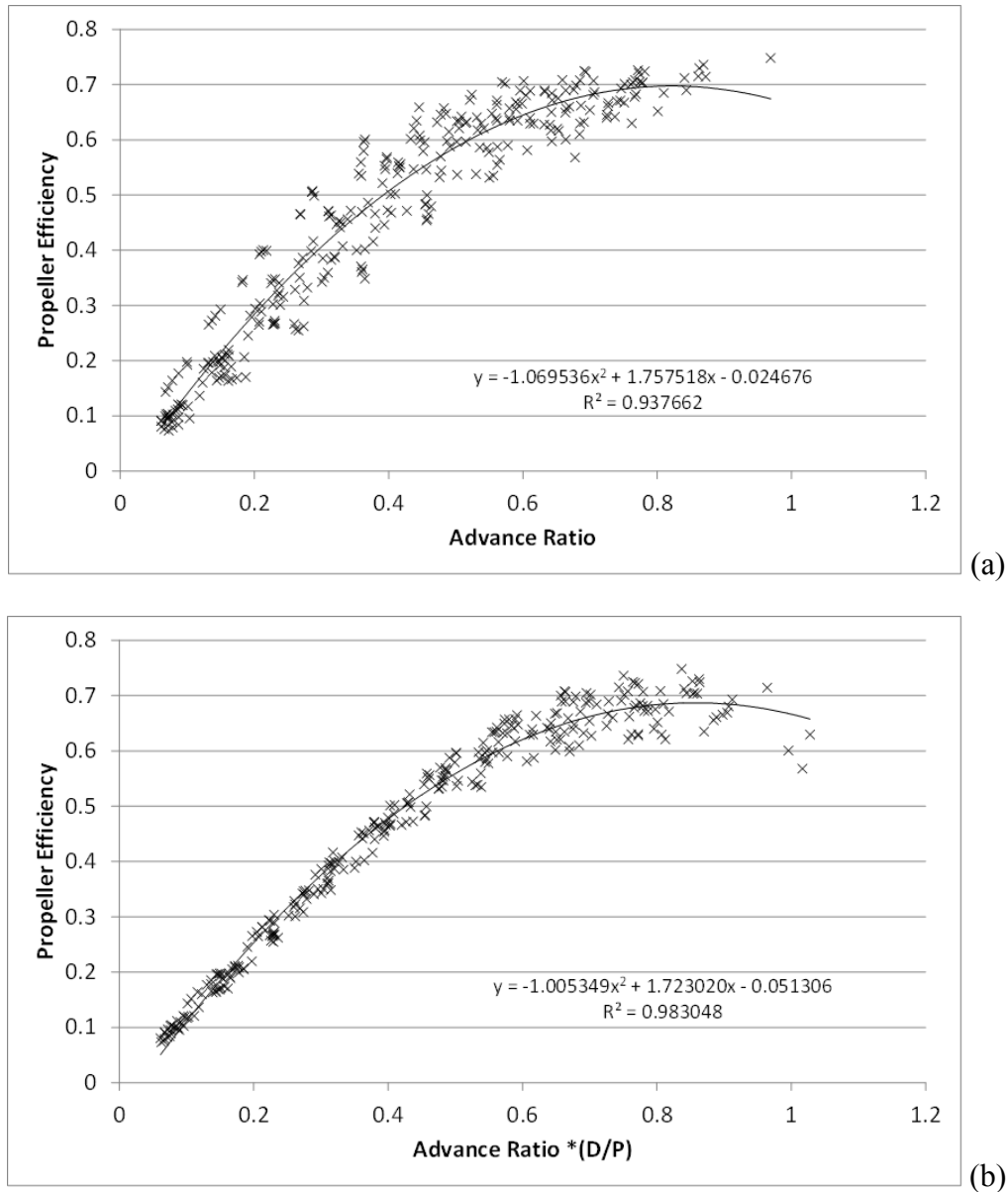


Figure 55 Propeller Efficiency vs. Advance Ratio for the APC Sport 400 Electric Propellers ( $\Delta\eta_p \leq 20\%$ )  
 (a) Original Representation of  $\eta_p$ ; (b) Advance Ratio Modified by  $D/P$ .

## 5.7 Conclusions

Twenty-four propellers in the range of  $4.0 \leq D \leq 6.0$  inches in diameter and  $2.0 \leq P \leq 5.5$  inches in pitch were tested statically and dynamically in the Wright State University wind tunnel over a wide range of propeller rotational speeds and air speeds. A detailed experimental procedure for both cases was employed and an extensive uncertainty analysis was performed on the resulting data. The experiments were validated by comparing the results to previous works. The repeatability of the experimental results and the repeatability of the manufacture of the propellers were proven by testing three duplicate propellers three times each. Static tests were performed by varying propeller speed from  $n = 4000$  rpm to the maximum speed limited by the manufacturer's

specifications or the maximum motor temperature. Dynamic tests were performed by holding the propeller speed constant and varying the wind tunnel airspeed and thus varying the advance ratio.

For a given airspeed and rotational speed, the thrust and torque both increased with propeller pitch and diameter, as expected. For static testing, the coefficient of thrust, coefficient of propeller power and the total propulsive efficiency increased with propeller pitch for a given propeller diameter at all rotational speeds. Alternately, when the diameter was increased and the pitch was held constant, the coefficient of thrust and coefficient of propeller power increased and the total propulsive efficiency decreased. Similar results were found for dynamic testing. The square ( $D/P$ ) propellers that were tested and compared to the results in the open literature were not correlated well with propeller diameter alone, which was possibly due to variations in the twist and chord distributions, as well as the blade stiffness. Correlations for the coefficient of thrust, propeller power and propeller efficiency for a family of propellers (APC Speed 400 Electric) under dynamic testing were found to be improved when the original coefficient (and/or advance ratio) was modified by  $D/P$ . This permitted the pitch to be accounted for in the performance characteristics of propellers in the range of  $0.86 \leq D/P \leq 1.5$ .

## 6 References

1. Corke, T.C., Enloe, C.L., and Wilkinson, S.P., *Annual Rev. Fluid Mech.*, Vol. 42, 2010, pp. 505-525.
2. Corke, T.C., Post, M.L., Orlov, D.M., Vol. 43, 2007, pp. 193-217.
3. Moreau, E., *J. physics D: Applied Physics*, Vol. 40, 2007, pp. 605-636.
4. Shang, J.S., Kimmel, R., Menart, J., and Surzhikov, S.T., *J. of Propulsion and Power*, Vol. 24, No. 5, 2008, pp. 923-934.
5. Shang, J.S., Surzhikov, S.T., Kimmel, R., Gaitonde, D., Menart, J., and Hayes, J., *Progress in Aerospace Sciences*, Vol. 41, 2005, pp. 642-668.
6. Mitchner M, Kruger C.H. Partially Ionized Gas, New York: Wiley & Sons; 1973.
7. Raizer, Yu. P., *Springer-Verlag*, Berlin, 1991.
8. Howatson, A.M., *Introduction to Gas Discharges*, 2<sup>nd</sup> edition, Pergamon Press, Oxford United Kingdom, 1975. pp. 1-49.
9. Elisson, B. and Kogelschatz, U. *Plasma Science*, Vol. 19, 1991, pp. 1063-1077.
10. Enloe, C.L., McLaughlin T.J., Vandyken, R.D., Kachner, K.D., Jumper, E.J., Corke, T.C., Post, M., and Haddad, O., *AIAA J.* Vol. 42, 2004, pp. 595-604.
11. Enloe, C.L., Mcharg, M.G., McLaughlin, T.E., *J. App. Phys.* Vol. 103, 2008, 073302.
12. Macheret, S.O., Shneider, M.N., and Miles R.B., *AIAA J.* Vol. 40, 2001, pp. 74-81.
13. Bogdanov, E.A., Kudryavtsev, A.A., Kuranov, A.L., Kozlov, L.E, and Tkchenko, T.L., *AIAA* 2008-1377, 2008.
14. Kim, W., Do, H., Mungal, M.G., and Cappelli, M.A., *Applied physics Letter*. Vol. 91, 2007, 181501.
15. Golubovskii, Yu.B., Maiorov, V.A., Behnke, J., and Behnke, J.F., *J. Physics D: applied Physics*, Vol. 35, 2002, pp.751-761.
16. Pancheshnyi, S.V., Starikovkaia, S.M., and Starikovskii, A. Yu., *J. Phys. D: Phys*, Vol. 34, 2001, pp. 105-115.
17. Opaits, D.F., Sheider, M.N., Miles, R.B., Likhanskii, A.V., and Macheret, S.O., *Physic of Plasma*, Vol. 15, 2008, pp, 073505-1-5.
18. Shang, J.S., *Journal of Scientific Computing*, Vol. 25, No.1, Oct. 2005, pp. 289-306.
19. Shang, J.S., *Progress in Aerospace Sciences*, Vol. 38, No. 6-7, 2002, pp. 449-467.
20. Shang, J.S., Surzhikov, S.T., and Yan, H., *Frontiers in Aerospace Engineering*, Vol. 1, No.1, Nov. 2012, pp.1-12.
21. Shang, J.S. and Surzhikov, S.T., *J. Progress in Aerospace Sciences*, Vol. 53, 2012, pp. 46-65.
22. Ziemer, R.W., *Journal of American Rocket Soc.*, Vol. 29, 1959, pp. 642-647.
23. Cristofolini, A., Borghi, C.A., Carraro, M.R., Neretti, G., Passaro, A., Fantoni, G., and Biagioni, L., *IEEE Trans. Plasma Science*, Vol. 36, No. 2, 2008, pp. 530-541.
24. Matsuda, A., Otsu, H., Kawamura, M., Konigorski, D., Takizawa, Y., and Abe, T. *Phys. Of Fluids*, Vol. 20, 127103, 2008, pp.127103,1-10.
25. Gulhan, A., Esser, B., Koch, U., Siebe, F., Riehmer, J., Giordano, D., and Konigorski, D., *J. Spacecraft & Rockets*, Vol. 46, No. 2, 2009, pp. 274-283.
26. Bird, R., Stewart, W., and Lightfoot, E., *Transport Phenomena*, 2<sup>nd</sup> Edition, John Wiley & Sons, New York, 2002. pp.513-538.
27. Capitelli M., Gorse C., Longo S., Giordano D., *J. of Thermophysics and Heat Transfer*. 2000. Vol. 14, No. 2, pp. 259-268.
28. Raizer, Yu. P. and Surzhikov, S.T., *High Temperature*, Vo. 26, (3), 1987, pp. 479-485.

29. Raizer, Yu. P. and Surzhikov, S.T., *High Temperature*, Vol. 28 (3), 1990, pp. 324-328.
30. Surzhikov, S.T. Shang, J.S., *AIAA* 2003-0176.
31. Surzhikov, S.T. Shang, J.S., *AIAA* 2004-2659, 2004.
32. Surzhikov, S.T., and Shang, J.S., *J. Computational Physics*, Vol. 199, 2, Sept. 2004, pp. 437-464.
33. Kimmel, R.L., Hayes, J.L., Menart, J. A., and Shang, J., *J. Spacecraft & Rockets*, Vol. 42, No. 6, 2006, pp.1340-1346.
34. Leonov, S., Bityurin, V., Savelkin, K., and Yarantsev, D., *AIAA* 2002-0355, 2002.
35. Massines, F., Rabehi, A. Decomps, P., Gadri, R.B., Segur, P., and Mayoux, C., *J. Applied Phys*, Vol. 83, No. 6, 1998, pp. 2950-2957.
36. Lee, D., Park, J.M., and Hong, S.H., *IEEE Trans Plasma Science*, Vol. 33 No. 2, 2005, pp. 949-957.
37. Gibalov, V.I. and Pietsch, G.J., *J. Physics D: Appl. Physics*, Vol. 37, 2004, pp. 2082-2092.
38. Boeuf, J.P., Pitchford, L.C., *J. Appl. Physics*, Vol. 97, 2005, pp.103307-1-10.
39. Boeuf, J.P., Lagmich, Y., Unfer, T., Callegari, Th., and Pitchford, L.C., *J. Physics D: Applied Physics*, Vol. 40, 2007, pp. 652-663.
40. Unfer, T. and Boeuf, J.P., *J. Phys. D: Appl. Phys.* Vol. 42, 2009, pp. 194017-1-12.
41. Solov'ev, V., Konchakov, A.M., Krivtsov, V.M., Aleksandrov, N.L., *Low-Temperature Plasma*, Vol. 34, No. 7, 2008, pp. 594-608.
42. Likhanskii, A.V., Shneider, M.N., Macheret, S.O., Miles, R.B., *J. appl. Physics*, Vol. 103, 2008, pp. 055505-1-13.
43. Shang, J.S., Huang, P.G., Yan, H., Surzhikov, S.T., *J. Applied Physics*, Vol. 105, 2009, pp. 023303-1-14.
44. Shang, J.S. and Huang, P.G., *J. Applied Physics*, Vol. 107, No.11. pp 113302-1-7. 2010.
45. Shang, J.S., Roveda, F., and Huang, P.G., *J. Applied Physics*, Vol. 109, No.11. pp. 113301-1-8, 2011.
46. Huang, P.G., Shang, J.S., and Stanfield, S.A., *AIAA J.* Vol. 49, No.1. Jan. 2011, pp. 119-127.
47. Singh, K.P. and Roy, S., *J. Appl. Phys*, Vol. 101, 2007, pp. 123308 1-8.
48. Graves, D.B. and Jensen, K.E. *IEEE Transactions on Plasma Science*, Vol, PS-14, No.2, 1986, pp.78-91.
49. Boeuf, J.P. and Marode, E. *J. Phys. D.. Appl. Phys.*, Vol. 12, 1982, pp. 2169-2187.
50. Kraus, J.D., *Electromagnetics*, McGraw-Hill, New York, NY, 1953.
51. Yee, H.C, *Comput. Math. Appl*, Vol. 12A, 1986, pp. 413-432.
52. Stone, H.L., *SIAM J. Num. Analy.* Vol. 5 No.3, 1968, pp. 530-558.
53. Schneider, G. E. and Zedan, M., *Numerical Heat Trabsfer*, Vo. 4, 1981, pp. 1-19.
54. Brandt, A., *Math. Comput.* Vol. 31, 1977, pp. 333-390.
55. Von Engel, A. and Steenbeck, M., *Springer*, Berlin, Vol. II, 1932.
56. Rafatov, I., Bogdanov, E.A., and Kudryavtsev, A.A., *Physics Plasma*, Vol. 19, 2012, pp. 033502 1-12.
57. Petrushev, A.S., Surzhikov, S.T., and Shang, J.S., *High Temperature*, Vol. 44, No. 6, 2006, pp. 814-822.
58. Gherardi, N., Gouda, G., Gat, E., Richard, A., and Massines, F., *Plasma Sources Science Technology*, Vol. 9, 2000, pp. 340-346.
59. Stanfield, S.A., Menart, J., DeJoseph, C., Kimmel, R.L., Hayes, J.R., *J AIAA*, Vol. 47, 2009, pp. 1107-1115.
60. Jayaraman, B. and Shyy, W., *Progress in Aerospace Sciences*, Vol. 44, 2008, pp. 131-191.



61. Hoskinson, A.R., Hershkowitz, N., and Ashpis, D.E., *J. Phys. D: Applied Physics*, Vol. 41, 2008, pp. 245209-1-9.
62. Hoskinson, A.R. and Hershkowitz, N., *J. Phys. D: Applied Physics*, Vol. 44, 2011, pp. 085202-1-11.
63. H. Zhu, R.J. Kee, V.M. Janardhanan, O. Deutschmann, D.G. Goodwin, *J. Electrochem. Soc.* 152 (2005) A2427.
64. E.S. Greene, W.K.S. Chiu, M.G. Medeiros, *J. Power Sources* 161 (2006) 225.
65. M. Ni, M.K.H. Leung, D.Y.C. Leung, *J. Power Sources* 168 (2007) 369.
66. S.H. Chan, Z.T. Xia, *J. Electrochem. Soc.* 148 (2001) A388.
67. S. Chan, K. Khor, Z. Xia, *J. Power Sources* 93 (2001) 130.
68. D. Bouvard, F.F. Lange, *Acta Met. Mater.* 39 (1991) 3083.
69. P. Costamagna, P. Costa, V. Antonucci, *Electrochim. Acta* 43 (1998) 375.
70. J.A. Currie, *J. Appl. Phys.* 318 (1960).
71. R. Dias, J. Teixeira, M. Mota, a Yelshin, *Sep. Purif. Technol.* 51 (2006) 180.
72. M. Matyka, A. Khalili, Z. Koza, *Phys. Rev. E* 78 (2008) 026306.
73. Randall M. German, *Particle Packing Characteristics*, Metal Powder Industry, 1989.
74. R.P. Dias, J. a. Teixeira, M.G. Mota, A.I. Yelshin, *Ind. Eng. Chem. Res.* 43 (2004) 7912.
75. R. O'Hayre, S.-W. Cha, W. Colella, F.B. Prinz, *Fuel Cell Fundamentals* (2nd Ed.), John Wiley & Sons, Inc., Hoboken, New Jersey, 2009.
76. W.Y. Lee, D. Wee, A.F. Ghoniem, *J. Power Sources* 186 (2009) 417.
77. W. G. Pollard, *Phys. Rev.* 73 (1948) 762.
78. J.H. Nam, D.H. Jeon, *Electrochim. Acta* 51 (2006) 3446.
79. C. Berger, *Handbook of Fuel Cell Technology*, Prentice Hall Inc, 1968.
80. S. Yeramunis, S.W. Cornell, B. Wintner, *Nature* (1965) 835.
81. S.P. Jiang, W. Wang, Y.D. Zhen, *J. Power Sources* 147 (2005) 1.
82. S. Kim, H. Moon, S. Hyun, J. Moon, J. Kim, H. Lee, *Solid State Ionics* 177 (2006) 931.
83. S.P. Jiang, P.J. Callus, *Solid State Ionics* 132 (2000) 1.
84. Sukeshini, A.M., Gardner, P., Jenkins, T., Reitz, T.L., and Miller, R.M., *Engineering and Technology*, vol. 1, pp. 325-332 (2010).
85. Brandt, J.B. and Selig, M.S. *49th AIAA Aerospace Sciences Meeting*. 2011. AIAA 2011-1255.
86. R. Dias, J. Teixeira, M. Mota, a Yelshin, *Sep. Purif. Technol.* 51 (2006) 180.
87. M. Matyka, A. Khalili, Z. Koza, *Phys. Rev. E* 78 (2008) 026306.
88. Randall M. German, *Particle Packing Characteristics*, Metal Powder Industry, 1989.
89. R.P. Dias, J. a. Teixeira, M.G. Mota, A.I. Yelshin, *Ind. Eng. Chem. Res.* 43 (2004) 7912.
90. R. O'Hayre, S.-W. Cha, W. Colella, F.B. Prinz, *Fuel Cell Fundamentals* (2nd Ed.), John Wiley & Sons, Inc., Hoboken, New Jersey, 2009.
91. W.Y. Lee, D. Wee, A.F. Ghoniem, *J. Power Sources* 186 (2009) 417.
92. W. G. Pollard, *Phys. Rev.* 73 (1948) 762.
93. J.H. Nam, D.H. Jeon, *Electrochim. Acta* 51 (2006) 3446.
94. C. Berger, *Handbook of Fuel Cell Technology*, Prentice Hall Inc, 1968.
95. S. Yeramunis, S.W. Cornell, B. Wintner, *Nature* (1965) 835.
96. S.P. Jiang, W. Wang, Y.D. Zhen, *J. Power Sources* 147 (2005) 1.
97. S. Kim, H. Moon, S. Hyun, J. Moon, J. Kim, H. Lee, *Solid State Ionics* 177 (2006) 931.
98. S.P. Jiang, P.J. Callus, *Solid State Ionics* 132 (2000) 1.

99. Brezina, Aron J. "Measurement of Static and Dynamic Performance Characteristics of Electric Propulsion Systems." *Masters Thesis*. Wright State University, 2012.
100. Corrigan, E.K. and Altman, A. *46th AIAA Aerospace Sciences Meeting*. 2008. AIAA 2008-179.
101. Deters, R.W. and Selig, M.S. *26th AIAA Applied Aerodynamics Conference*. 2008. AIAA 2008-6246.
102. Gamble, D.E. "Automated Dynamic Propeller Testing at Low Reynolds Numbers." *M.S. Thesis*. Stillwater, OK: Oklahoma State University, 2009.
103. Glauert, H.. *The Elements of Aerofoil and Airscrew Theory*. Cambridge: Cambridge University Press, 1926.
104. Hackett, J.E., Lilley, D.E., and Wilsden, D.J. *Estimation of Tunnel Blockage from Wall Pressure Signatures: A Review and Data Correlation*. NASA CR15-2241, 1979.
105. Hepperle, M. *PropellerScanner Software*. 2003. <http://www.mh-aerotools.de/>.
106. Kline, S. J., and F. A. McClintock. "Describing Uncertainties in Single-Sample Experiments." *Mech. Eng.*, 1953: 3.
107. Merchant, M.P. and Miller, L.S. "Propeller Performance Measurement for Low Reynolds Number UAV Applications." *44th AIAA Aerospace Sciences Meeting*. 2006. AIAA 2006-1127.
108. Ol, M., Zeune, C., and Logan, M. "Analytical – Experimental Comparison for Small Electric Unmanned Air Vehicle Propellers." *26th AIAA Applied Aerodynamics Conference*. 2008. AIAA 2008-7345.
109. Selig, M. *UIUC Propeller Database*. 2012. <http://www.ae.illinois.edu/m-selig/props/propDB.html>.
110. Selig, M., and Ananda, G. *Low Reynolds Number Propeller Performance Data: Wind Tunnel Corrections for Motor Fixture Drag*. 2011. <http://www.ae.illinois.edu/m-selig/props/uiuc-props-wind-tunnel-correction.pdf>.